UNIVERSITÀ DEGLI STUDI DI NAPOLI FEDERICO II

DIPARTIMENTO DI INGEGNERIA CHIMICA, DEI MATERIALI E DELLA PRODUZIONE INDUSTRIALE

DOTTORATO IN INGEGNERIA DEI PROCESSI E DEI PRODOTTI INDUSTRIALI - XXXV CICLO

Ph.D. THESIS

Directly Irradiated Fluidized Bed Autothermal Reactor for solar thermochemical processes and energy storage

Scientific Committee

Prof. Piero Salatino

Prof. Roberto Solimene

Dr. Claudio Tregambi

Dr. Maurizio Troiano

PhD Candidate

Stefano Padula

Academic year 2021/2022

“…nella ricerca scientifica, né il grado di intelligenza né la capacità di eseguire e portare a termine con esattezza il compito intrapreso, sono i fattori essenziali per la riuscita e la soddisfazione personale. Nell'una e nell'altra contano maggiormente la totale dedizione e il chiudere gli occhi davanti alle difficoltà…”

Rita Levi-Monalcini

CHAPTER I

CONCENTRATING SOLAR THERMAL TECHNOLOGIES

CHAPTER II

MODEL OF DIFBAR AS THERMOCHEMICAL BATTERY

CHAPTER III

MULTIPHASE REACTORS FOR THERMOCHEMICAL PROCESSES

CHAPTER IV

DIFBAR PROOF OF CONCEPT

Abstract

This Ph.D. thesis deals with the development of a new solar reactor, named Directly Irradiated Fluidized Bed Autothermal Reactor (DIFBAR), that exploits fluidization technology and the principle of an autothermal reactor. The recovery of the sensible energy of the solid products to preheat the reactants is realized with an innovative design coupling a cavity receiver with a countercurrent double-pipe heat exchanger. This allows to carry out chemical processes at high temperature with a large saving of solar energy. In the base scheme, the solar receiver works also as a gas-solid separator/reactor and the bed material is continuously recycled to a reservoir, that can also be operated as a fluidized bed reactor for the regeneration of the solid reactant. Alternative plant schemes and reactor configurations have also been envisaged: a “Dual Tank” scheme in which the solid product is collected in a separate reservoir and can be handled to other plant units and a “Shaded reactor” configuration in which the reaction occurs in a vessel separated from the receiver. The objective of this work is the proof-of-concept of this technology, and it has been pursued through modeling and experimental activities, culminating with the design, construction and characterization a fully operational prototype.

A simple compartmental model has been implemented to understand the effect of the design and operational variables and a numerical study has been conducted to assess the application of the DIFBAR for ThermoChemical Energy Storage (TCES), taking the Calcium Looping (CaL) as a reference process. The results served as a basis for the design of the prototype.

Experiments of Chemical Looping Reforming of methane (CH_4), testing a laboratory-prepared perovskite with chemical formula $La_{0.6}Sr_{0.4}FeO_3$, have been carried out with bench reactors, as preliminary steps toward an application with the DIFBAR prototype. In particular, reaction temperatures,

oxygen capacity and selectivity have been assessed by the analysis of time-resolved concentration profiles of the outlet gas. The material stability has been tested by iterated cycles. The effect of gas-solid contact patterns has been scrutinized by comparing the performance of fixed and fluidized bed reactors in terms of conversion rates and selectivity. The results encouraged to test the material with a directly irradiated reactor unit, reproducing the geometry of the DIFBAR receiver. A batch of perovskite was mixed with the reactor inventory, made of mullite particles. The conversion rates did not match those under fluidized bed conditions, maybe as a result of a physical-chemical interaction between the perovskite oxygen carrier and the mullite.

Finally, the DIFBAR prototype has been built and tested. A base design has been adopted and characterized, featuring a closed circulation loop of the solid composed by a fluidized bed riser, a solid separator (the receiver), a standpipe (the annulus) and a reservoir. Cold flow experiments have been carried out with Geldart B sand to verify proper control of the system, as a preliminary step toward high temperature experiments. The solid circulation rate can be regulated through the riser fluidization velocity and match the design target of 1.4 g/s. Pressure measurements have been used to monitor and control the bed level in the annulus. Internal gas flow patterns have been determined by a gas tracing technique, indicating that undesired gas by-passing streams are very small and can be zeroed by regulating the operating conditions. An in-house built high-flux solar simulator has been used for high temperature experiments. A characterization of the heat exchanger was carried out by operating the prototype with the same inert sand. The results have been used to validate the compartmental model, extended to simulate transient operation. The heat transfer coefficient ranges between 370 and 540 W/(m^2 K) and a heat recovery factor of 90% has been calculated. The receiver temperature reached 700°C and was sufficiently high to perform calcination tests with $MgCO_3$, providing a first demonstration of the working principle of the DIFBAR under

reactive conditions. The work done lays the groundwork for future studies aiming at the optimization of the reactor and testing new solar processes.

Preface

Clean energy technologies are urgently needed to stop global warming, by zeroing greenhouse gas emissions. The transition from fossil to renewable sources is a necessary task for our societies, that will require the joint efforts of the scientific community, politicians and private companies. This transition must not only respond to the immediate threats of climate change, but also to the needs of maintaining affordable prices, to pursue social equity and economic wealth, and of ensuring a stable and secure supply of energy and essential goods.

Solar energy has a potential to address all these issues: it is clean and is available in every continent. Sun radiation can be exploited to produce heat and electricity. Photovoltaic (PV) cells directly convert solar energy into electricity and have seen an impressive development in the past decade, becoming the leading technology on the solar market with 760 GW of capacity globally installed in 2020. Sun rays are used to heat water for domestic or industrial use, by means of concentrating mirrors. Concentrated solar radiation can also supply heat to conventional thermal power stations to produce electricity. This application, known as Concentrating Solar Power (CSP), has started to be implemented on a commercial scale in many countries around the world, (the global installed capacity in 2020 was 6 GW) proving to be economically sustainable, and can be improved in many ways through research and development.

A primary obstacle to the development of solar technologies is the intermittency of sun irradiation due to Earth’s rotation and weather variability. The development of energy storage systems is the main technological challenge for the use of sun energy. Batteries and electrolyzers can store the electric energy produced by PV panels by electrochemical reactions, but their use in the future might be limited by the scarcity of raw materials. Adiabatic tanks can store thermal energy and are being used to improve the stability and flexibility of CSP plants and to extend the operation during off-sun periods. The use of solid materials as thermal energy storage media is regarded as an important improvement of current systems. Solid materials can also exploit solar energy to drive endothermic reactions for the production of energy carriers and materials. This might considerably expand the applications of concentrating solar technologies from the heat and power to the fuels and chemical sectors. For these reasons, the interest of researchers toward the development of gas-solid receivers and reactors for the absorption and utilization of concentrated solar radiation has been growing exponentially in the past decades and fluidized bed technology can bring several advantages to meet the specific requirements of the absorption of concentrated solar radiation and to carry out thermochemical processes.

This Ph.D. work studies a new fluidized bed reactor, named Directly Irradiated Fluidized Bed Autothermal Reactor (DIFBAR), conceived for the utilization of solar energy by the *thermochemical route*. The main novelty of the reactor is the autothermal operation, consisting in the recovery of the sensible energy of the reaction products to preheat the inlet solid. Applied to an exothermic process, this allows to reach the process temperature without an external input of heat. By applying the same principle to a solar reactor, it is possible to reduce the input of solar energy required to run the process, and to increase the overall efficiency. With the DIFBAR, this is achieved by coupling a directly irradiated fluidized bed solar receiver and a solid-solid counter-current heat exchanger. In principle, for a given solar input, it is possible to reach any process temperature, by properly sizing the length of the heat exchanger. The presented activities span a three-years research program and have been conducted in the frame of the collaboration between the Department of Chemical and Materials Engineering for the Industrial Production (DICMAPI) of the University of Naples Federico II and the Institute of

Science and Technology for Sustainable Energy and Mobility (STEMS) of the Italian National Research Council (CNR).

Chapter I illustrates the state-of-the-art of CSP technology, discusses the main research lines in the field of solar-driven chemical processes and introduces the new reactor studied in this work.

Chapter II presents a compartmental model of the DIFBAR, based on steady state thermal balances and empirical equations, and the design calculations for Calcium Looping as a reference thermochemical process.

Chapter III relates the investigations on Chemical Looping Reforming for the solar-driven production of hydrogen, conducted in different laboratory reactors: a fixed bed reactor, a fluidized bed reactor and a directly irradiated fluidized bed, mimicking the receiver of the DIFBAR.

Chapter IV deals with the design and testing of an experimental prototype of the DIFBAR. A hydrodynamic study has been carried out, to verify proper control of the system. Preliminary heating and reaction tests have also been conducted, demonstrating the working principle of the reactor.

In the Appendix, an extension of the compartmental model is proposed to simulate transient operation and is compared with experimental results.

Acknowledgments

I would like to express my gratitude to all the people, that supported my work.

First of all, I thank Prof. Piero Salatino for his trust and advice during this challenging research project. I share and admire his clear and forward-looking ideas about the ecological transition.

I am grateful to my incomparable team of supervisors, Prof. Roberto Solimene, Dr. Maurizio Troiano and Dr. Claudio Tregambi, for their constant and competent guidance along this professional and personal growth path.

A special thank goes to the technical staff of the CNR in via Metastasio, Antonio Cammarota, Ernesto Marinò, Antonio Cante and Rino Bencivenga, for their priceless assistance on countless occasions.

I also thank Gennaro Somma for his support for the construction of the DIFBAR prototype.

I would like to mention my colleagues Francesca Di Lauro and Laura Molignano, who have undertaken their Ph.D. projects and worked alongside with me, sharing stressful and pleasant moments.

I dedicate this achievement to my family and to Francesca, my beloved “little feather”.

List of figures

List of tables

CHAPTER I

CONCENTRATING SOLAR THERMAL TECHNOLOGIES

I.1. Concentrating Solar Power and Thermal Energy Storage

Concentrating solar technologies exploit solar irradiation as a heat source, by means of an array of flat or parabolic mirrors (heliostats), that reflect the sun rays on a receiver (Pitz-Paal, 2020). The heliostats track the sun by rotating around one or two axes (Figure I.1). One-axis heliostats concentrate sun rays on a line (line focusing system), whereas two-axes heliostats concentrate them on a point (point focusing system).

The two main line focusing systems are the parabolic trough collector and the linear Fresnel reflector. The *parabolic trough* is the most mature technology (Figure I.2). It is composed by rows of parabolic reflectors with a single curvature rotating around their axes. Solar rays are focused on tubular receivers running along the axes of the reflectors, connected in parallel or in series. The *linear Fresnel reflector* is made of a set of parallel long flat mirrors, that reflect the sun rays on a linear receiver (Figure I.3). Simplicity and modularity are the major advantages of these systems.

Point focusing systems show more varied designs. The *central tower* receiver has reached full commercial development (Figure I.4). It consists of a large field of flat two-axes heliostats, focusing the solar rays on a receiver placed at the top of a tower. In the *beam-down* configuration a secondary reflector is placed at the top of the tower, to reflect the solar rays on a receiver placed on the ground (Figure I.5). The *parabolic dish* is a reflector with the shape of a circular paraboloid and rotates around two axes, concentrating the sun beams on its focus (Figure I.6). The dimensions of these systems are limited for structural reasons, and they can only concentrate a few tens of kW. Finally, a *spot Fresnel reflector* has been recently developed (Figure I.7), made of circular metallic stripes arranged on a dome structure, reflecting the rays on a spot (Al-Maaitah, 2022). The entire dome rotates around the focus point, acting as a magnifying lens. A 10 kW prototype has been successfully demonstrated.

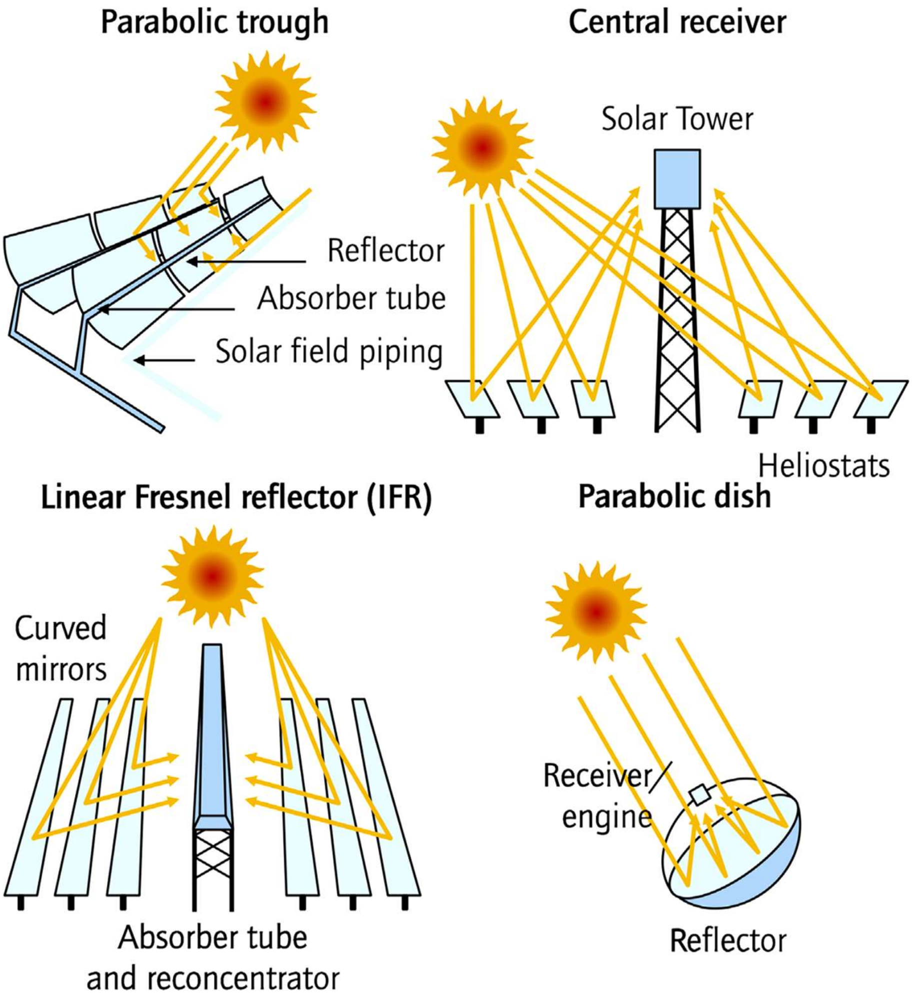

Figure I.1 Concentrating solar technologies.

Figure I.2 A parabolic through in the Mojave Desert in California, USA (Mojave Solar Project, 250 MW).

Figure I.3 A linear Fresnel reflector in Dhursar village in Rajasthan, India (Dhursar CSP, 125 MW).

Figure I.4 A central tower receiver in Ouarzazate, Morocco (NOOR III, 150 MW).

Figure I.5 A beam-down concentrator under construction in the Jiquan prefecture, PRC (Yumen Xinneng, 50 MW).

Figure I.6 A parabolic dish at the Plataforma Solar de Almería near Tabernas, Spain (EURODISH, 10 kW).

Figure I.7 The spot Fresnel reflector at the Masdar Institute Solar Platform near Abu Dhabi, United Arab Emirates (ASC-10, 10 kW).

Concentrating technologies are characterized by their concentration factor, that can be defined as the ratio between the total area of the collectors ($A_{collectors}$) and of the minimum surface area (A_{focus}) on which the total collected radiation is concentrated:

$$C = A_{collectors} / A_{focus} \tag{I.1}$$

The useful power absorbed by a perfectly insulated ideal blackbody receiver can approximately be calculated as:

$$P = I\, A_{collectors} - \sigma_{SB}\, T^4\, A_{focus} \tag{I.2}$$

Where I is the incident solar radiation flux, σ_{SB} is the Stefan-Boltzmann constant and T is the receiver temperature (Fletcher and Moen, 1977). The collection efficiency would be:

$$\eta_{collection} = (I\ A_{collectors} - \sigma_{SB}\ T^4\ A_{focus}) / I\ A_{collectors} = 1 - \sigma_{SB}\ T^4 / I\ C \qquad (I.3)$$

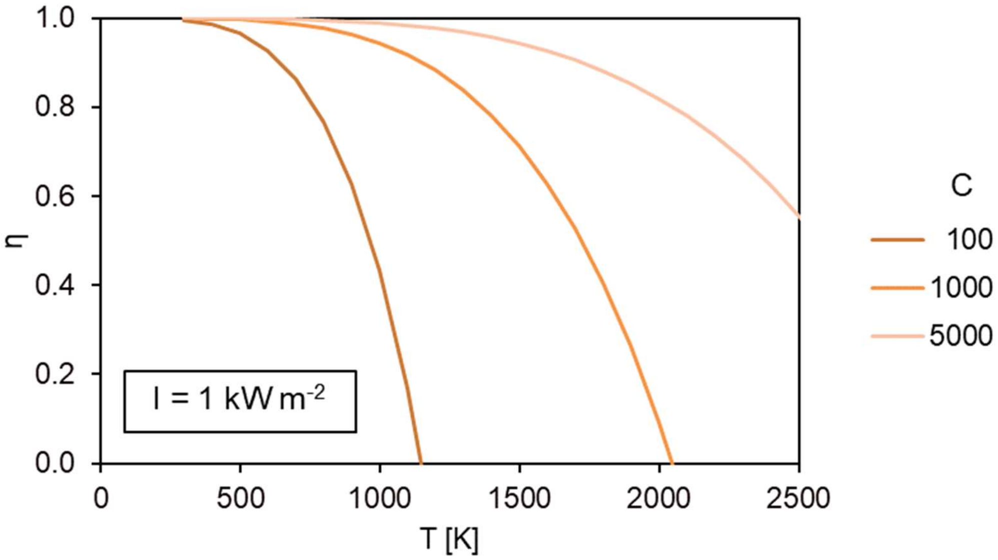

Figure I.8 Efficiency of a perfectly insulated blackbody receiver.

This simple calculation shows that high concentration factors are required to operate at high temperatures with acceptable efficiency. Point focusing systems allow to reach the highest concentration factors and so to work with higher temperatures.

In Concentrating Solar Power (CSP) plants, the energy absorbed in the receiver is used to supply a thermodynamic power cycle for the production of electric energy. In direct systems, the working fluid is heated in the receiver. In indirect systems a Heat Transfer Fluid (HTF) absorbs solar energy and then transfers heat to the working fluid. Thermal Energy Storage (TES) allows to extend the operation of the power plant after sunset, when solar radiation is not available and energy demand is higher, increasing the revenues (Liu et al., 2016). In active TES systems thermal energy is stored by temporarily accumulating the hot HTF in an adiabatic tank. In passive TES systems a TES material packed in a storage tank exchanges heat with the HTF, alternatively absorbing and releasing heat (charging and discharging). Molten salts mixtures are used today as HTFs and TES media in state-of-art plants (Fernández et al., 2019). Research is focusing in reducing storage volumes by increasing the heat capacity with solid particles and Phase-Change Materials, filling the storage tank or suspended by the HTF. However, the working temperature of these fluids is bounded below 600 °C due to problems of corrosion and thermal degradation. An interesting alternative is the use of granular solid materials as HTFs and TES media (Ho, 2016). Many of them can withstand temperatures of over 1000°C and could enable the implementation of high efficiency power cycles. In addition, some of them are involved in high temperature chemical processes, and this might provide new market opportunities for concentrating solar technologies and help to decarbonize other industrial sectors.

I.2. Solar-driven chemical processes

Concentrating solar technologies can deliver a large quantity of heat to receiver at high temperature and so have the potential to sustain endothermic chemical reactions. This might be exploited for the production of energy carriers and materials through innovative or traditional processes (Yadav and Banerjee, 2016).

One possibility is Thermochemical Energy Storage (TCES) (André et al., 2016; Carrillo et al., 2019). It consists in storing thermal energy by running an endothermic reaction. The chemical products have a higher enthalpy than the reactants and can release heat through the reverse exothermic reaction. They can be stored for unlimited periods and used at any time when needed. The main advantage with respect to existing TES systems is the possibility to implement long period storage strategies. Applied to a CSP plant, it would be possible to store excess sun energy during long summer days and spend it gradually during winter. By consequence it would be possible to better meet the energy demand throughout the year, by adapting the plant operation to seasonal changes, and to optimize the size of the heliostat field.

Another possibility is the production of sustainable fuels and materials. Many innovative processes aim at the production of hydrogen (H_2), carbon monoxide (CO) or a mixture of them (synthesis gas). These gases can then be used to power gas turbines and fuel cells, but also for advanced chemical synthesis.

I.2.1 Sorption cycles

Sorption cycles can be implemented for TCES. By these processes, the endothermic chemical desorption of a gaseous molecule from a solid sorbent is used to store thermal energy. The stored energy can be released on demand through the reverse adsorption reaction, fixing again the gaseous compound on the sorbent.

Carbonates can be employed through calcination/carbonation cycles. This is the case of the Calcium Looping process (Edwards and Materić, 2012). Calcium carbonate ($CaCO_3$) calcines above 750 °C in air through the reaction:

$$CaCO_3 \rightarrow CaO + CO_2 \qquad \text{(I.4)}$$

Calcium oxide (CaO) can then be stored and used to produce energy, by the reverse reaction with carbon dioxide (CO_2) at 650-750°C. This process is an ideal candidate for TCES, due to the large enthalpy change of the reaction ($\Delta H_{298} = 178$ kJ/mol). CO_2 for the carbonation step can be fed from flue gases. By calcining $CaCO_3$ in a pure CO_2 stream at 900°C, this process can be effectively employed for Carbon Capture and Storage (Tregambi et al., 2019).

The availability of limestone, a cheap natural source, is a considerable advantage. The major drawback is that the reactivity of this material decays cycle after cycle, due to sintering. Different carbonates have been studied to achieve higher stability and storage density (André and Abanades, 2017; Di Lauro et al., 2021).

Hydroxides can be analogously employed through dehydration/hydration cycles but at lower temperatures. Calcium hydroxide ($Ca(OH)_2$) has been intensively studied and is regarded as a promising TCES material (Schaube et al., 2012; Criado et al., 2014; Pardo et al., 2014).

I.2.2 Redox cycles

Redox cycles usually involve a metal oxide, that is cyclically reduced and oxidized, acting as an oxygen carrier. When employed for TCES, solar energy is stored through the endothermic reduction step, releasing oxygen (O_2):

$$MO_x \rightarrow MO_{x-y} + y/2\ O_2 \qquad (I.5)$$

Then, the oxygen carrier is re-oxidized through the reverse reaction, releasing the stored energy (Block and Schmücker, 2016). Both the reduction and oxidation steps can be carried out with air, which is a considerable advantage.

Another possibility is the production of synthesis gas (Agrafiotis et al., 2015). In this case the reduced oxide is used to split H_2O or CO_2, producing H_2 or CO and regenerating the oxygen carrier:

$$MO_{x-y} + y\ H_2O \rightarrow MO_x + y\ H_2 \qquad (I.6)$$

$$MO_{x-y} + y\ CO_2 \rightarrow MO_x + y\ CO \qquad (I.7)$$

The overall reaction is the decomposition of H_2O\CO_2. The fuel gas and O_2 output streams are produced in separated steps, so they cannot form explosive mixtures. In this case, the reduction step typically requires temperatures of 1000-1500°C and extremely low O_2 partial pressures, usually obtained by vacuum pumping or inert gas sweeping. Methane (CH_4) can be used in the reduction step to lower the reaction temperature at 900°C and to enhance the production of syngas (Krenzke et al., 2017):

$$MO_x + y\ CH_4 \rightarrow y\ MO_{x-y} + 2y\ H_2 + y\ CO \tag{I.8}$$

The resulting overall reaction in this case is steam\dry reforming and the process is known as Chemical Looping Reforming. In principle, 4 moles of syngas can be produced from 1 mole of CH_4 per each cycle with a $H_2 : CO$ ratio, that varies between 1 and 3 depending on whether CO_2 or H_2O is split during the oxidation step. The produced syngas has a total energy content higher than the CH_4 feed and can be used to produce advanced fuels.

The selection of suitable oxygen carriers is a wide research field. The desired properties are feasible reduction temperatures, high re-oxidation rates and good stability over cycles.

Some oxygen carriers selected for TCES are common to Chemical Looping Combustion technology. A detailed experimental study has been conducted by the American company General Atomics, in collaboration with the German Aerospace Center (DLR) (Wong et al., 2011). Barium (BaO_2), manganese (Mn_2O_3), iron (Fe_2O_3), cobalt (Co_3O_4) and copper oxide (CuO) have been considered as promising candidates.

Different oxygen carriers have been selected for the production of syngas (Roeb et al., 2012; Scheffe and Steinfeld, 2014). Volatile oxides release metal vapors, when reduced. Zinc oxide (ZnO) falls in this category and has been long studied (Steinfeld, 2002). The efficient separation of the metal vapor from the product gas, to avoid the recombination with O_2, is a fundamental aspect to consider (Alxneit, 2008). On the other hand, non-volatile oxides have the advantage of remaining in a condensed state, when reduced. Magnetite (Fe_3O_4) was the first oxide to be proposed for solar-driven thermochemical splitting and belongs to this category (Nakamura, 1977). Mixed oxides have also been investigated as ferrites (Ehrensberger et al., 1995; Tamaura et al., 2001), aluminates (Muhich et al., 2015) and perovskites (Scheffe et al., 2013), proving a higher stability during the high temperature reduction step.

Despite limiting the oxygen capacity, partial reduction of non-stoichiometric oxides shows some beneficial aspects. Non-stoichiometric oxides preserve their crystal phase, by letting oxygen diffuse through their lattice, through the formation of vacancies. Among the advantages are moderate reduction temperatures, fast kinetics of re-oxidation and good stability. Ceria (CeO_2) is a reference material of this kind (Panlener et al., 1976). The use of dopants enhances the stability of lattice defects and yields higher reduction degrees (Scheffe and Steinfeld, 2012; Luciani et al., 2019). Perovskites are also non-stoichiometric oxygen carriers (Scheffe et al., 2013). They are characterized by the presence of two cations and represented with the general formula ABO_3. Partial substitution of the A and B cations can be used to tailor the redox properties (Luciani et al., 2018). Lanthanum (La) - Fe and La - Mn perovskites, in which strontium (Sr) partially replaces La in the A-sites, have been found particularly suited for Chemical Looping Reforming, thanks to their high selectivity toward partial oxidation of CH_4 (Evdou et al., 2008, 2010; Donat et al., 2020).

I.2.3 Thermochemical up-grade of carbon-based feedstocks

Solar energy can also be exploited for the up-grade of carbon-based feedstocks (either fossil or bio-based) to fuels, through thermochemical conversion processes (Nzihou et al., 2012). Solar reforming of CH_4 and solar gasification of coal/biomass generally consist in the endothermic reaction of the feedstock with H_2O (or CO_2) at very high temperatures 800-1500 °C to produce synthesis gas (Puig-Arnavat et al., 2013; Agrafiotis et al., 2014; He and Li, 2014). Solar-driven processes have several advantages compared to the traditional ones, in which a considerable part of the feedstock is burnt to supply the reaction heat.

Solar pyrolysis is the main alternative process: it consists in the thermal decomposition of the feedstock under inert atmosphere. The decomposition of CH_4 occurs above 550°C and produces a pure H_2 stream and solid carbon (C) (Hirsch et al., 2001), according to the reaction:

$$CH_4 \rightarrow C + 2\ H_2 \tag{I.9}$$

Pyrolysis of coal/biomass occurs above 400°C and displays a wide spectrum of products, distributed among a C-rich solid (char), condensable vapors (tars and H_2O) and incondensable gases (CH_4, H_2, CO, CO_2), whose yields generally depend on process temperature and gas-solid contact time (Troiano et al., 2022). The tar vapors can be condensed to obtain a liquid feedstock (bio-oil), that can be further up-graded through thermocatalytic processes to conventional fuels and chemicals. On account of this aspect, biomass pyrolysis is considered with great interest as the initial step of the supply chain of a new biorefinery model.

I.3. Gas-solid solar receivers and reactors

Gas-solid solar receivers and reactors have been developed and tested at laboratory and pilot scales. Experimental research is carried out either with solar furnaces or solar simulators. Solar furnaces are facilities equipped with heliostats of various types to concentrate sunlight. Solar simulators are usually made by a short-arc lamp coupled with elliptical reflector. Gas-solid *solar* *receivers* are mainly conceived to produce hot air for a Brayton cycle (Nie et al., 2022). Solids are used both for the effective absorption of solar radiation and as TES media. In indirectly irradiated receivers an intermediate element absorbs solar radiation and heats the solid by conduction or re-emission. In directly irradiated receivers, the solid is exposed to the concentrated sunlight, passing through an optical aperture. The aperture can be sealed with a transparent window to minimize convective losses and to collect the outlet gas. A *solar reactor* is usually a solar receiver, that also acts as a chemical reactor (Zsembinszki et al., 2018). In some cases, solar reactors are operated in batch mode, alternating a charge and a discharge phase by a temperature swing or changing the gas composition. In other cases, solar reactors are operated in continuous mode and the exothermic process is eventually carried out in a secondary reactor.

The efficiency of solar reactors has been defined in several ways in literature (Bulfin et al., 2021). A generic definition can be given as:

$$\eta = 1 - E_{lost} / E_{input} \tag{I.10}$$

Where E_{lost} is the total amount of energy losses and E_{input} is the amount of energy supplied to the reactor. However, these terms differ depending on the choice of the system boundary and on whether the energy balance includes the mechanical energy of material streams (provided by auxiliary components as pumps, blowers and feeders) and mobile parts (drums, impellers, shafts, …). By considering the thermal balance on the reactor unit, two definitions can be given. The total efficiency is defined as the ratio between the total energy absorbed by the reactor (sensible and chemical) and the total energy irradiated:

$$\eta_{tot} = (Q_{sensible} + Q_{reaction}) / Q_{solar} \tag{I.11}$$

The chemical efficiency is defined by the ratio between the energy absorbed by the chemical reaction and the total energy irradiated:

$$\eta_{chem} = Q_{reaction} / Q_{solar} \tag{I.12}$$

The energy absorbed to raise the temperature of the feed streams ($Q_{sensible}$) is accounted as useful energy according to the first definition and as a loss according to the latter. It follows that the chemical efficiency is always lower than the total efficiency. The total efficiency is suitable when both sensible and chemical energy are exploited for instance to heat the working fluid of a power cycle, operating round the clock. The chemical efficiency is more appropriate when the goal is only the production of an energy carrier, that is cooled at room temperature. Anyway, these efficiencies are not intrinsic performance parameters of a given reactor design, as they greatly depend on the process that is carried out.

According to the multiphase flow regime, gas-solid receivers and reactors have generally been divided into stacked, entrained, and fluidized beds (Alonso and Romero, 2015). In the following paragraphs the state-of-the-art of these technologies is discussed by reporting some notable examples found in literature.

I.3.1 Stacked beds

Stacked beds are characterized by high solid fractions and low solid velocities, and include fixed\packed, moving and rotating beds. Some experimental applications are summarized in Table I.1 and detailed in the following text. Fixed bed reactors benefit from low costs and easy operability. A relevant example is the indirectly irradiated packed bed reactor, developed at the Paul Scherrer Institute (PSI) for the combined reduction of ZnO and gasification of coal (Osinga et al., 2004) and for the steam gasification of carbonaceous feedstocks (Piatkowski et al., 2009). The reactor features two cavities separated by a graphite partition. The upper cavity is a solar receiver closed by an optical window and the lower cavity is the reaction chamber, hosting the packed bed. The graphite partition absorbs solar energy and heats the bed from above by re-emission. A pilot plant was successfully tested at the solar furnace of the Weizmann Institute of Science (WIS) with a power input of 300 kW (Wieckert et al., 2007). The total efficiency reached up to 30%.

Porous structured packings have also been investigated. By adjusting the porosity, it is possible to have deeper penetration lengths of the incident radiation and better thermal conductivities. The use of reticulated porous ceramic (RPC) foams in directly irradiated reactors has been deeply studied for thermochemical splitting of H_2O with CeO_2. A CeO_2-coated RPC foam support made of zirconia has been realized at the University of Niigata and tested at the 40 kW solar furnace of the Korea Institute of Energy Research (KIER) (Cho et al., 2015). In order to obtain a better compromise between a low extinction coefficient and a large surface area, a dual-scale porosity RPC foam made of CeO_2 has been investigated at the Swiss Federal Institute of Technology (ETH), with mm-size pores to enable the volumetric absorption of concentrated solar radiation and μm-size pores to offer a large specific area (Ackermann et al., 2017). Another remarkable case of a porous structured reactor is the TCES system, that has been tested at the DLR Solar Tower in Jülich, made of a honeycomb cordierite support coated with 90 kg of Co_3O_4 (Tescari et al., 2017). Although in this case the reactor is indirectly heated by a side stream of air coming from the receiver. By combining RPC technology with direct air carbon capture and Fischer-Tropsch synthesis, the ETH has demonstrated the complete production chain of solar fuels with a pilot plant (Schäppi et al., 2022). This technology has provided the basis for the creation of the first start-up, producing solar fuels at commercial scale (Synhelion, 2022).

Rotary kilns are praised for good solid mixing, flexibility and simple control and were proposed to be coupled with CST technology for the calcination of $CaCO_3$ for the first time in 1980 (Flamant et al., 1980). They can process solids in continuous mode within a very wide range of particle sizes. A directly irradiated rotary kiln has been developed at the DLR and tested with a solar simulator. The kiln is designed to process a continuous flowrate of solid. During a first campaign heating tests were carried out and a predictive model was validated (Tescari et al., 2018). Then, the reactor was tested for the calcination of cement raw meal powder of micrometer size and for the reduction of Mn-Fe mixed oxide particles of millimeter size (Tescari et al., 2020). Both experiments were carried out in an air atmosphere. Due to the deposition of fines on the optical window, the tests with the CRM powder had to be performed in a windowless, open configuration (Moumin et al., 2019). The total and chemical efficiency were respectively in the range between 19.1 - 39.6 % and 10.7 - 16.4 %, by varying the solid flowrate between 4 - 12.4 kg/h. The tests with the Mn-Fe oxide particles were carried out at a flowrate of 10 - 11 kg/h and scored a total efficiency of 24.7 %, whereas a chemical efficiency of 2.2 % can be evaluated from reported data (Tescari et al., 2022).

A continuous directly irradiated rotating cavity reactor has been developed at the PSI for the thermal dissociation of ZnO. Due to the centrifugal force, the particles form a layer that thermally shields the reactor wall. The reactor has been tested both under real and simulated concentrated solar radiation (Haueter et al., 1999; Schunk et al., 2008). After that, a pilot-scale prototype has been realized and tested at the solar furnace of the French National Centre for Scientific Research (CNRS) in Odeillo with a power input of 100 kW, reaching a chemical efficiency up to about 3 % (Koepf et al., 2016).

Receiver type	**Operation modality**	**Irradiation**	**Test site**	**High Flux Source***	**Irradiated power [kW]**	**Maximum temperature [°C]**	**References**
Fixed bed	Batch	Indirect	PSI/ETH	SF/SS	4.0-10	1310	(Osinga et al., 2004; Piatkowski et al., 2009; Tzouganatos et al., 2016)
			WIS	SF	300	1177	(Wieckert et al., 2007)
Monolith	Batch	Indirect	DLR (Jülich)	SF	-	1100	(Tescari et al., 2017)
		Direct	ETH	SS	1.9-3.8	1500	(Ackermann et al., 2017)
			KIER	SF	8.8-16.7	1600	(Cho et al., 2015)
Rotary bed	Continuous	Direct	DLR	SS	10.2-14.2	1072	(Moumin et al., 2019; Tescari et al., 2022)
			CNRS (Odeillo)	SF	115	1790	(Koepf et al., 2016)
		Indirect	CNRS	SF	1.5	1030	(Abanades and André, 2018)

*SF = Solar Furnace, SS = Solar Simulator

Table I.1 Stacked bed technologies.

An indirectly irradiated design has been also proposed at the CNRS for the calcination of limestone. In this case the rotating reactor tube is placed inside a cavity receiver and heated through the lateral wall (Abanades and André, 2018).

I.3.2 Entrained beds

Entrained beds are characterized by very diluted particle flows and high velocities. The reviewed experimental applications are summarized in Table I.2. The solar vortex flow reactor (SVR) developed at the PSI must be mentioned (Steinfeld et al., 1998). Very fine solid particles (<50 µm) are fed to a cylindrical cavity and entrained by a gas vortex flow. Solar radiation is concentrated on the inlet side. Both direct and indirect irradiation have been tested (Hirsch and Steinfeld, 2004). Indirect heating resulted in higher efficiencies, but lower temperatures and conversion degrees. The reactor has been tested for the decomposition of CH_4 (Hirsch and Steinfeld, 2004) and steam gasification of petcoke (Z'Graggen et al., 2006; Z'Graggen and Steinfeld, 2008) with total and chemical efficiencies respectively in the range 10 - 20 % and 3 - 10 %. Uncommon applications have also been studied like the combined production of synthesis gas and Zn (Steinfeld et al., 1998) and of synthesis gas and lime (Nikulshina et al., 2009). A modified design has been proposed by the University of Adelaide, featuring a conical inlet located at the opposite side of the cavity's aperture (Chinnici et al., 2015). This configuration generates an expanding vortex flow, that mitigates particle deposition on the window and leads to the recirculation of larger particles, increasing their residence time and conversion degrees (Davis et al., 2020). Directly irradiated free-falling particle receivers have been studied for forty years at the Sandia National Laboratories (SNL) (Martin and Vitko, 1982). They cannot be strictly classified as entrained beds because the particle motion is driven by gravity rather than by drag force, but they also feature a very diluted high-velocity multiphase flow.

Receiver type	**Operation modality**	**Irradiation**	**Test site**	**High Flux Source***	**Irradiated power [kW]]**	**Maximum temperature [°C]**	**References**
Vortex flow	Continuous	Direct	PSI/ETH	SF/SS	3-6.6	1545	(Hirsch and Steinfeld, 2004; Z'Graggen et al., 2006)
Falling particles	Continuous	Direct	SNL	SF	1000	700	(Ho et al., 2017)

*SF = Solar Furnace, SS = Solar Simulator

Table I.2 Entrained bed technologies.

Solid particles are mechanically conveyed at the top of a tower and discharged from a hopper. During the fall, the free-falling particle curtain is exposed to concentrated solar radiation through an aperture. Large amounts of solids can be heated with short exposure times (Ho et al., 2017). This system has not been employed so far as a solar reactor. The major issues are the lack of a window closing the aperture, causing large energy losses and wind interferences (Tan and Chen, 2010).

I.3.3 Fluidized beds

Fluidized beds can be regarded as an intermediate regime between stacked and entrained beds, in which void degrees and velocities can be significantly varied. Thanks to their excellent heat transfer properties, fluidized beds have been recognized as a suitable solution for the absorption of concentrated solar energy since the 1980s (Flamant, 1982) and in the last ten years the development of fluidized bed solar receivers and reactors has seen an acceleration thanks to innovative designs (Table I.3) (Tregambi et al., 2021). Large thermal diffusivities allow to spread the heat from the irradiated spot to the entire volume of the reactor (Tregambi et al., 2016). Uneven fluidization has been investigated as a means to enhance thermal diffusion by inducing large-scale convective stream of the particles and at the same time to reduce convective energy losses (Salatino et al., 2016).

The idea of uneven fluidized beds has been explored by the University of Naples Federico II and the Italian National Research Council (CNR) with the compartmented fluidized bed receiver, designed to perform the different tasks of CST energy collection, storage and delivery in a single unit (Solimene et al., 2017). This concept has been demonstrated in two commercial pilot plants ("STEM®-CST Concentrated Solar Thermal,"), built and successfully operated by the Italian company Magaldi, one rated at 100 kW, the other at 2 MW peak radiative power.

Receiver type	**Operation modality**	**Irradiation**	**Test site**	**High Flux Source***	**Irradiated power [kW]**	**Maximum temperature [°C]**	**References**
Bubbling	Batch	Direct	CNR	SS	3.2	1100	(Tregambi et al., 2019)
		Indirect	NREL	SF	10	1500	(Hoskins et al., 2019)
	Continuous	Indirect	CNRS (Odeillo)	SF	10	750	(Zhang et al., 2017)
Compartmented	Batch	Direct	Magaldi (Messina)	SF	2000	1000	(STEM®-CST Concentrated Solar Thermal)
Internally circulating	Batch	Direct	Niigata university	SS	1.2-5.1	1200	(Gokon et al., 2008, 2019)
			Miyazaki university	SF	100	1100	(Kodama et al., 2019)
Spouted	Continuous	Direct/ Indirect	CNRS (Odeillo)	SF	1.5	1400	(Bellouard et al., 2017; Chuayboon et al., 2019)
Multistage crossflow	Continuous	Indirect	CNRS (Odeillo)	SF	10-50	800	(Esence et al., 2020a, 2020b)

*SF = Solar Furnace, SS = Solar Simulator

Table I.3 Fluidized bed technologies.

A directly irradiated internally circulating fluidized bed reactor has been developed at the University of Niigata, based on the same principle. The reactor features a central draft tube and an annulus region: thanks to different fluidization velocities, the particles are transported upward in the draft tube and move downward in the annulus region. The beneficial effects on the temperature distribution and on the reactor performance have been experimentally demonstrated (Gokon et al., 2008, 2010, 2012, 2015). During first experimental campaigns, the reactor was tested with a solar simulator for the reduction of nickel ferrite ($NiFe_2O_4$) supported on zirconia particles (ZrO_2) in a N_2 flow (Gokon et al., 2008). The effects of particle size and of the catalyst support were investigated (Gokon et al., 2009). Also, several redox cycles were performed to produce H_2, by switching the gas feed from pure N_2 to a mixture of H_2O and N_2 (Gokon et al., 2011). Conversion degrees about 40% were obtained with cycle efficiencies less than 1%. Successively, the reactor was also tested for the gasification of coal coke with CO_2 (Gokon et al., 2012) and steam (Gokon et al., 2014, 2015), with conversion degrees above 60% and average chemical efficiencies that can be estimated around 5%. Recently, the internally circulating fluidized bed reactor has been scaled-up and has started to be tested at the 100 kW beam-down solar furnace of the University of Miyazaki (Kodama et al., 2019). Another example of an uneven fluidized system is the spouted bed reactor developed at the CNRS for the gasification of biomass (Bellouard et al., 2017). The reactor can operate with a continuous feed of biomass. Both a direct and indirect heating configurations have been studied. Indirect irradiation resulted in lower temperatures, but higher conversion degrees were attained (up to 97%). Different types of biomasses have been tested with mean particle sizes ranging from 0.3 to 4 mm (Chuayboon et al., 2019). An optimal operating condition has been found for a resinous mix (0.55 mm), scoring a total efficiency of 26% and a chemical efficiency of 8.3 %.

In order to exploit the large bed-to-wall heat transfer coefficients of dense suspensions, many authors have thought to concentrate solar radiation on the lateral walls of fluidized beds. A pair of twin indirectly irradiated fluidized bed reactors has been tested for the reduction of hercynite particles at the 10 kW solar furnace of the National Renewable Energy Laboratory (NREL) (Hoskins et al., 2019). Dense circulating systems have been developed, both with up- (Zhang et al., 2017) and downflowing bubbling fluidized beds (Miller et al., 2018), to have a continuous throughput of a heated solid. The upflowing bubbling fluidized bed concept was tested at the 4 MW Themis solar furnace ("Next - CSP project").

Finally, in order to improve the control of the residence time of the solid phase, a cross-flow fluidized bed composed of multiple horizontal stages has been proposed (Kong et al., 2018) and a 50 kW prototype has been tested for the calcination of dolomite at the CNRS (Esence et al., 2020a).

I.4. The Directly Irradiated Fluidized Bed Autothermal Reactor (DIFBAR)

The recovery of the sensible energy of the products to preheat the reactants, that characterizes an autothermal reactor, has been recognized as a key strategy to increase the efficiency of solar reactors through analytical models (Ermanoski et al., 2013; Falter and Pitz-paal, 2018). A technical implementation of this principle has been proposed for the first time with a new concept of fluidized bed reactor, named Directly Irradiated Fluidized Bed Autothermal Reactor (DIFBAR), developed by the collaboration between the University of Naples Federico II and the CNR. Figure I.9 illustrates the working principle of the DIFBAR.

The DIFBAR consists in a conical cavity receiver connected at the bottom with two vertical coaxial tubes (Figure I.9). The bed material is fed to the receiver through the inner tube (riser) by a fluidizing gas stream. There, the particles are exposed to a high flux of solar radiation and separate from the gas stream falling into the outer tube (annulus). The material descends through the annulus as a moving bed and transfers its sensible heat to the granular suspension flowing up through the riser. In this way a solid can be processed continuously, by recovering its sensible energy to preheat the feed.

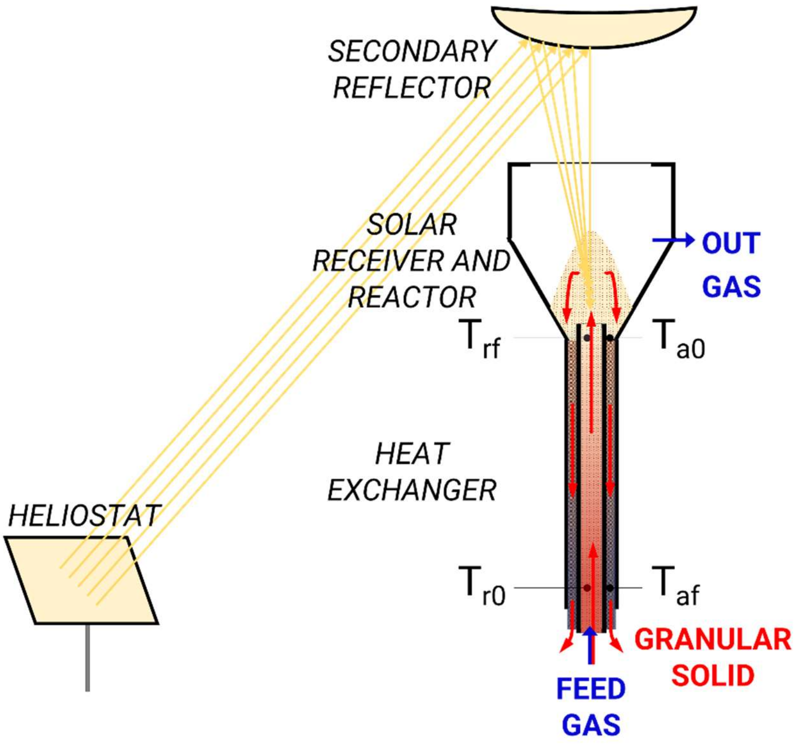

Figure I.9 DIFBAR concept.

The riser and the annulus work as a double pipe countercurrent heat exchanger and are expected to be characterized by parallel temperature profiles like the ones in Figure I.10. The temperature difference through the heat exchanger is sustained by the absorption of concentrated solar radiation inside the receiver. In principle, for a fixed temperature difference - that is for a fixed power absorbed by the solid inside the receiver - it is possible to reach any temperature by properly sizing the length (L) of the heat exchanger.

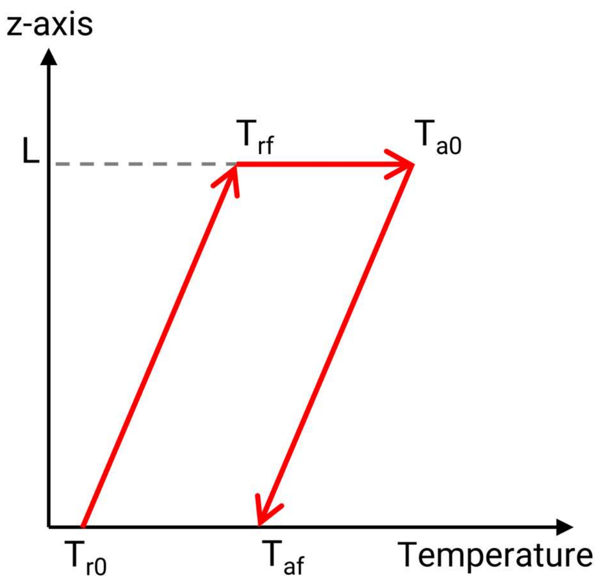

Figure I.10 Qualitative temperature profile of the heat exchanger.

Two alternative plant schemes are considered for handling the solid:

- In the “Dual Tank” scheme the feed and product streams of the solid are collected in separate tanks (Figure I.11, left). The reacted material can be sent to an exothermic reactor for a regeneration step and then returned to the feed tank.
- In the “Single Tank” scheme (Figure I.11, right), the solid material is continuously recirculated between the receiver and a single reservoir, that can eventually be operated as an exothermic reactor.

The Single Tank scheme is more compact and can be favored for volume saving. When operated as a storage tank, the mixing of the product and the reactant solids should be avoided, to prevent the reacted solid to be sent back to the receiver. In this case the solid should flow down as a moving bed, approximating a plug flow. If the reservoir is employed as a reactor, fluidized bed conditions might be preferable. In any case this design has the advantage of reducing the plant volumes. Gas by-passing from the reservoir to the receiver or vice versa is undesired and must be avoided by a proper design and control.

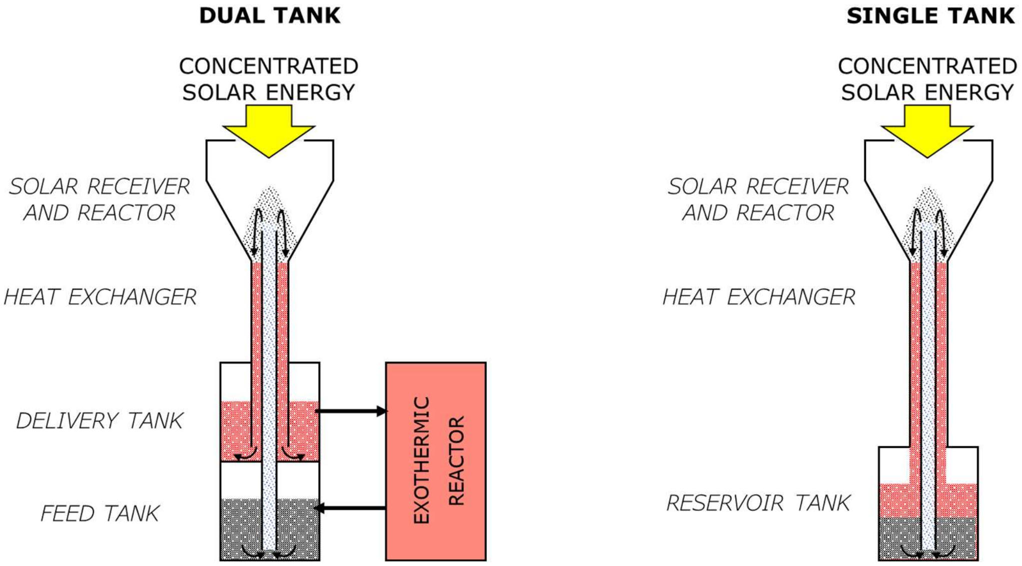

Figure I.11 DIFBAR alternative schemes for solid handling: Dual Tank (left) and Single Tank (right).

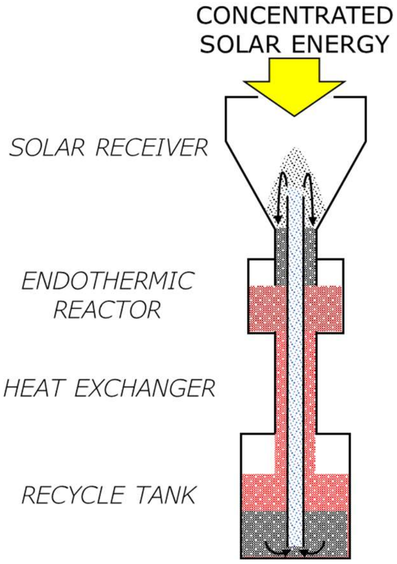

Figure I.12 Shaded reactor configuration.

Two different configurations are also conceived for the reactor:

- In the base configuration, the reaction takes place in the receiver, so the reactor and the receiver coincide.
- In the alternative “Shaded reactor” configuration (Figure I.12), the reaction and the absorption of solar radiation take place in two different vessels. In this way the gas products are collected separately, without mixing with the riser fluidizing gas.

The operation principle of a counter-current solid-solid heat exchanger coupled with a solar receiver has been demonstrated with a stainless steel prototype of the Single tank configuration, heated by an in-house built high-flux solar simulator. Very favorable overall heat transfer coefficients were found, ranging between 400 and 700 W m^{-2} K^{-1}, though the experiments were performed at relatively low temperatures (100-175°C) (Tregambi et al., 2020a). Then, a smaller experimental unit was built, that can reach up to 1200°C(Tregambi et al., 2020b). This unit lacks any storage tank (the annulus and the riser are directly connected) and has a very small heat exchange area, so its effect is very limited. However, the unit reproduces the receiver part of the DIFBAR and allows to explore operability limits and to perform reactive tests with a small inventory, serving as a perfect test unit for preliminary studies of solar processes. Operability limits were assessed for different materials under inert conditions, and Calcium Looping cycles were performed.

I.5. Aim of the Ph.D. thesis

This Ph.D. thesis aims at the first complete proof-of-concept of the DIFBAR. To this end a new prototype has been designed and built, to carry on a high-temperature process with concentrated sunlight and to show the beneficial effect of the heat recovery. At the same time, preliminary investigations on a thermochemical process for the solar-driven production of hydrogen have been conducted in different laboratory reactors, in view of an application with the new DIFBAR prototype. The main contributions of the thesis are:

- The implementation of a compartmental model of the DIFBAR, based on thermal balances and empirical equations, as a design tool. The design and performance of the DIFBAR as a “thermochemical battery” has been assessed through model calculations.

- Investigations on Chemical Looping Reforming with a laboratory-produced perovskite in different laboratory reactors: a fixed bed reactor, a fluidized bed reactor and the DIFBAR receiver test unit, employed in previous experiments (Tregambi et al., 2020b).

- The design, construction and testing of a new prototype of the DIFBAR. A hydrodynamic study has been conducted to verify proper control of the system, by measuring solid flowrates, pressure loops and gas by-passing flowrates. The efficiency of the heat exchanger has been assessed by heating the receiver with a high-flux solar simulator. Preliminary reaction tests demonstrated the working principle of the reactor.

CHAPTER II

MODEL OF DIFBAR AS THERMOCHEMICAL BATTERY

II.1. Design and operation of the thermochemical battery

In principle, the DIFBAR can be employed for any solar-driven chemical process. For the purposes of this thesis, the application of the DIFBAR for TCES has been conceptualized through the idea of the “thermochemical battery”, that consists of two alternative operation modes: the charge mode, during which solar energy is stored by means of an endothermic reaction, and the discharge mode, during which the stored energy is released by the reverse reaction. The Single Tank scheme is particularly suited to this idea, as the reservoir can be operated to store the product of the charge reaction and to perform the discharge reaction, by holding a constant temperature. In this way it would be possible to avoid or limit any transient heating phase, due to the switch between the two modes of operation.

The sizing of the heat exchanger is the starting point in the design of the DIFBAR. Steady state calculations have been performed for this purpose assuming a simple compartmental model. Calcium Looping has been taken as a reference process, on account of the previous work carried out by the research group (Tregambi et al., 2020b). The results, reported in this chapter, have been published in a scientific paper (Padula et al., 2021). The effect of key variables such as fluidization velocities and operation temperatures are discussed in terms of power and size requirements. Efficiency and reaction times are also evaluated. This study has provided the basis for the design and realization of a dedicated proof-of-concept prototype.

II.2. Compartmental model

The DIFBAR can be simulated with a compartmental model, as shown in Figure II.1. The pictured model represents the Single Tank scheme. Each compartment corresponds to a well-confined reactor zone, characterized by homogeneous flow conditions (the riser, the receiver, the annulus, the reservoir). As an exception, the riser inlet zone is considered separately, to catch the effect of the fast heat transfer between the primary gas and the solid recycled from the reservoir, occurring in an undetermined volume below the heat exchanger section. To simulate the transient behavior, it is necessary to consider internal variables, like volumes and void degrees. Moreover, a 1-D approach must be adopted to resolve the dynamic evolution of the temperature profiles along the heat exchanger. Under steady state conditions instead, each compartment can be simply characterized by the inlet and outlet variables with a 0-D approach. Steady state equations can be conveniently solved for design purposes with minimum information.

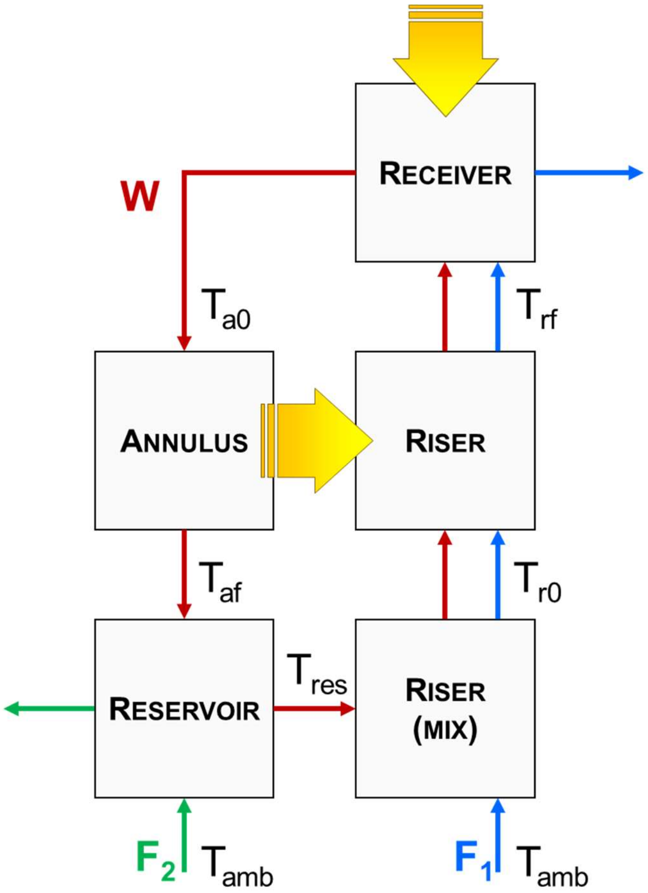

Figure II.1 Compartmental model of the DIFBAR with lumped parameters.

A transient model is described in the Appendix and has been applied as an analysis tool for the thermal characterization presented in Chapter IV. In this chapter, a steady state model is described and applied to perform design calculations. Equations are first written for inert operating conditions (purely thermal operation) and then are modified to account for reactive operative conditions.

II.2.1. Purely thermal operation

Thermal energy balances for purely thermal operation in each compartment read:

$$W\ H_{res} + F_1\ h_{in1} - W\ H_{r0} - F_1\ h_{r0} = 0 \tag{II.1}$$

$$P_{ex} + W\ H_{r0} + F_1\ h_{r0} - W\ H_{rf} - F_1\ h_{rf} = 0 \tag{II.2}$$

$$P_{net} + W\ H_{rf} + F_1\ h_{rf} - W\ H_{a0} - F_1\ h_{a0} = 0 \tag{II.3a}$$

$$W\ H_{a0} - P_{ex} - W\ H_{af} = 0 \tag{II.4a}$$

$$W\ H_{af} + F_2\ h_{in2} - W\ H_{res} - F_2\ h_{res} = 0 \tag{II.5a}$$

where W and F are the solid and gas flowrates, H and h are the solid and gas specific enthalpies (calculated with respect to 25 °C respectively on mass and molar basis), P_{net} is the net power absorbed in the receiver (not accounting for losses due to radiation or heat through the walls) and P_{ex} is the power exchanged between the annulus and the riser. The external walls are assumed adiabatic. By summing up Eqs. (II.1)-(II.5), the global balance can be obtained:

$$P_{net} + F_1\ h_{in1} + F_2\ h_{in2} - F_1\ h_{a0} - F_2\ h_{res} = 0 \tag{II.6a}$$

The global balance directly relates the three controllable variables of the system: the two gas flowrates and the energy input. The system is solved by assuming that the temperatures of the gas and solid streams exiting a same volume are identical. For system closure, two ancillary equations are needed:

$$P_{ex} = U\, a\, L\, \Delta T \tag{II.7}$$

$$W = K\,(Q_1 - Q_{min}) \tag{II.8a}$$

$$G_r = K\,(u_1 - u_{min}) \tag{II.8b}$$

Equation (II.7) expresses the thermal power exchanged in the heat exchanger between the uprising and descending solid, U being the heat transfer coefficient, a the heat exchange surface area per unit length of the riser, L the length of the annulus-riser heat transfer section and ΔT the driving force (calculated as the logarithmic mean temperature difference at the upper and lower cross sections of the heat exchanger). Equation (II.8a) is an empirical equation relating solid mass flowrate W to the primary gas volumetric flowrate Q_1: according to previous investigations a linear relation holds between W and Q_1, featuring a minimum flowrate (Q_{min}) to initiate solid circulation(Tregambi et al., 2020b). Gas volumetric flowrates are related to the relative molar flowrates by the ideal gas equation of state:

$$Q_i = F_i\, R\, T_i / p \tag{II.9}$$

The temperature of the secondary gas stream is assumed equal to the reservoir temperature T_{res}. The temperature of the primary gas stream is taken as the mean between the temperatures at the inlet and outlet of the riser, T_{r0} and T_{rf}, respectively. Equation (II.8b) is obtained from Eq. (II.8a) by dividing each term by the cross-section of the riser: G_r is the solid mass flux, u_1 is the primary gas velocity and u_{min} the minimum circulation velocity.

II.2.2. Charge operation

The calcination of limestone is considered as the charge reaction. The inventory is made of limestone with a mass fraction α of calcium carbonate and a total mass m. The total amount of chemical energy (E) that can be stored and the charge efficiency (η) are:

$$E = m\,\alpha\,\Delta H_{298} / M_{CaCO3} \qquad \text{(II.10)}$$

$$\eta = E / (\, P_{net}\,\tau_r \,) \qquad \text{(II.11)}$$

$$\tau_r = m\,\alpha / \dot{n}\,M_{CaCO3} \qquad \text{(II.12)}$$

where M_{CaCO3} is the molar weight of $CaCO_3$, ΔH_{298} is the molar enthalpy change of the calcination reaction at 25 °C, τ_r is the time for complete $CaCO_3$ conversion. $\dot{n}$ is the product molar rate of the reaction, calculated by assuming that the reaction reaches equilibrium. At thermodynamic equilibrium, the partial pressure of CO_2 is given by Eq. (12):

$$p\,y_{eq} = p_{atm}\exp(\,-\Delta G° / RT\,) \qquad \text{(II.13)}$$

where p is the total pressure of the receiver and y_{eq} is the molar concentration of CO_2. Then the product molar rate for complete thermodynamic conversion is calculated as follows:

$$\dot{n}_{eq} = F_1\,y_{eq} / (1 - y_{eq}) \qquad \text{(II.14)}$$

This value increases with temperature and becomes larger, the closer the equilibrium partial pressure of CO_2 to the total pressure of the receiver. A temperature T* exists beyond which the product molar rate $\dot{n}_{eq}$ is bounded by the maximum complete stoichiometric conversion of the calcium carbonate stream fed to the receiver:

$$\dot{n}_{st} = W\,\alpha / M_{CaCO3} \tag{II.15}$$

Depending on the temperature, the actual product molar rate is taken as the minimum between the thermodynamic and the stoichiometric conversion limits:

$$\dot{n} = \min\{\dot{n}_{eq}, \dot{n}_{st}\}. \tag{II.16}$$

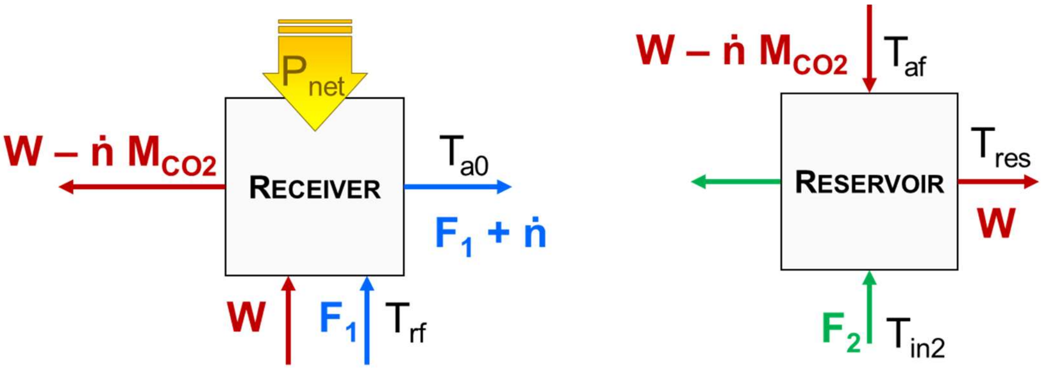

(a) (b)

Figure II.2 Balance scheme during charge operation for receiver (a) and reservoir (b).

It should be pointed out that η (Eq. II.11) is not the global energy storage efficiency: additional losses related to the receiver overall collection efficiency should be considered, i.e. the ratio between the total power of the radiative flux focused on the receiver and the net power absorbed. During charge operation, the energy balances must be modified in order to account for the thermal effect due to the course of the reaction, the material transfer between the solid and gas phases, and the solid mass loss due to the reaction, as detailed in Fig. II.2. In particular, the balance equations on the receiver, the annulus and the reservoir (Eqs. (II.3a)–(II.6a)) are modified as follows:

$$P_{net} + W\,H_{rf} + F_1\,h_{rf} - (W - \dot{n}\,M_{CO2})\,H_{a0} - F_1\,h_{a0} - \dot{n}\,\hat{h}_{a0} - \dot{n}\,\Delta H_{298} = 0 \qquad \text{(II.3b)}$$

$$(W - \dot{n}\,M_{CO2})\,H_{a0} - P_{ex} - (W - \dot{n}\,M_{CO2})\,H_{af} = 0 \qquad \text{(II.4b)}$$

$$dm_{res}/dt\;H_{res} = (W - \dot{n}\,M_{CO2})\,H_{af} + F_2\,h_{in2} - W\,H_{res} - F_2\,h_{res} \qquad \text{(II.5b)}$$

$$dm_{res}/dt = -\,\dot{n}\,M_{CO2} \qquad \text{(II.17)}$$

where $\hat{h}$ is the specific enthalpy of CO_2, M_{CO2} is the molar mass of CO_2 and m_{res} is the reservoir mass inventory. It is assumed that the solid circulation rate W and the specific enthalpy negligibly change with solid conversion. A mass balance on the reservoir (Eq. (II.17)) is added to account for the mass variation in the solid phase due to the CO_2 release. For the sake of simplicity, it is assumed that the reaction takes place only in the receiver, so the two balances on the riser (Eq. (II.1) and (II.2)) hold. As for the purely thermal operation case, the linear combination of the governing equations yields a global balance:

$$P_{net} + F_1\,h_{in1} + F_2\,h_{in2} - F_1\,h_{a0} - F_2\,h_{res} - \dot{n}\,\hat{h}_{a0} - \dot{n}\,\Delta H_{298} + \dot{n}\,M_{CO2}\,H_{res} = 0 \qquad \text{(II.6b)}$$

Actually, the calcination reaction would reasonably start inside the riser at some height at which a threshold temperature is reached. As a consequence, a part of the heat transferred from the annulus would be absorbed by the riser to drive the reaction, resulting in a lower T_{rf}. Conversely, part of the energy irradiated into the receiver would be spent to raise the temperature at the fixed

T_{a0}. The assumption that the reaction only takes place in the receiver just implies a segregation of the sensible and reaction heat loads between the heat exchanger and the receiver and should not have consequence on the global energy balance and the power requirements. On the other hand, a lower T_{rf} implies a higher temperature difference and then a shorter heat exchanger. Thus, this assumption is conservative for design purposes.

II.2.3. Discharge operation

The discharge reaction (the carbonation of CaO) is carried out in the reservoir. The total amount of energy that can be released by carbonation is also given by Eq. (II.10). Moreover, a discharge efficiency can be defined as:

$$\eta = (P_{out}\,\tau_r) / E \qquad (II.18)$$

where P_{out} is the output power and τ_r is the time for complete conversion of CaO, still given by Eq. (II.12). Two possible configurations for retrieval of energy are considered, as reported in Fig. II.2. In one configuration (Fig. II.3a) energy is recovered from the outlet gas. In the other configuration (Fig. II.3b) heat is extracted from the reservoir operated as fluidized bed, while the sensible heat of the outlet gas is used to pre-heat the feed gas. The former solution is technically simpler, while the latter one provides one more degree of freedom. Assuming to fix the temperature of the outlet gas after cooling down to T_{out} (for instance 20 °C above temperature T_{in}), the only free variable in the first configuration is the gas flowrate, while in the second one it is possible to vary the amount of heat released from the reactor (P_{out}), which also affects the process temperature.

The product molar rate of the reaction $\dot{n}$ is obtained from a material balance on the inert gas, still considering thermodynamic equilibrium:

$$\dot{n} = F\,(y - y_{eq}) / (1 - y_{eq}) \qquad (II.19)$$

where y is the inlet volume fraction of CO_2. The CO_2 fixed on CaO causes an increase in solid mass, so a mass balance is necessary:

$$dm/dt = \dot{n}\, M_{CO2} \qquad (II.20)$$

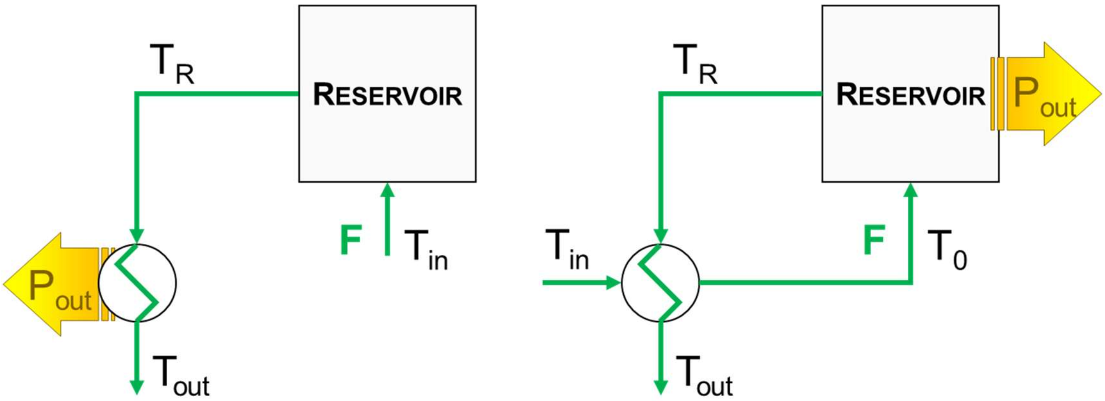

(a) (b)

Figure II.3 Discharge configurations. Energy recovery from gas (a) or fluidized bed (b).

Then two energy balances are written on the reactor and on the downstream heat exchanger. Equations (II.21)–(II.20) hold for scheme in Fig. II.2a, Eqs. (II.23)–(II.24) for scheme in Fig. II.2b.

$$dm/dt\, H_R = F\,[(1-y)\,h_{in} + y\,\hat{h}_{in}] - F\,(1-y)\,h_R - (F\,y - \dot{n})\,\hat{h}_R + \dot{n}\,\Delta H_{298} \qquad (II.21)$$

$$F\,(1-y)\,h_R + (F\,y - \dot{n})\,\hat{h}_R - P_{out} - F\,(1-y)\,h_{out} - (F\,y - \dot{n})\,\hat{h}_{out} = 0 \qquad (II.22)$$

$$dm/dt\, H_R = F\,[(1-y)\,h_0 + y\,\hat{h}_0] - P_{out} - F\,(1-y)\,h_R - (F\,y - \dot{n})\,\hat{h}_R + \dot{n}\,\Delta H_{298} \qquad (II.23)$$

$$F\,(1-y)(h_R - h_{out}) + (F\,y - \dot{n})(\hat{h}_R - \hat{h}_{out}) = F\,[(1-y)(h_0 - h_{in}) + y\,(\hat{h}_0 - \hat{h}_{in})] \qquad (II.24)$$

By summing Eqs. (II.21)–(II.22) and (II.23)–(II.24), the same global balance equation is obtained:

$$dm/dt\, H_R = F[(1-y)\, h_{in} + y\, \hat{h}_{in}] - P_{out} - F(1-y)\, h_{out} - (F\, y - \dot{n})\, \hat{h}_{out} + \dot{n}\Delta H_{298} \quad \text{(II.25)}$$

This means that the two configurations are, in principle, equivalent. Another interesting remark is that, once T_{in}, T_{out} and y are fixed, the reactor temperature T_R is only dependent upon the ratio P_{out}/F, that is the amount of heat released per mole of feed. It follows, by combining Eqs. (II.10), (II.12), (II.18) and (II.21), that also the discharge efficiency is tied to this ratio:

$$\eta = (P_{out} / F)\ (1 - y_{eq}) / (y - y_{eq}) / \Delta H_{298} \quad \text{(II.26)}$$

For a fixed triplets of T_{in}, T_{out} and y, η and T_R can freely vary with the ratio P_{out}/F for the case in Fig. II.2b, whereas for the case in Fig. II.2a T_R is bound by Eq. (II.21) and so are P_{out}/F and η.

The CO_2 feed can derive from an industrial source, like the flue gas from a combustion process. Alternatively, the CO_2 produced by the calcination step can be stored and used as reactant for the discharge step. This option would allow the autonomous operation of the battery, at the expense of increasing plant complexity.

II.2.4. Constitutive parameters

The constitutive parameters appearing in Eqs. (II.7)–(II.8) depend on the geometry of the system and on the properties of the granular phase. In order to perform exploratory calculations, constant values have been assumed in agreement with experimental results: K = 25 kg/m^3, u_{min} = 0.25 m/s (Tregambi et al., 2020b) and U = 400 W/(m^2 K) (Tregambi et al., 2020a). In these experiments Geldart B sand particles were used (size range: 0.1–0.3 mm).

Except for the length L of the heat exchanger, that is a free design variable, geometrical parameters of the prototype have been fixed in the computations: the diameters of the riser, annulus and reservoir cross-sections are 10 mm, 16 mm and 40 mm. The reaction enthalpy ΔH at 25 °C is 178 kJ/mol. A linear relation for ΔG° was used in order to calculate the equilibrium concentration of CO_2 from Eq. (II.13):

$$\Delta G^\circ = \gamma_0 + \gamma_1 T \tag{II.26}$$

with parameters obtained from literature (Shackelford and Alexander, 2006): $\gamma_0 = 128.124$ J/mol, $\gamma_1 = -0.142167$ J/(mol K). A total inventory m of 120 g of limestone is chosen and α_{CaCO3} is set at 30% to account for sorbent sintering over iterated cycling (Tregambi et al., 2019). Accordingly, a maximum storage capacity E of 66 kJ or 18 Wh can be calculated. Data for enthalpy calculations were obtained from literature (Perry, 2008). The solid specific heat was taken as the weighted mean value between that of pure CaO and the one of the initial unreacted solid. The system is at atmospheric pressure.

II.3. Results and discussion

The system of equations for the charge phase has four degrees of freedom. Design calculations can be performed to calculate the length of the heat exchanger (L) and net power P_{net}, by setting the two gas velocities u_1 and u_2, and two temperatures. A couple of independent temperatures can be chosen by setting T_{a0} or T_{rf} and then T_{af}, T_{res} or T_{rf}.

II.3.1. Purely thermal operation

A series of design calculations are performed, starting from a base case and changing one variable at a time, to show the corresponding effect. For the base case calculation, the receiver temperature T_{a0} is set at 900 °C, whereas the reservoir temperature T_{res} is set at 650 °C, in agreement with temperatures required for limestone calcination/carbonation reactions. Primary gas velocity u_1 is set to 1.2 m/s and secondary gas velocity u_2 is set to zero. Table II.1 shows the output for each case: the first row corresponds to base case calculations, the others report results obtained changing one input variable at a time. By reducing u_1, the net power must be reduced because of the reduction of convection losses, according to the global energy balance (Eq. (II.6)), and the length of the heat exchanger must be reduced as well because of the reduction of the solid circulation rate W (Eq. II.8)), according to the heat exchanger balances (Eqs. (II.4), (II.7)). The effect can be appreciated by looking at the temperature profiles in Fig. II.4a.

Input					Results			
u_1 [m/s]	u_2 [m/s]	T_{res} [°C]	T_{a0} [°C]	reaction	W [g/s]	P_{net} [W]	P_{ex} [W]	L [m]
1.2	0	650	900	no	1.9	31	447	2.28
0.8					1.1	21	192	0.63
	0.05				1.9	45	432	1.40
		730			1.9	30	309	1.56
			825		1.9	29	308	1.57
				yes	1.9	844	388	1.07

Table II.1 Results.

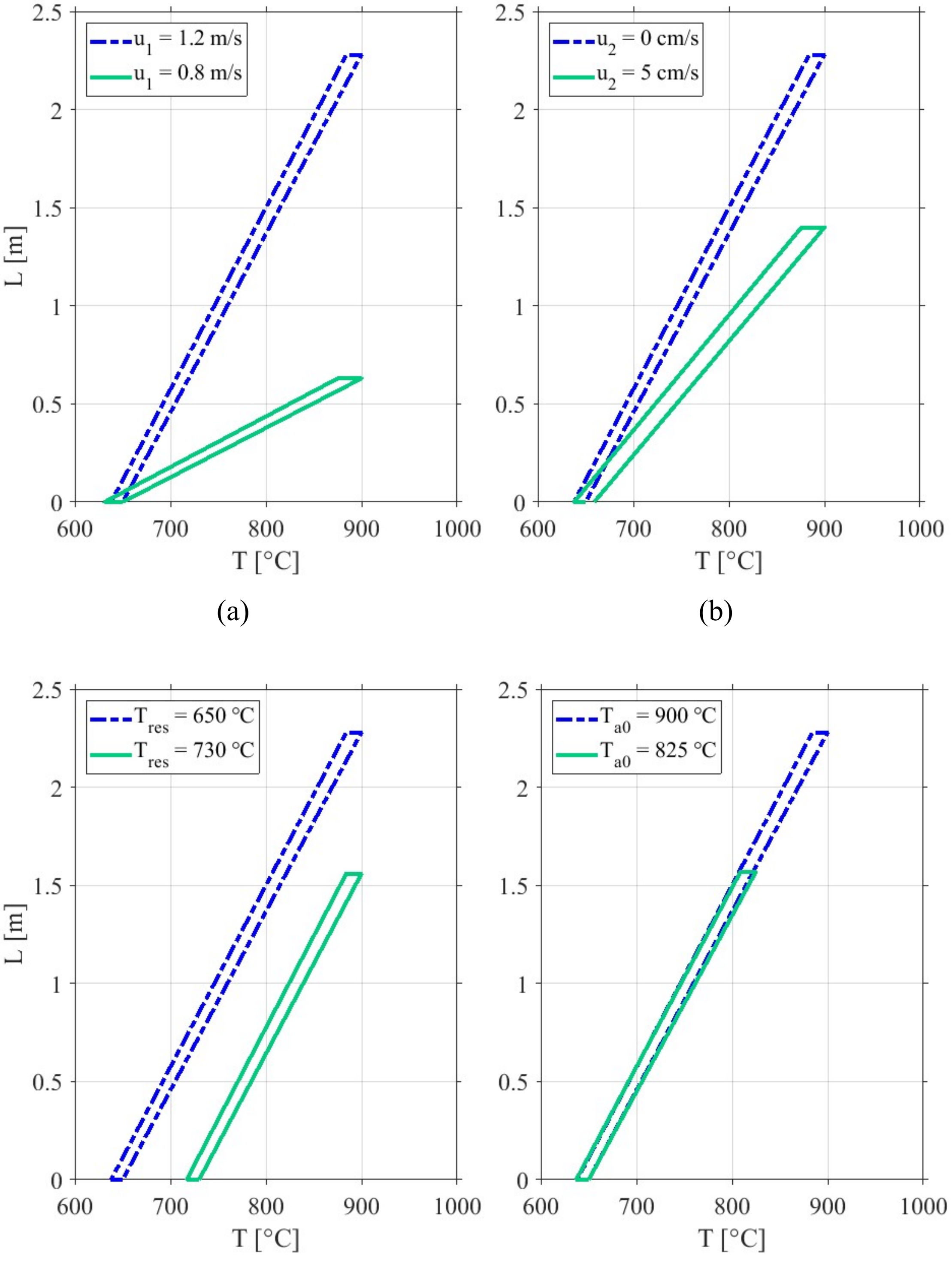

(a) (b)

(c) (d)

Figure II.4. Temperature profiles along the heat exchanger: effect of u_1 (a), u_2 (b), T_{res} (c) and T_{a0} (d).

If a secondary gas stream is fed to the reservoir to keep it under fluidized state, the net power increases because of the increase of convection losses, according to global energy balance (Eq. (II.6)), but the heat exchanger length must be reduced. This is explained by looking at the reservoir energy balance (Eq. II.5): the solid inlet temperature T_{af} must increase with respect to T_{res}, consequently increasing driving force of the heat exchanger (ΔT) in Eq. (II.7). Fig. II.4b shows this effect. By increasing the reservoir temperature T_{res} (Fig. II.4c), the length of the heat exchanger must be shortened according to the heat exchanger balances (Eqs. (II.4), (II.7). The net power remains almost constant, because by increasing T_{res}, the riser inlet temperature T_{r0} also increases following the riser inlet balance (Eq. (II.1)) and the primary gas molar flowrate F_1 is reduced to keep constant u_1, according to the ideal gas equation of state (Eq. (II.9). Finally, by decreasing the receiver temperature T_{a0} both the net power and the length are obviously reduced (Fig. II.4d), as follows from the heat exchanger (Eqs. (II.4), (II.7)) and the global energy balances (Eq. (II.6)). The effect of limestone calcination is considered through Eqs. (II.3b)–(II.6b). The net power sharply increases, due to the power required by the chemical reaction (Eq. (II.6b)). The reduction of the heat exchanger length (Fig. II.5) might be an unintuitive result. Due to the CO_2 released in the receiver, the solid flowrate through the annulus is reduced and less heat is transferred (Eq. (II.4b)). This also causes the slopes of the temperature profiles in the riser and the annulus to diverge, resulting in the increase of the temperature difference ΔT in Eq. (II.7). Both effects reduce the length required for the heat transfer.

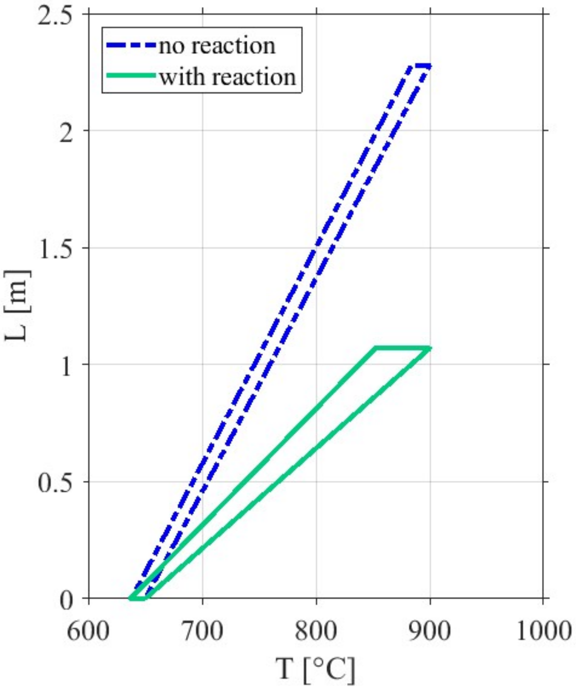

Figure II.5. Effect of limestone calcination in the receiver.

II.3.2. Charge operation

The results of a series of design calculations, performed with the charge operation equations are presented below. All calculations were performed considering the reservoir either fluidized or not, with a constant temperature T_{res} of 650 °C. Gas velocities and flowrates are chosen to vary in the range for which the parameters of Eq. (II.8) were obtained (Tregambi et al., 2020b). In particular, the lowest value of the gas velocity corresponds to the minimum value for which a stable solid circulation occurs (u_{min}). For a fixed primary gas velocity u_1, i.e. a fixed solid circulation rate W (Eq. (II:8)), the time of charge τ_r decreases, by increasing the receiver temperature T_{a0}, until it reaches a minimum plateau value, evidenced by an angular point between 880 °C and 900 °C (Fig. II.6a). This point corresponds to the temperature T* above which the reaction is no more thermodynamically constrained ($\dot{n}_{eq} > \dot{n}_{st}$) and the maximum molar product rate ṅ is reached, dictated by stoichiometry according to Eq. (II.16).

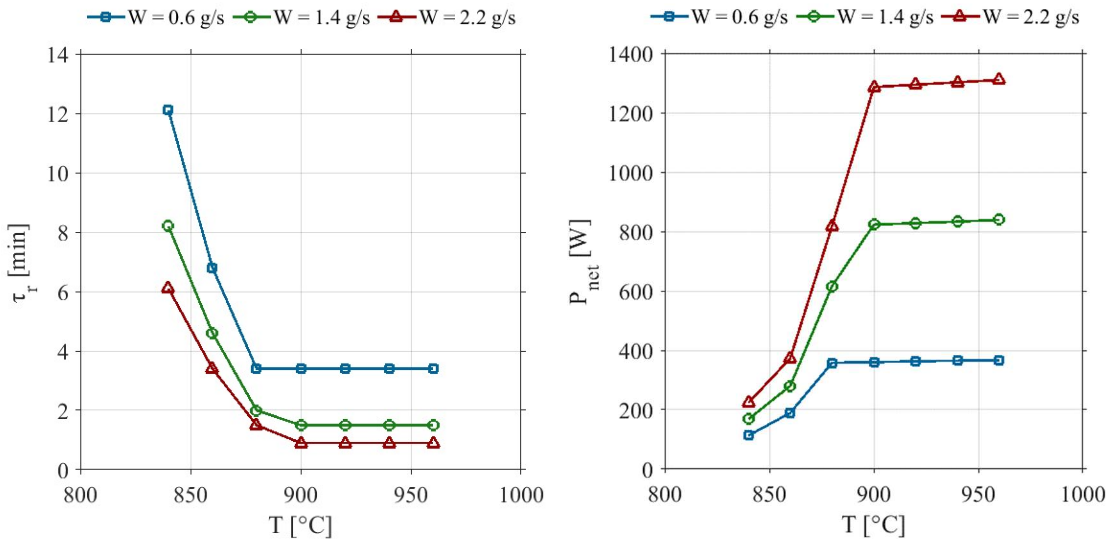

(a)

(b)

Figure II.6. Charge time (a) and net power (b) as a function of the receiver temperature T_{a0}.

By combining Eq. (II.12) and (II.15), it can be seen that the charge time becomes equal to the mean recirculation time:

$$\tau = m / W \tag{II.27}$$

The net power sharply increases with temperature up to T*. Beyond that temperature the conversion rate ṅ reaches its maximum value and P_{net} increases but with a smaller slope, as only additional sensible energy is absorbed (Fig. II.6b). These two trends have opposing effects on the charge efficiency, as it can be understood from Eq. (II.11). Fig. II.7a shows the resulting trend: the effect of the reduction of the charge time, sustaining the increase of the charge efficiency, is prevailing until it becomes constant beyond T*, then the charge efficiency declines as the net power increases. The required annulus length L decreases as the reaction speeds up, because of the reduction of solids flowrate through the annulus, then it increases (Fig. II.7b). The temperature T* is the optimal temperature for the charge operation, as under this operating condition the time of charge τ_r and required annulus length L assume the minimum values while the charge efficiency η reaches the maximum value. T* just depends on the solid circulation rate W, as obtained by equating Eq. (II.15) and (II.16).

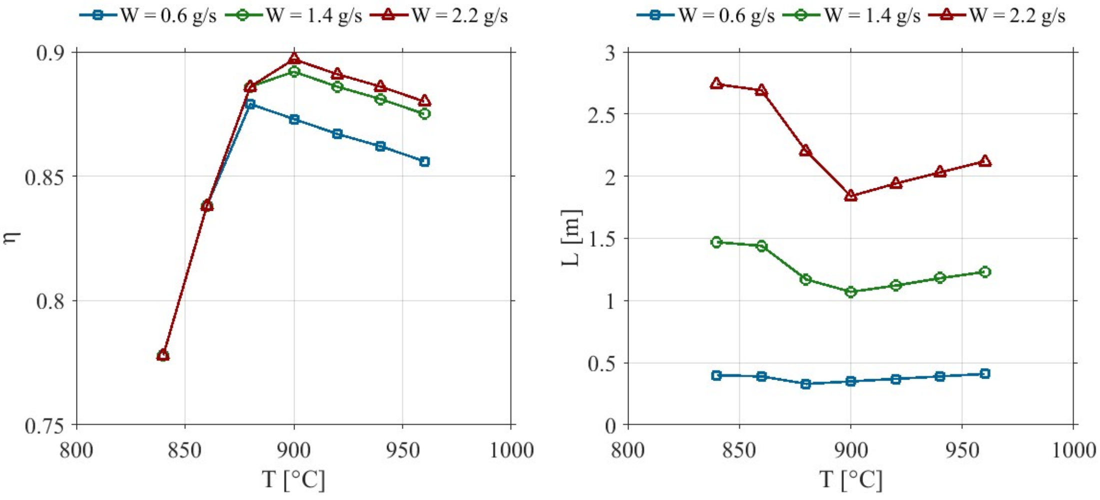

(a) (b)

Figure II.7. Charge efficiency (a) and heat exchange length (b) as a function of the receiver temperature T_{a0}.

The case of the reservoir under fluidized conditions is not shown as it has no effect on the charge time and slightly affects P_{net}, with an efficiency reduction. The non-fluidized reservoir case is the less favorable from the standpoint of heat transfer, so in the fluidized case the annulus length L can be reduced. Finally, Fig. II.8 shows the outlet volume fraction of CO_2 y_{out}. At temperatures lower than T*, it just corresponds to the equilibrium concentration (Eq. (III.13)). The CO_2 outlet concentration is expected to tend to 1 asymptotically as T_{a0} increases, as F_1 is reduced to keep constant u_1.

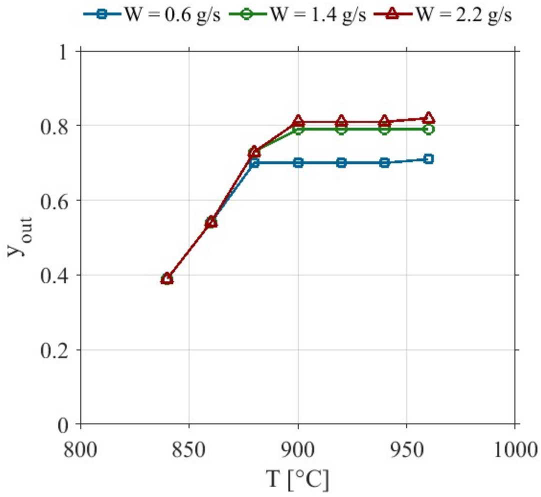

Figure II.8. Outlet CO_2 concentration vs. receiver temperature T_{a0}.

Above T*, a plateau is observed, corresponding to the stoichiometric limit of the product molar rate (Eq. (II.15)). By increasing the circulation rate W, the CO_2 molar fraction y_{out} increases. However, in order to increase the circulation rate, the primary gas flowrate has to be increased as well. The combined effect of these trends is that a limit $y_{out}(T)$-curve is approached for large flowrates. The fate of the CO_2-rich stream issuing from the thermochemical battery is open to alternative solutions. It has already been suggested that storing the gas as reactant for the subsequent discharge phase would make the thermochemical battery independent from external sources, and the estimated concentrations would confirm this possibility.

II.3.3. Discharge operation

Simulations are performed first for the configuration shown in Fig. II.3b, while varying the reactor temperature T_R and the CO_2 inlet concentration. The gas outlet temperature was fixed at 20 °C above the inlet one and the feed flowrate F at 0.1 Nm^3/h, corresponding to a velocity around 9 cm/s at operative temperatures. The results are shown in Fig. II.9.

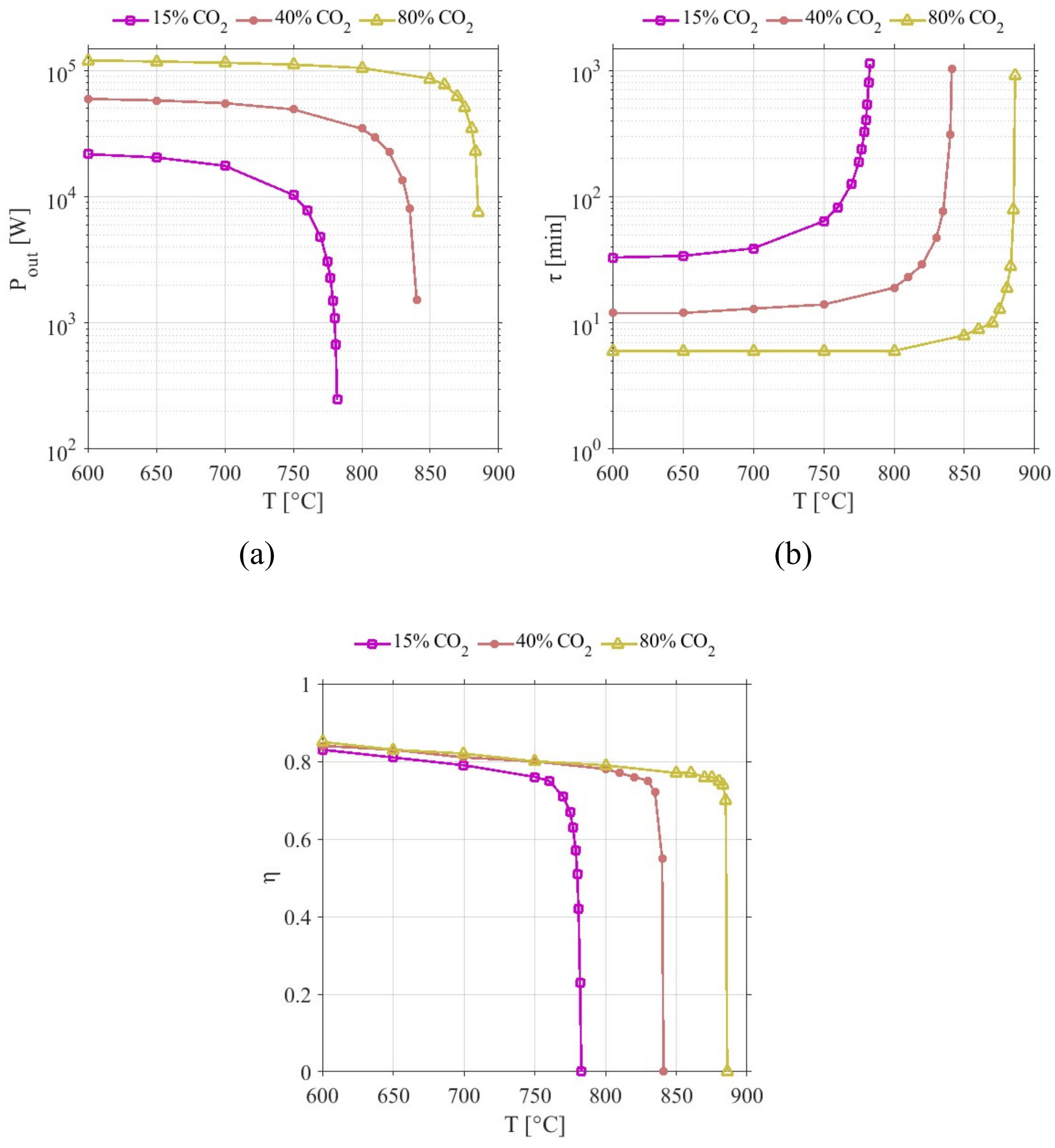

(a) (b)

(c)

Figure II.9. Heat released per mole of feed (a) – Discharge time (b) – Discharge efficiency (c) vs. reactor temperature T_R.

There is an upper limit to the reactor operating temperature T_R for which the equilibrium concentration of CO_2 (Eq. (II.13)) equals the inlet concentration and the product molar rate $\dot{n}$ goes to zero. As T_R approaches this limit value, the heat released per mole of feed P_{out}/F drops to zero (Fig. II.9a). Conversely, at low temperatures the equilibrium concentration of CO_2 tends to zero and the conversion rate $\dot{n}$ reaches its maximum value depending on the CO_2 inlet concentration according to Eq. (II.19). As a consequence, also the heat released per mole of feed reaches an upper limit. The discharge time τ_r is inversely proportional to the product molar rate $\dot{n}$, so it reaches a minimum at low temperatures and diverges by approaching the maximum operative temperature of the reactor (Fig. II.9b). Discharge efficiency η depends on the product of the heat released from the reactor and the discharge time, that have opposite trends. It generally follows the trend of released heat, going to zero for the maximum operating temperature. But it is noteworthy that at low temperatures the discharge efficiency seems to follow a linear trend that looks almost independent of the CO_2 inlet concentration (Fig. II.9c). This trend is not remarkably influenced by the efficiency of the heat recovery, as it may be inferred from a global balance. This trend can be mathematically derived from Eqs. (II.19), (II.18), (II.25) and (II.26) and by substituting $y_{eq} = 0$ and $T_{out} = T_{in}$, so assuming a maximum heat recovery:

$$\eta_{max} = 1 - (M_{CO2}\, H_R - \hat{h}_{in}) / \Delta H_{298} \qquad \text{(II.28)}$$

As it appears, the enthalpy of the CO_2 that is fixed on CaO cannot be recovered and deeply influences this trend and represents the major energy loss. Therefore, from Equation (II.28) it is possible to obtain the upper limit value of the discharge efficiency for a given reactor temperature T_R and inlet concentration of CO_2. However, these calculations neglect the effect of the decline of the kinetic rate at lower temperatures, that would result at in a decrease of the efficiency. As consequence, an optimum temperature should be found at some point below the adiabatic temperature.

When the discharge configuration reported in Fig. II.3a is considered, results are pretty much the same, but for a given CO_2 inlet concentration the temperature is fixed, and so any other parameter. For the three chosen values of the inlet concentration $y = 0.15$, 0.4 and 0.8, the adiabatic temperature T_{ad} is

696 ◦C, 819 ◦C and 881 ◦C, while the efficiency η takes the values 0.8, 0.76 and 0.75, respectively.

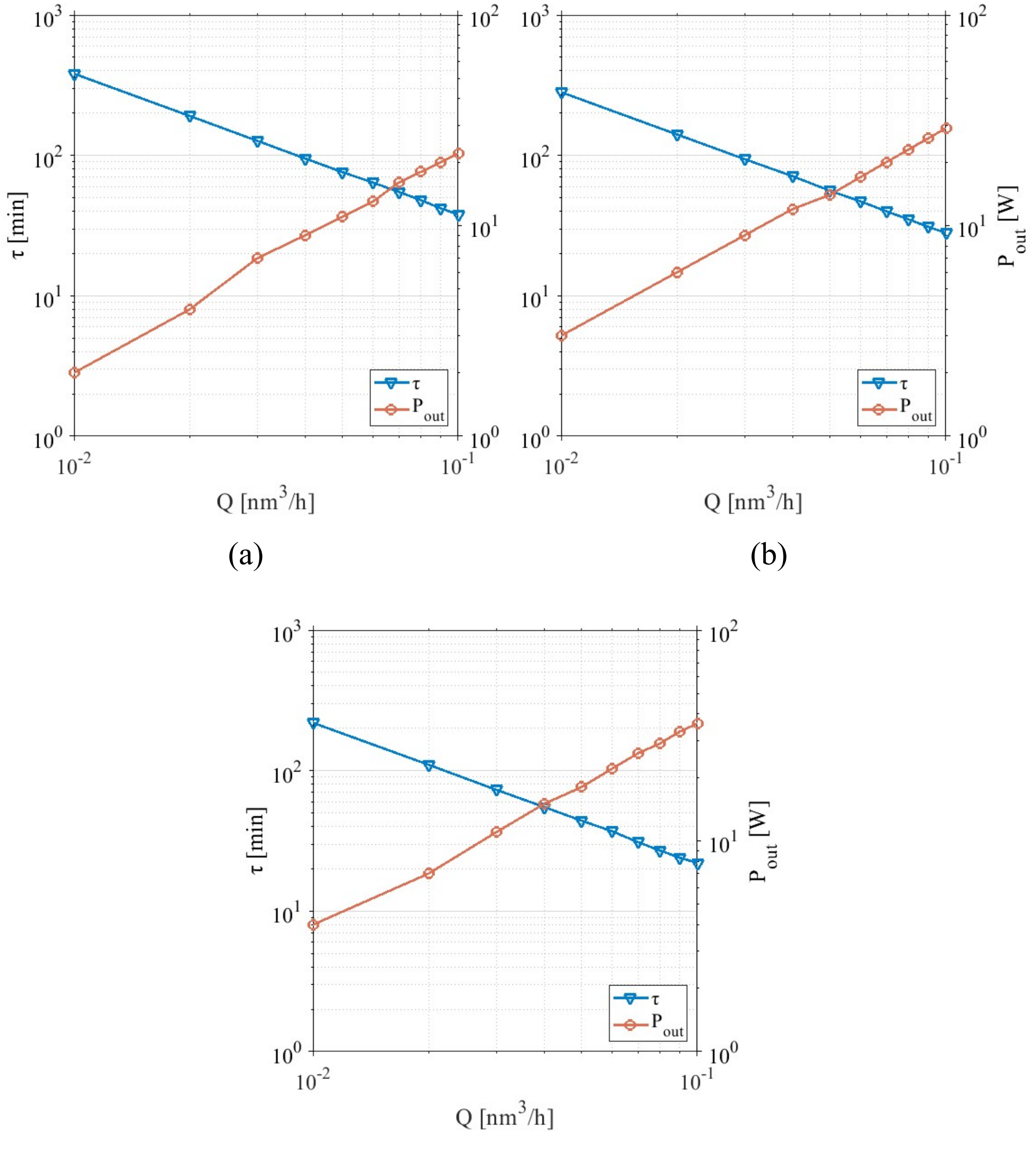

(a) (b)

(c)

Figure II.10. Discharge time and power as a function of the gas flowrate at the adiabatic temperature; 15% CO_2 - 696 °C (a); 40% CO_2 - 819 °C (b); 80% CO_2 - 881 °C (c).

Once the inlet concentration y and reactor temperature T_R are fixed, the efficiency η is fixed as well. Then by varying the feed flowrate F, the discharge time τ_r and power P_{out} vary in opposite ways. They are inversely proportional, since their product equals the storage capacity E times the discharge efficiency η, as in Eq. (II.18). This is shown in Fig. II.10, while varying the feed flowrate between 0.01 and 0.10 Nm^3/h, corresponding to velocities between 1 and 10 cm/s. This is an interesting result, as it suggests that the discharge time and power can be freely controlled without affecting the efficiency and the reservoir temperature.

CHAPTER III

MULTIPHASE REACTORS FOR THERMOCHEMICAL PROCESSES

This chapter deals with the study of Chemical Looping Reforming of CH_4 (§I.2.2). The oxygen carrier used is a laboratory-prepared perovskite with chemical formula $La_{0.6}Sr_{0.4}FeO_3$. Experimental campaigns have been carried out in fixed bed and fluidized bed conditions to investigate reaction stoichiometry, kinetics and selectivity at different temperatures as well as the material stability over iterated looping cycles. A critical comparison between fixed and fluidized bed performance has been made. Preliminary experimental tests have been conducted with the DIFBAR receiver test unit, previously employed for Calcium Looping (Tregambi et al., 2020b), in view of the application with the new scaled-up prototype.

The perovskite powder was synthetized following the procedure developed by Luciani et al. (Luciani et al., 2018). Briefly, stoichiometric amounts of strontium nitrate, lanthanum nitrate hydrate and iron (III) nitrate nonahydrate (Sigma Aldrich) were dissolved in 75 mL bi-distilled water and stirred for 3 h. The obtained solution was heated for few minutes (about 10 min) in a microwave oven (CEM SAM-155) up to the formation of a homogeneous gel, which was further calcined at 1100 °C for 4 h (heating rate: 10 °C/min). The powder was pressed into small cylindrical pads (2-3 mm diameter and height) with a bench-top press at 10 ton. Eventually, the pads were crushed into a mortar, and the fragments sieved in the size range 200-400 μm. Larger particles were crushed again, while finer pressed again into pads, until granulation of the whole powder sample within the desired size range.

III.1. Fixed and fluidized bed experimental set-ups

III.1.1. Experiments under fixed bed conditions

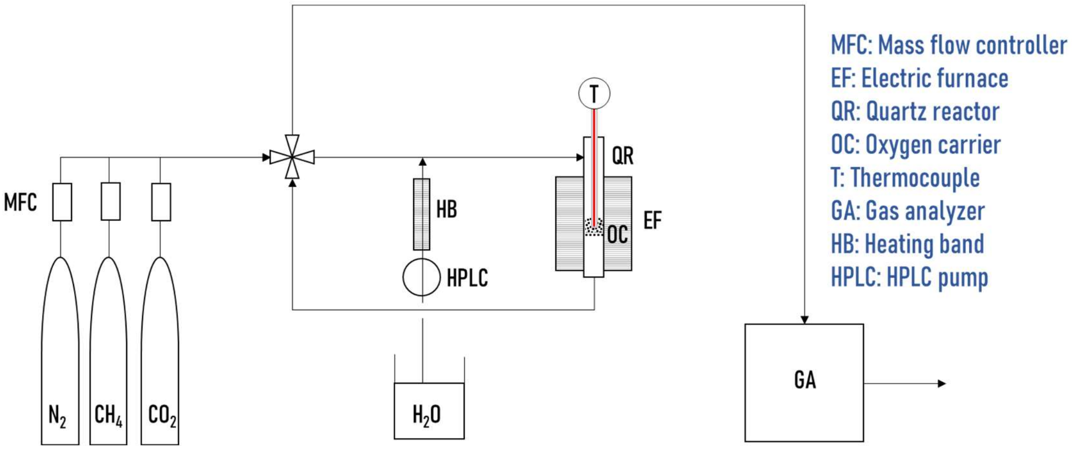

Figure III.1 Experimental set-up for fixed bed reaction tests.

Figure III.1 shows the set-up for the experiments under fixed bed conditions. A perovskite sample (0.5 g) was placed on a porous plate inside a tubular quartz reactor with an internal diameter of 10 mm and heated by a cylindrical electric furnace (Lenton). A thermocouple, sheathed with a 6 mm tube, was vertically plunged into the sample along the center line of the reactor. A PID-type controller was used to set a heating rate or a fixed temperature. The reactants were diluted in a nitrogen (N_2) flow and fed at the top of the reactor. The gaseous species were fed from pure gas cylinders through mass flow controllers (Brooks 5850S). Water was fed with a pump (Dionex P680 HPLC Pump) and vaporized by heating at 120 °C. A pressure transducer monitored the pressure upstream the reactor inlet for safety reasons. The outlet gaseous stream was analyzed with two gas analyzers in series (Gas 3100 Syngas Analyzer and NGA 2000 from Rosemount) to detect the main chemical species (CH_4, CO, CO_2, H_2, O_2), after drying in a $CaCl_2$ trap. The reactor can be by-passed using a four-way valve, to allow the analysis of the feed.

The following experiments were run:

- Temperature Programmed Reduction (TPR) from 25 to 1000 °C at 10 °C/min with CH_4.
- Temperature Programmed Oxidation (TPO) from 550 to 1000 °C at 10 °C/min with CO_2.
- Isothermal cycles with CO_2 as oxidizer at 860, 920 and 1000 °C.
- Isothermal cycles with H_2O as oxidizer at 920 °C.

For every test the gas was fed from the top with a total flowrate of 10 NL/h, corresponding to a gas velocity between 0.14-0.17 m/s for the operating temperature range (860-1000 °C). The gas composition was 5% CH_4 for the reduction steps and 5% CO_2 for the oxidation steps. The concentration of H_2O could not be measured, but the pump was set to supply the oxidizer at the same concentration. A pure N_2 flow was used to sweep the reactor between consecutive reaction steps. After the TPO with CO_2, a TPO was performed with O_2 to ensure the full re-oxidation of the catalyst and to eventually burn unconverted coke deposited on the perovskite surface.

III.1.2 Experiments under fluidized bed conditions

The set-up for the experiments under fluidized bed conditions was very similar (Figure III.2). The perovskite sample (3.2 g), sieved in the range 250-355 μm, was placed in a tubular quartz reactor with an internal diameter of 10 mm inside a cylindrical electric furnace (Watlow). The temperature of the catalyst was controlled with a PID controller. The fluidizing and reacting gases were fed from gas cylinders through mass flow controllers (Bronkhorst El-Flow Select). The outlet gas passed through a bubble flowmeter, a water condenser and finally through a gas analyzer (ABB, Advance Optima AO2020).

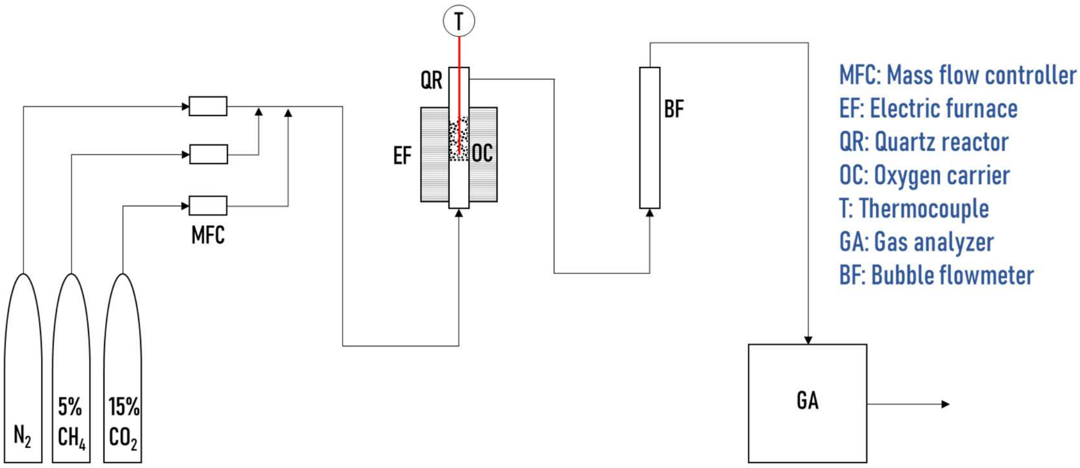

Figure III.2. Experimental set-up for fluidized bed reaction tests.

Isothermal cycles were conducted at 900 °C using CO_2 as oxidizer. A single long reduction step at 970 °C was conducted to study the decomposition of CH_4, followed by an oxidation step at 855 °C. The gas was fed from the bottom with a total flowrate of 70 NL/h, in order to have about the same contact time of the fixed bed experiments. The corresponding fluidization velocity was about 1.1 m/s at 900 °C. The gas composition was 5% CH_4 for all the reduction steps, 15% CO_2 for the oxidation steps at 900 °C and 8% CO_2 for the oxidation step at 855 °C.

III.2. Directly irradiated fluidized bed experimental set-up

III.2.1 The reactor

The experimental apparatus, outlined in Fig. III.3, is the same used in previous studies (Tregambi et al., 2020b) with some modifications. It consists of a directly irradiated fluidized bed reactor, reproducing the features of the DIFBAR receiver. A photo of the reactor is shown in Figure III.4, it is composed of three parts aligned along a same vertical axis:

i) the riser tube, internal diameter (ID) 10 mm, length 120 mm;
ii) the annulus tube, ID 16 mm, length 70 mm;

iii) the receiver, upper ID 120 mm, length 120 mm, lower internal cone angle 30°;

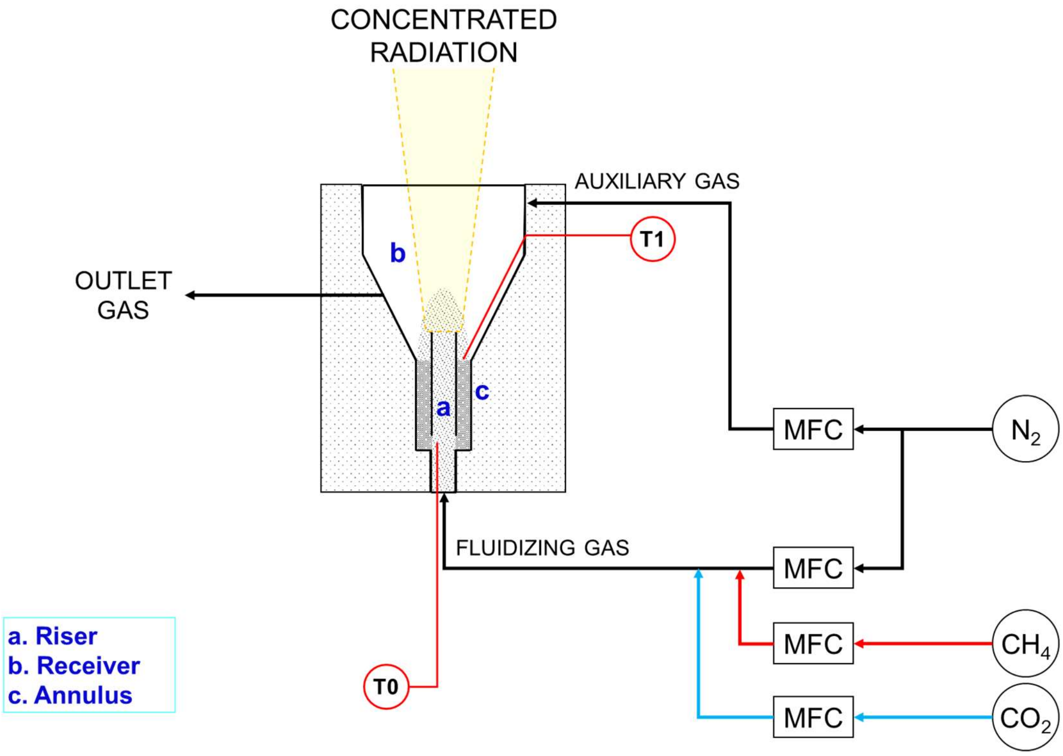

Figure III.3 Experimental set-up for the DIFBAR receiver test unit.

Figure III.4 Photo of the DIFBAR receiver test unit.

The reactor is thermally insulated with multiple layers of rock wool blanket to minimize heat losses toward the external environment. All the parts are made of stainless steel (AISI 310 and AISI 316).

The annulus is welded at the conical bottom of the receiver and is connected to the riser by a reducer fitting. The solid is directly recycled from the annulus to the riser through four symmetrical orifices (6 mm). The riser protrudes inside the receiver for 10 mm. The top of the receiver is closed by a transparent quartz window (3 mm thick, transmittance of 90% in the 250–2500 μm wavelength range), to let in solar radiation, concentrated at the top of the riser. A water-cooled flange is used to close the receiver, using a soft gasket. Several lateral tubes can be used for the gas exit and as accesses for measuring and control devices.

The reactor is operated with a bed inventory of 10-14 g of sand-like particles. A fluidizing gas stream is fed to the riser, through a nozzle (ID 4 mm). Figure III.5 shows the solid circulation rate and mass flux across the riser as a function of the gas velocity obtained from cold flow experiments .

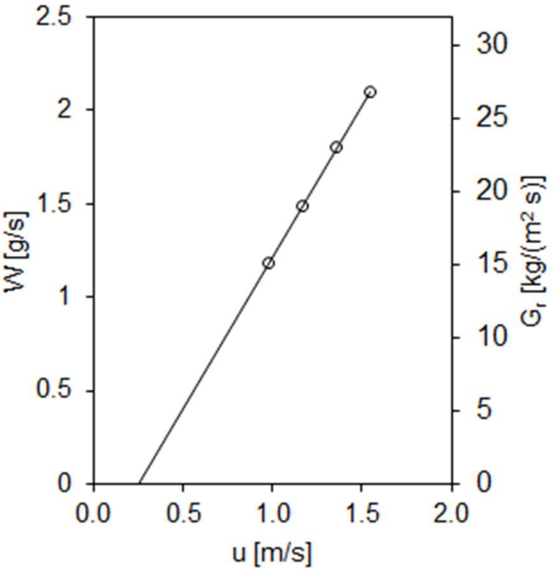

Figure III.5 Solid circulation rates obtained with cold flow experiments.

A minimum gas velocity is necessary to induce the solid circulation between the riser and annulus. The height reached by the particles ejected inside the receiver increases with the gas velocity, so the operative range is limited to prevent the particles to impact the window. Fluidization regime changes, increasing the gas velocity into the riser, from bubbling/slugging to fast fluidization conditions. The transition can be visually observed under circulating conditions, as at low velocities the particles are ejected into the receiver with intermittent slugs, whereas at higher velocities a stable flux of particles appears, whose trajectories resemble the streamlines of a fountain (fountain-like conditions).

An auxiliary stream (50-60 NL/h) can be fed to receiver through a lateral tube of the receiver at a heigh of 90 mm, for the protection of the quartz window.

III.2.2 Measurement and control instrumentations

The fluidizing and reacting gases are fed from gas cylinders through mass flow controllers (Bronkhorst El-Flow Select). The auxiliary gas stream is regulated with a needle valve and a rotameter. A piston check valve from VYC Industrial was installed on a lateral tube of the receiver, with an opening pressure of 80 mbar, to protect the window from overpressures. Bed temperature is measured with two K-type thermocouples: one is located inside the riser at the same height of the orifices (T0) and one is located in the receiver at the inlet of the annulus (T1). Temperature acquisition is performed by means of a NI-9211 module. A LabView VI is used to set the flow controllers, monitor and record reactor temperatures.

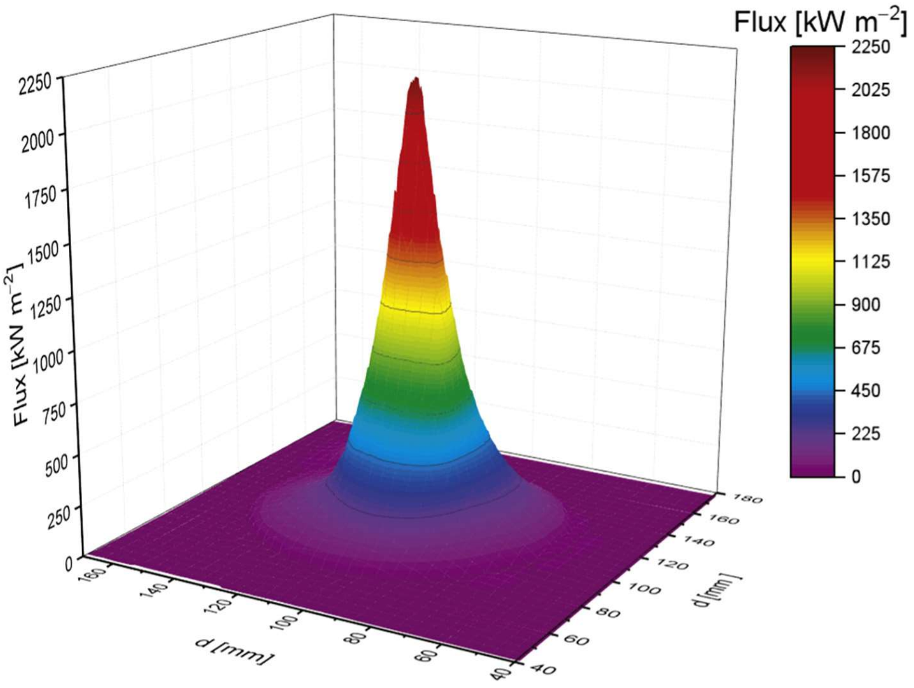

Figure III.6 Spatial distribution of the incident radiative flux from the solar simulator at full power.

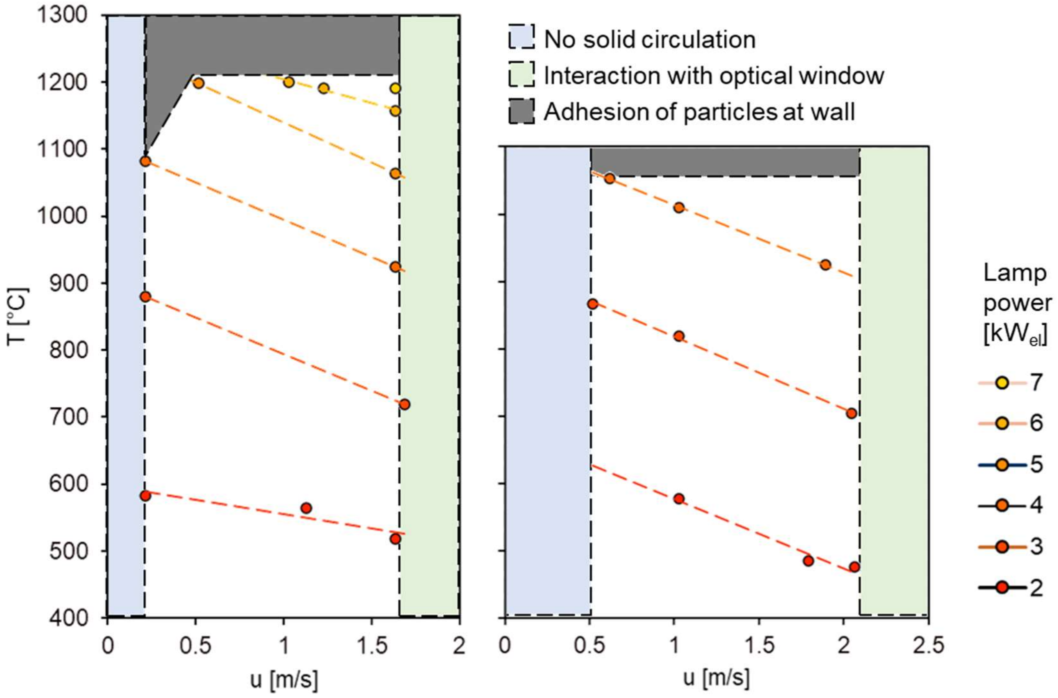

Figure III.7 Operability map of the reactor using mullite (left) and silica sand (right) as bed material.

The solar simulator consists of a short-arc Xe lamp coupled with an elliptical reflector. Lamp input power can be tuned from 2 to 7 kW_e, with 1 kW_e increments. The spatial distribution of the simulated solar radiation at the full power of 7 kW_e, obtained in a previous study (Tregambi et al., 2020b), is reported in Figure III.6.

A peak flux of 2.1 MW/m^2 is obtained in the focal point, while the total thermal power is of about 1.8 kW_{th}. In the same study, operability maps were obtained for different materials by measuring the steady state temperatures for all lamp power steps and the maximum and minimum operative fluidizing gas velocity (Figure III.7). As expected, the steady state temperatures increase with the power of the solar simulator and decrease with the fluidizing gas velocity. Operative gas velocities are bound between two limits: the lower limit is the minimum circulation velocity, and the higher limit is the velocity beyond which the particles ejected in the receiver hit the optical window, because of the higher kinetic energy. Operative temperatures are limited by the adhesion and agglomeration of particles on the receiver wall, that occurs for high powers and low velocities. Mullite was the best material among those tested, as it showed the largest operative temperature range (up to 1175°C).

III.2.3 Experimental procedure

Perovskite from the same sample used for the fluidized bed experiments was mixed with mullite particles (bulk density 1555 kg/m^3, Sauter diameter 210 μm) to reach the operative bed mass. A series of CLR cycles were performed under direct irradiation. The power of the solar simulator was set to 4 kW_{el} to heat the reactor at about 900°C. N_2 was used as the fluidizing and auxiliary gas. The reacting gases (CH_4 and CO_2) were mixed with the fluidizing gas upstream the reactor. The auxiliary stream was fixed at 50-60 NL/h. The outlet gas was split to measure the concentrations of reacting species with a gas analyzer (ABB, Advance Optima AO2020).

III.3. Results and discussion

III.3.1 Fixed bed

Figure III.8 shows the temperature and concentration profiles from the TPR experiments. At about 800°C the reaction starts to take place with a high selectivity toward the products of partial oxidation and with a limited conversion of CH_4, as inferred from the H_2 : CO concentration ratio of about 2. These observations suggest that the reaction is kinetically controlled by oxygen diffusion through the lattice of the perovskite and as consequence the concentration of oxygen on the surface of the catalyst is very low. A very little amount of CO_2 appears to be produced according to the reaction:

$$MO_x + \delta/4\ CH_4 \rightarrow MO_{x-\delta} + \delta/2\ H_2O + \delta/4\ CO_2 \qquad \text{(III.1)}$$

When the temperature exceeds 900°C, the concentration of CO decreases but both the conversion of CH_4 and the production of H_2 continue. It is deduced that, as the catalyst is progressively reduced, CH_4 decomposition takes over (Eq. (I.9)), as confirmed by the ratio between the concentration of H_2 and that of consumed CH_4. The amount produced or reacted of each gaseous species can be calculated as follows:

$$n_i = F_{tot} \int |y_i^{in} - y_i^{out}|\ dt \qquad \text{(III.2)}$$

where F_{tot} is the total molar flowrate, y_i^{in} and y_i^{out} are the inlet and outlet concentration of species i. From the atomic balances on hydrogen, carbon and oxygen it is possible to calculate the amount produced of H_2O and C and the amount of oxygen released by the perovskite:

$$4\ n_{CH4} = 2\ n_{H2} + 2\ n_{H2O} \qquad \text{(III.3)}$$

$$n_{CH4} = n_C + n_{CO} + n_{CO2} \qquad (III.4)$$

$$n_O = n_{CO} + 2\, n_{CO2} + n_{H2O} \qquad (III.5)$$

By dividing n_O by the moles of the sample ($n_{perovskite}$) it is observed that 1.5 moles of oxygen were released per mole of perovskite, corresponding to the total reduction of iron from Fe^{+3} to Fe^0 and thus to the complete conversion of the oxygen carrier. The formation of Fe^0 may be responsible for the catalytic decomposition of CH_4.

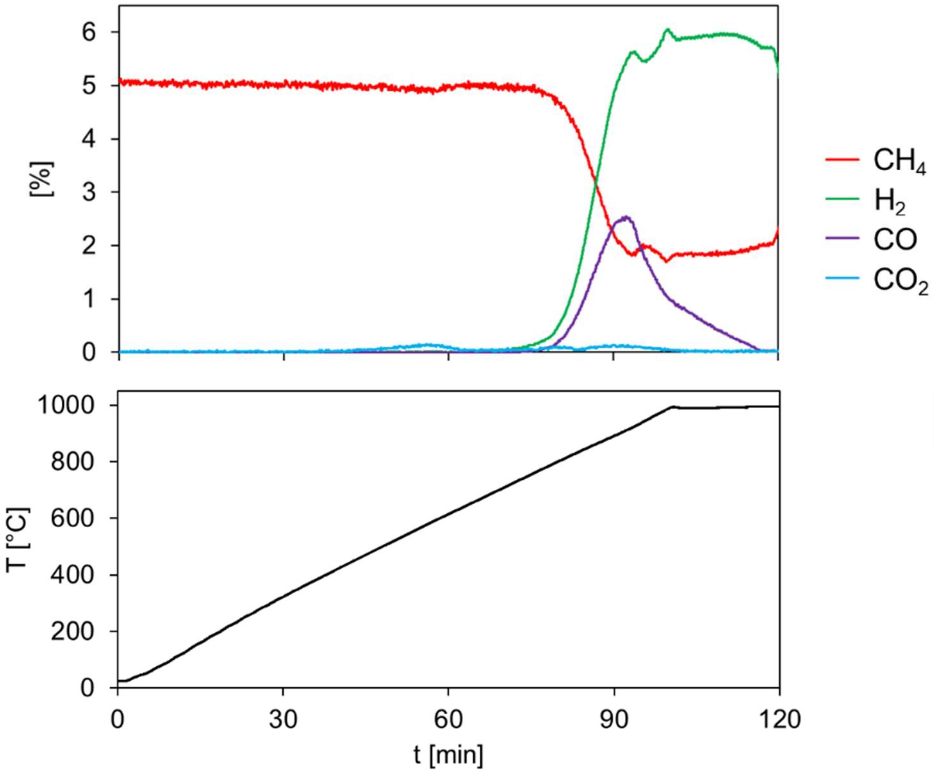

Figure III.8 Temperature Programmed Reduction with 5% CH_4 in fixed bed conditions.

Figure III.9 shows the temperature and concentration profiles during the TPO experiments. The reaction starts just above the initial temperature of 550 °C, and above 800 °C the conversion of CO_2 is almost complete and then falls down, as the catalyst is totally regenerated. The molar ratio between produced CO and converted CO_2 reaches values greater than unity, showing that gasification of deposited carbon according to the Boudouard reaction occurs simultaneously to perovskite oxidation, according to the reaction:

$$CO_2 + C \rightarrow 2\ CO \qquad \text{(III.6)}$$

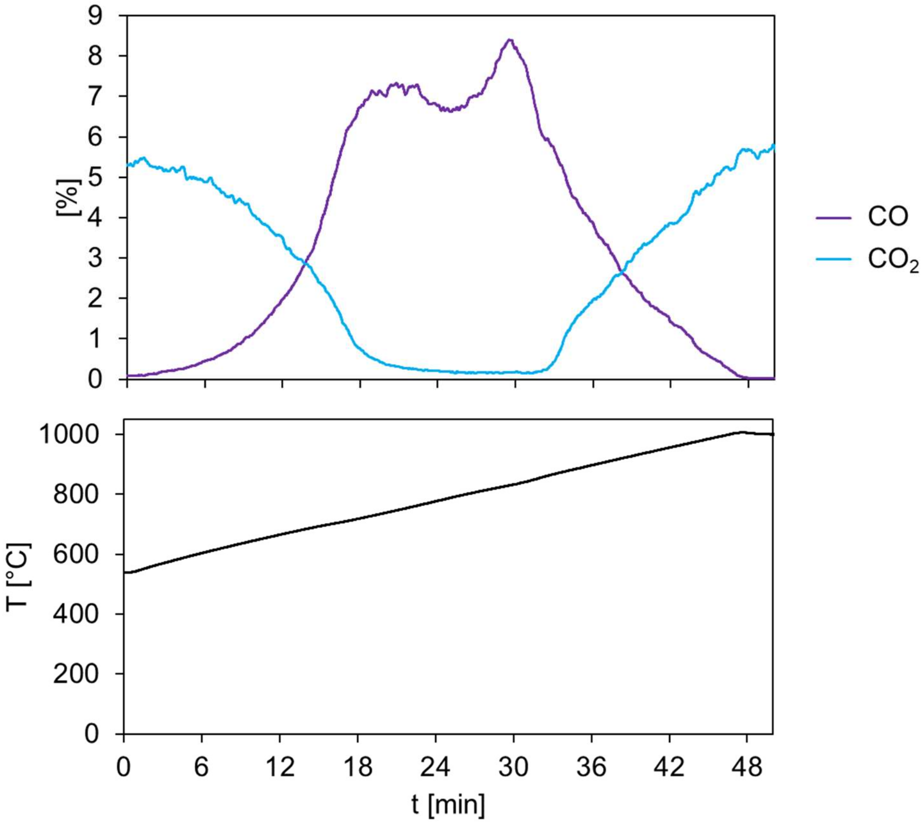

Figure III.9 Temperature Programmed Oxidation with 5% CO_2 in fixed bed conditions.

The amounts involved in the reaction of the gaseous species can be calculated again from Equation (III.2). The atomic balances on carbon and oxygen give the amount of C re-gasified according to reaction (III.6) and the amount of oxygen uptaken by the perovskite:

$$n_C + n_{CO2} = n_{CO}, \tag{III.7}$$

$$2\, n_{CO2} = n_O + n_{CO}, \tag{III.8}$$

The calculations prove that the deposited carbon (C) is totally re-gasified according to reaction (III.6) and that the perovskite is completely re-oxidized. According to these results, a yield of 0.6 Nm^3 of syngas per kg of catalyst per cycle can be obtained from reactions (I.6)-(I.8), corresponding to the maximum value of $\delta = 1.5$, in agreement with literature data for a similar perovskite (Donat et al., 2020)

Isothermal reaction profiles at different temperatures during the reduction steps are shown in Figure III.9. During the course of the reaction, the selectivity toward CO decreases and the H_2 : CO ratio increases, indicating that CH_4 decomposition also occurs. The reduction steps were interrupted in order to limit the decomposition of CH_4 and the deposition of C on the catalyst. To this end, the concentration of CH_4, H_2 and CO were monitored and the feed of CH_4 was interrupted as soon as the selectivity toward CO appeared to drop below 80%. Except for an initial peak of CO_2, the favored products are H_2 and CO in every case and a quasi-steady condition is reached at 860°C. These observations fit very well the interpretation of a fast reaction regime, kinetically controlled by the diffusion of oxygen through the lattice sites: at the beginning of the reaction, CH_4 reacts with the oxygen-rich surface of the catalyst through complete oxidation; due to the low diffusion rate, the oxygen concentration at the surface rapidly drops down approaching the minimum value allowed by the thermodynamic equilibrium. This is evident at 860 °C, as the gas composition probably mirrors an equilibrium condition. At higher temperatures, the reaction speeds up thanks to higher diffusivities and more favorable thermodynamic conditions, as witnessed by the concentration profiles. However, the reaction also slows down more rapidly, due to the faster reduction of the catalyst.

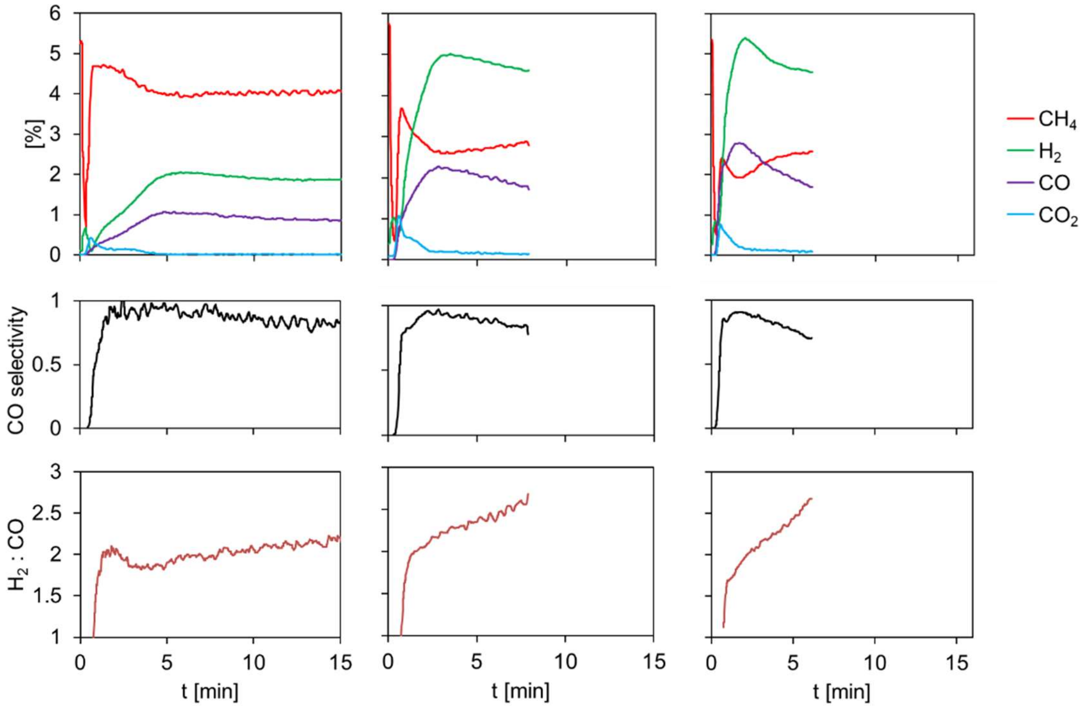

(a) (b) (c)

Figure III.10 Reduction steps under fixed bed conditions at 860°C (a), 920°C (b), 1000°C (c) with 5% CH_4.

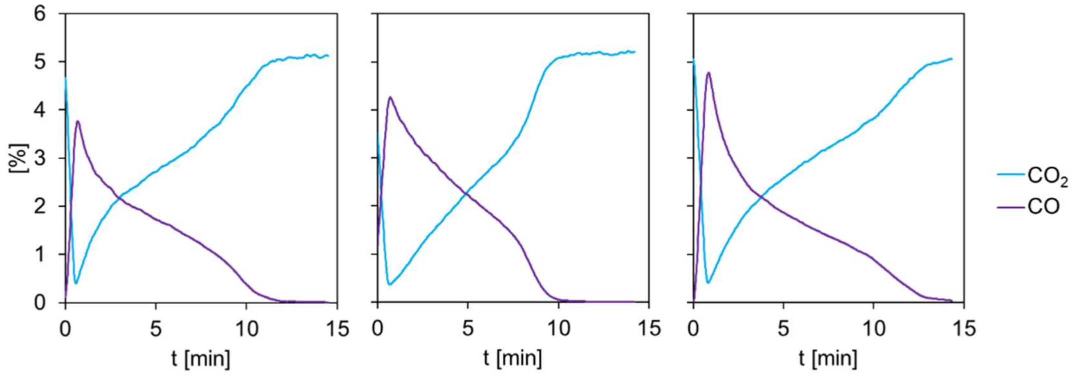

(a) (b) (c)

Figure III.11 Oxidation steps under fixed bed conditions at 860 °C (a), 920 °C (b), 1000 °C (c) with 5% CO_2.

In Figure III.10 the isothermal oxidation steps are shown. The increase of the temperature has opposite effects on the reaction rate. The initial peak of CO concentration indicates an increase of the kinetic rates of surface reactions. However, the reaction times do not increase monotonically. This can again be explained considering oxygen diffusion as the limiting step. At the beginning, the surface of the reaction is rapidly oxidized, producing the peak of CO, but it quickly saturates reaching the highest oxygen concentration allowed by thermodynamic equilibrium. Then the reaction proceeds slowly, controlled by oxygen diffusion from the surface toward the bulk of the catalyst. As temperature is increased, the diffusivity also increases, and this can explain the reduction of the reaction time from 860 °C to 920 °C. However, at higher temperatures, unfavorable thermodynamic equilibrium limits the surface concentration of oxygen and thus slows the diffusion process. This might explain why the reaction time increases, by raising the temperature from 920 °C to 1000 °C.

Equations (7-10) and (12-13) were solved for each of the isothermal cycles and the conversion degrees of the sample were calculated as:

$$X = n_O / (1.5\ n_{perovskite}) \qquad (III.9)$$

Figure III.12 shows the results. A reduction degree around 50% and complete re-oxidation is observed for every process temperature. The cycles show good repeatability, and no deactivation trend is observed. The results of the isothermal cycles at 920 °C using H_2O as oxidizer are shown in Figure III.13. Six consecutive cycles were performed, using a shorter reaction time for the reduction step (6 min) to further limit CH_4 cracking. A reduction degree of about 40% was obtained. As for the CO_2 oxidation tests, the perovskite material showed complete re-oxidation and good cyclability.

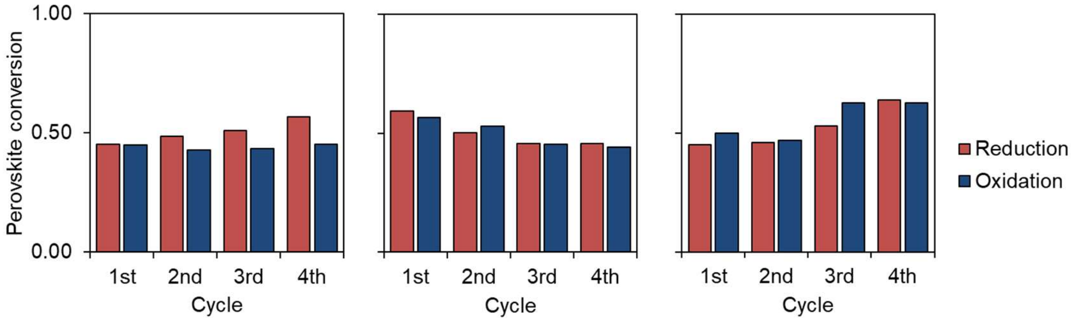

(a) (b) (c)

Figure III.12 Conversion degree during reduction/oxidation isothermal cycles at (a) 860 °C, (b) 920 °C, (c) 1000 °C with CO_2 as oxidizer.

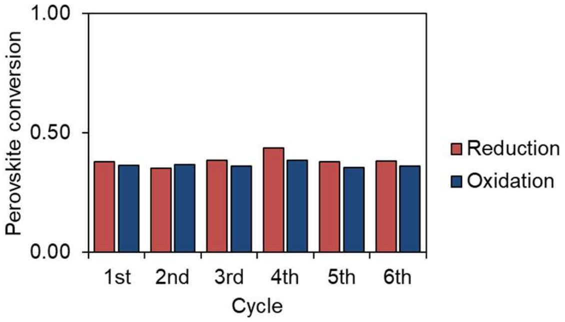

Figure III.13 Conversion degree during reduction/oxidation isothermal cycles at 920°C with H_2O as oxidizer.

III.3.2. Fluidized bed

Four isothermal cycles were conducted at 900 °C. During the first cycle CH_4 was fed for 19 min, to assess the time needed for the total reduction of the perovskite. For the following two cycles, the CH_4 feed was interrupted after 7 min to avoid CH_4 cracking and C deposition. Finally, the fourth cycle was carried on for 16 min, to reach again the full conversion of the perovskite. Figure III.14 shows the reaction profiles of the 2nd and 4th cycles. The reduction profiles (Fig. III.14a) show a good repeatability. Total conversion of the perovskite is achieved in about 12 min and CH_4 decomposition initiates immediately after.

The oxidation profiles (Fig. III.14b) differ because during the 4th cycle C gasification occurs according to the Boudouard reaction, evidenced by the peak of CO. During the 2nd cycle instead, no C is formed and occurring in the 4th cycle. Figure III.15 shows the perovskite conversion degrees. The reduction degree for 7 min at 900 °C is about 72%, whereas in fixed bed experiments at 920 °C the reduction degree for about the same time was 50% suggesting that, in fluidized bed conditions, higher conversion rates can be obtained.

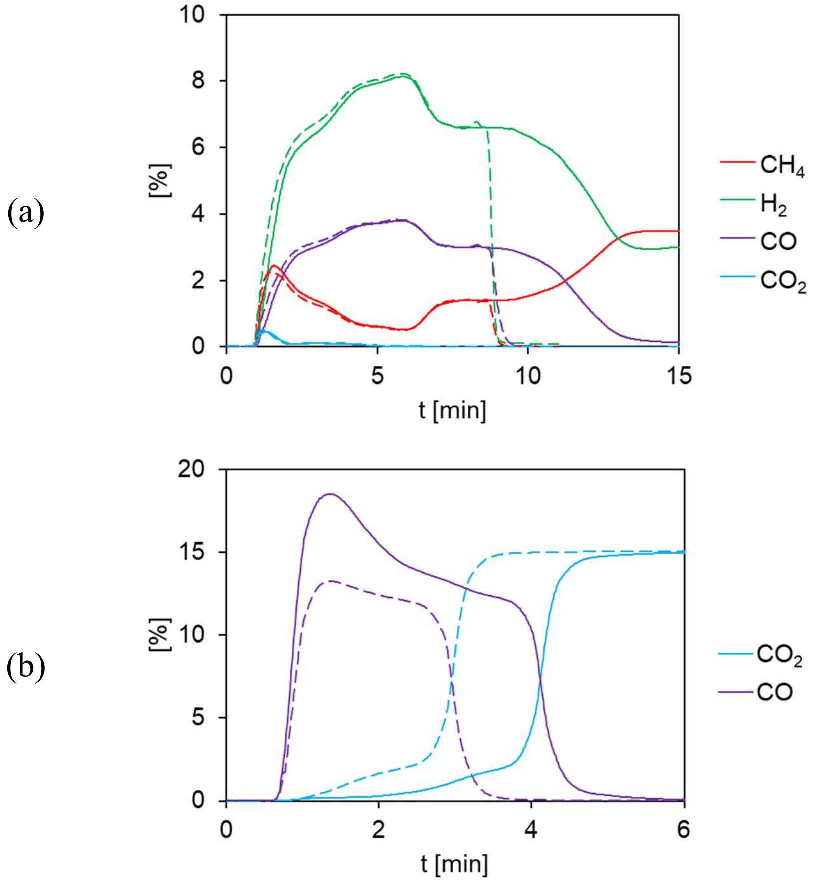

Figure III.14 Isothermal cycles at 900°C: reduction step (a), oxidation step (b). 2nd cycle (dashed line), 4th cycle (continuous line).

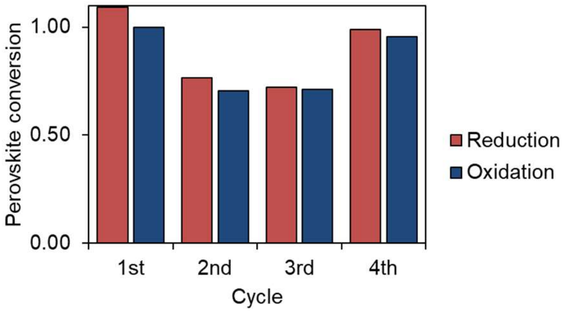

Figure III.15 Isothermal cycles at 900°C.

Finally, results of the long reduction test at 970°C are shown in Figure III.16. This test allowed to investigate the occurrence of deactivation phenomenon due to C deposition on the catalyst. Complete reduction of the perovskite is achieved in about 9 min. It can be pointed out that CH_4 is almost fully converted in this phase, showing again that the conversion rate is higher with respect to the case of the fixed bed (see Fig. III.12c). Then, CH_4 decomposition started and was carried on for more than 35 min. The decomposition rate shows a gradual but constant decrease, indicating an inhibiting effect of the deposited carbon. About 3 mmol of C were produced per mmol of catalyst, indicating that the reaction proceeds beyond the total coverage of catalytic Fe^0 sites. Figure III.16 shows the profiles of the following regeneration step, performed at 855°C with 8% CO_2. Again, complete regeneration of the catalyst could be achieved.

After the fluidized bed tests, the perovskite sample was recovered, weighted and sieved in order to assess an eventual mass loss and particle size reduction. 0.3 g of perovskite were found missing, and 0.1 g of the recovered perovskite had reduced its size below 250 μm. This indicates that the particles reduced their size by attrition and up to 9%$_w$ of the bed inventory might have been lost by elutriation.

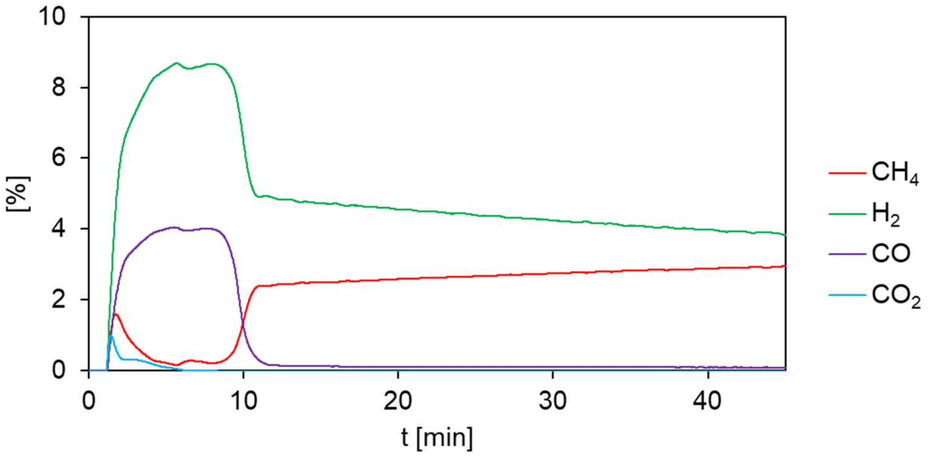

Figure III.16 Perovskite reduction and CH_4 decomposition at 970°C.

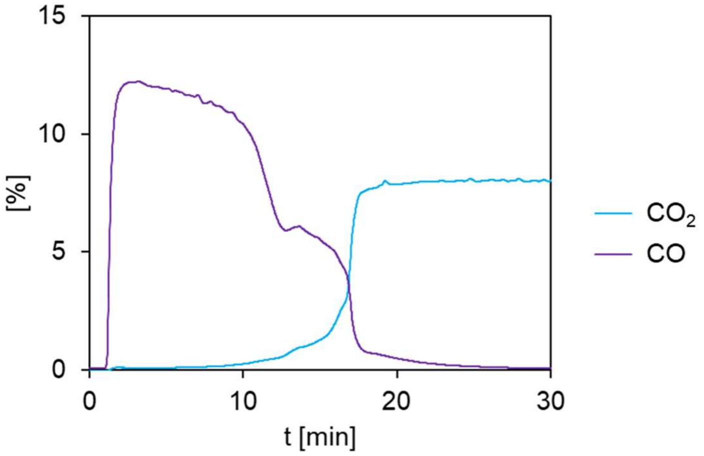

Figure III.17 Catalyst regeneration at 855°C.

Finally, Figure III.18 shows a comparison between the time profiles of the H_2 : CO ratio, and the selectivity toward CO, for the reduction step at 1000 °C in fixed bed conditions and the one at 970 °C in fluidized bed conditions.

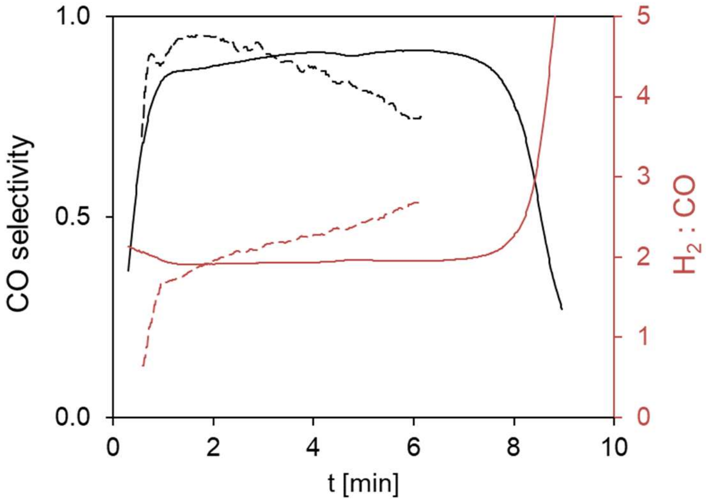

Figure III.18 CO selectivity and H_2 : CO ratio in fixed bed conditions at 1000 °C (dashed line) and fluidized bed conditions at 970 °C (continuous line).

Under fluidized bed conditions, CH_4 decomposition initiates only at the end of the perovskite reduction, as inferred from the obtainment of a nearly constant H_2 : CO ratio of 2 and selectivity of 0.8, throughout most of the experimental run. Differently, under fixed bed conditions, the H_2:CO ratio soon exceeds the value of 2 with a concomitant decrease in the CO selectivity, indicating that CH_4 decomposition starts quite sooner and gradually takes over. This might be explained by the different contacting pattern between the gas reactant and the perovskite bed of particles. The fixed bed conditions combined with the plug flow pattern of the gas phase determine that the layers of the catalyst at the inlet are reduced faster than those at the outlet. This leads to an early start of the decomposition reaction with respect to the complete reduction of catalyst particles. In fluidized bed tests, instead, the solids perfect mixing conditions allow a uniform reduction degree of the particles, delaying CH_4 decomposition at the end of bed solids reduction step.

III.3.3. Directly irradiated fluidized bed

The first results of an experimental campaign with the DIFBAR receiver prototype are here reported. A first experiment was conducted with a bed inventory of 13.5 g (with a perovskite mass fraction of about 12%), a total fluidizing flowrate of 80 NL/h (corresponding to a velocity of about 1.2 m/s) and a constant lamp power of 4 kW_{el}. The test was early interrupted during the first cycle by the agglomeration of the particles, as the receiver temperature had gradually increased up to 1000°C. The addition of the perovskite to the mullite bed had two effects: an increase of the steady state temperatures due to the higher absorptivity of perovskite and a reduction of the temperature at which the bed starts to agglomerate (Figure III.6). The clump was broken, and the particles recovered. The perovskite and mullite particles could not be separated nor distinguished as the whole bed appeared homogeneously made of grey particles, suggesting a physical-chemical interaction between the two materials.

In a successive experiment the solid mass was reduced to 10.2 g to avoid the build-up of the bed level inside the receiver, the total gas flowrate was raised at 120 NL/h to reduce the operative temperatures and the lamp power was switched between 3 kW_{el} and 4 kW_{el} to keep the T1 temperature between 880 and 910 °C. CH_4 and CO_2 concentrations in the feed stream were respectively 14.3 and 8.75%. With these conditions four CLR cycles were successfully conducted, by varying reduction times. Figure III.19 shows the whole time series of the experimental data. The temperatures were controlled in the desired range, but the alternated switch of the lamp power generated a sawtooth profile.

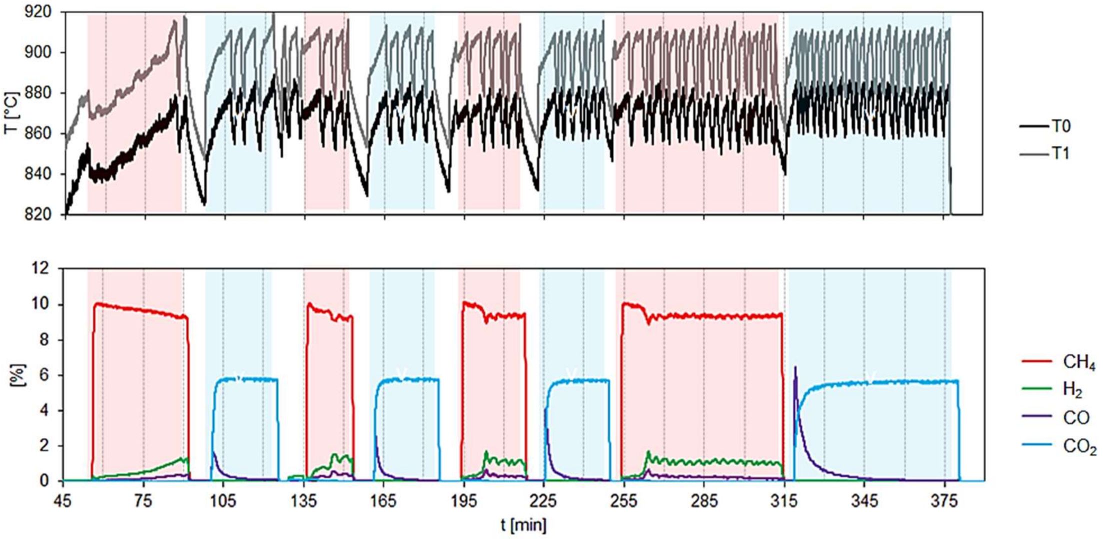

Figure III.19 Chemical Looping Reforming cycles under direct irradiation.

The concentration profiles for all reduction steps are compared in Figure III.20. The first cycle appears quite different from the others probably because the reduction step starts at a lower temperature (T1 = 870°C). From the second cycle on, reduction starts at T1 = 900 °C and the concentration profiles look quite repeatable. CH_4 conversion is far less than in the previous experiments in fluidized bed, but the contact time is largely inferior and so the results are not comparable. After a rise time, CH_4 conversion gets almost steady and so does H_2 productivity. On the other hand, the perovskite conversion proceeds more slowly, as it appears from the persisting concentration of CO: full reduction of the perovskite is not attained even after 1 h. CO_2 production also endures longer than in the fluidized bed experiments. Figure III.21 shows the H_2 : CO ratio for all the reduction steps. Except for the first cycle, the ratio is initially equal to 2 and then increases, as H_2 productivity gets stable, and CO slowly falls to zero, indicating that the CH_4 decomposition starts.

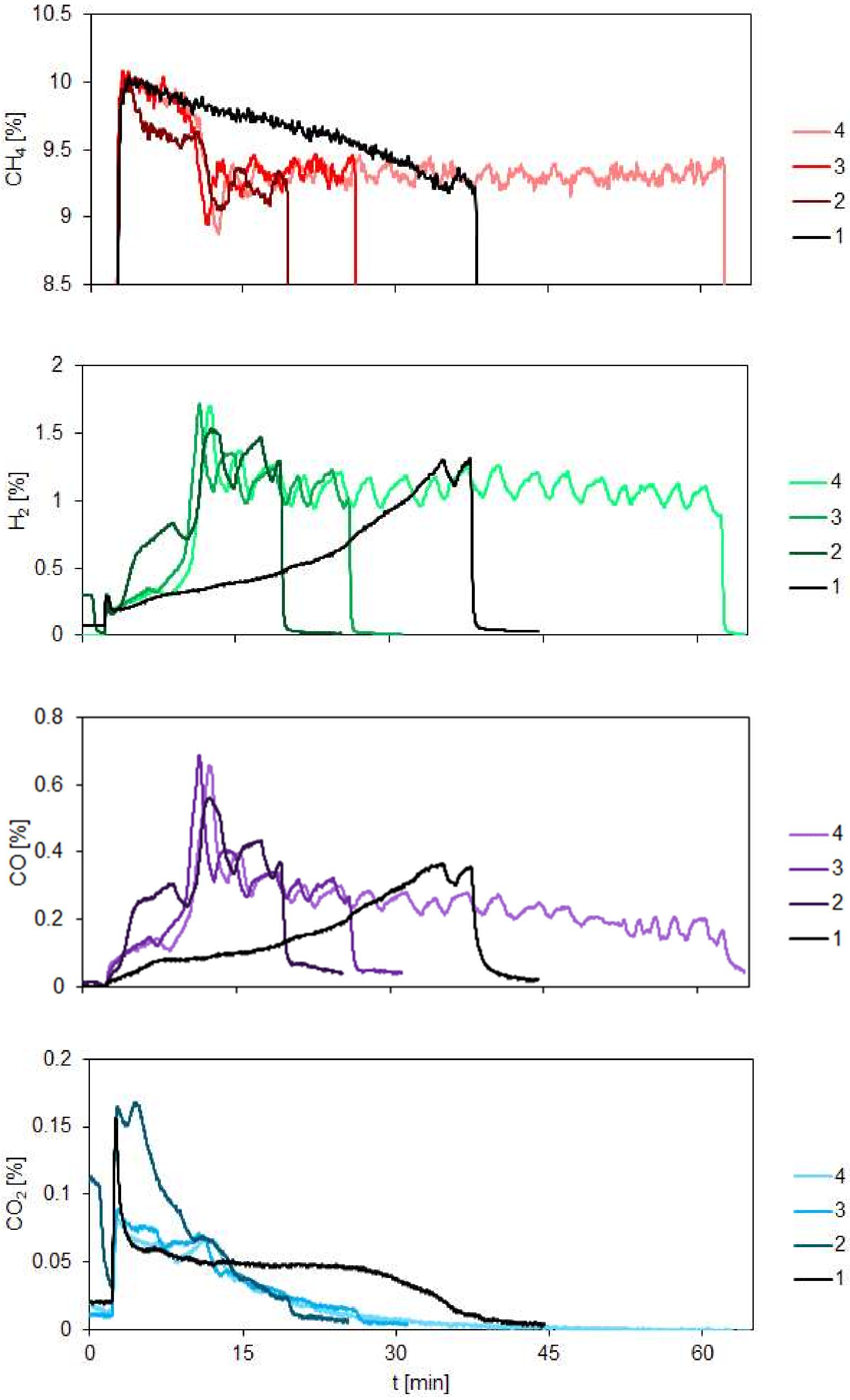

Figure III.20 Concentration profiles during the reduction steps.

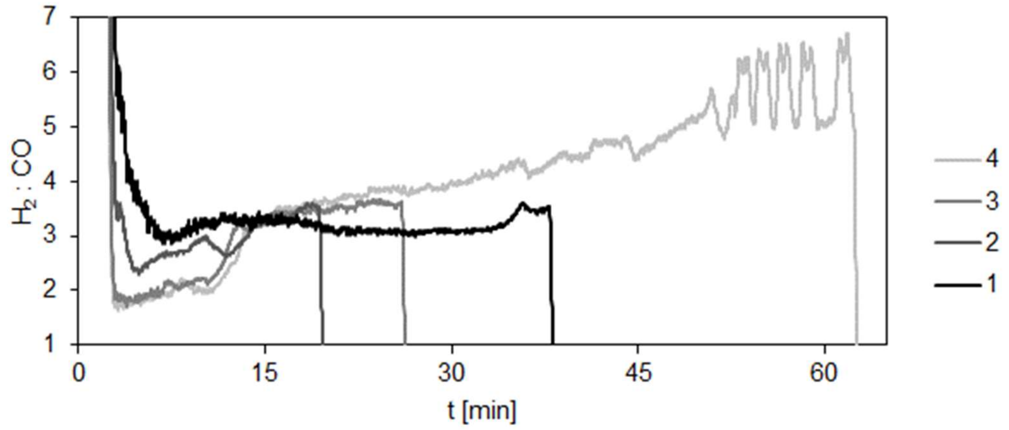

Figure III.21 H_2 : CO ratio during the reduction steps.

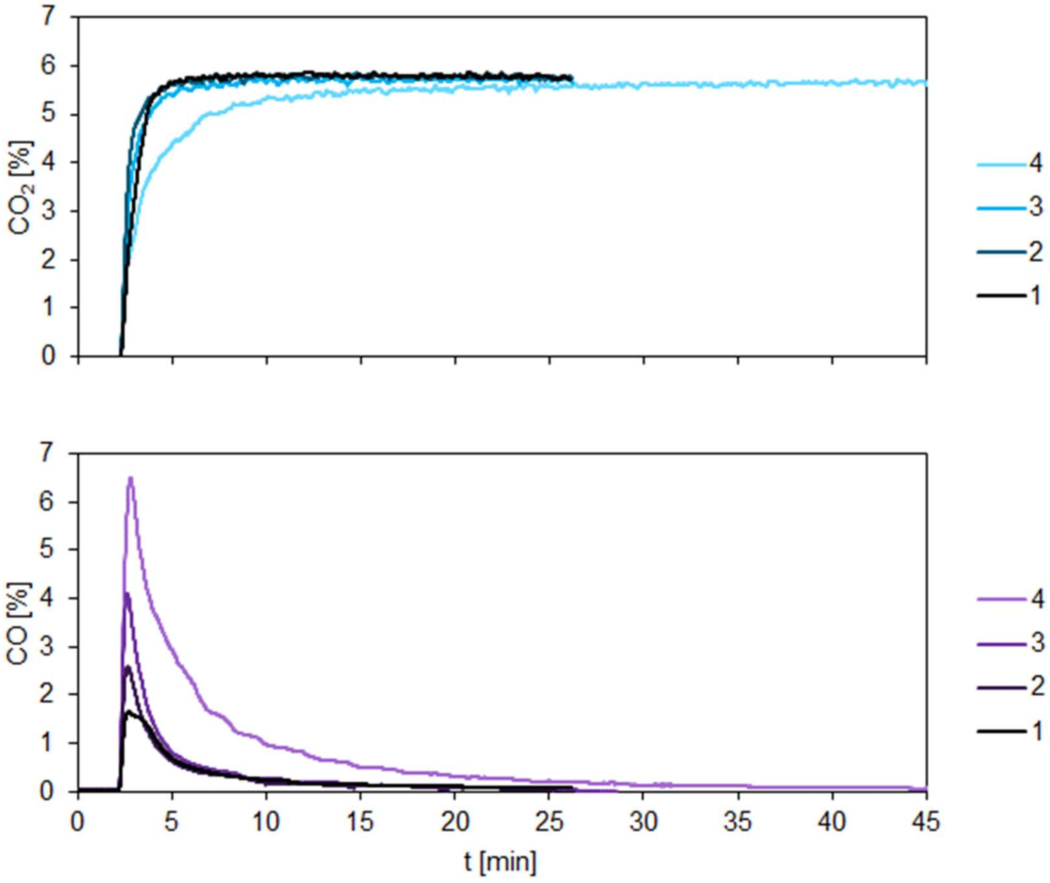

Figure III.22 Concentration profiles during the oxidation steps.

Finally, the concentrations during the oxidation steps are shown in Figure III.22 and confirm the possibility of regenerating the material. The last profile is visibly more pronounced as it follows the longest reduction step. Altogether, the results appear more similar to those in fixed bed conditions, even if the gas-solid contact patterns are more similar to those of a fluidized bed. Further study is needed to understand the reason. The bed materials should be analyzed in order to find if any physical-chemical interaction occurs between the perovskite and the mullite particles, reducing the reactivity of the oxygen carrier.

CHAPTER IV

DIFBAR PROOF OF CONCEPT

IV.1. Design

A new prototype of the DIFBAR has been built and is presented in this last chapter. Stainless steel is chosen as main material, in order to easily machine and assemble the various parts. The Single tank scheme (§I.4) has been thoroughly studied in this work, but the prototype can be assembled also in the Dual Tank and Shaded Reactor configurations thanks to a modular and flexible design: every part can be removed and replaced. It is possible to mount the upper reservoir of the Dual Tank configuration or the receiver of the Shaded Reactor configuration keeping constant the total height of the system, by removing one piece of the annulus. This is necessary to meet the constraint of a fixed distance from the solar simulator, hanging at 4 m above the ground. It is also possible to change specific parts of the reactors to meet variable experimental needs and new aspects might be studied in the future, by customizing replacing parts.

From a hydrodynamic point of view the prototype is a Circulating Fluidized Bed (CFB) composed by a fluidized bed riser, a solid separator (the receiver), a standpipe (the annulus) and a reservoir. The receiver has been designed according to previously acquired knowledge of the research group and is almost identical to the previous prototype presented in Chapter III (Tregambi et al., 2020b). Based on the model calculations reported in Chapter II, the heat exchanger was chosen to be 1 m long and to operate with a solid mass flowrate of about 1.4 g/s. Hydrodynamic control is fundamental for the proper operation of the reactor. As understood from literature on CFBs, the gas pressure loop governs the solid circulation and the gas bypassing, so it must be properly monitored and controlled (Kaiser et al., 2003; Zhang et al., 2009; Suárez-almeida et al., 2021). The devices adopted to control the system are further detailed in the next paragraph.

IV.2. Experimental set-up

IV.2.1. The reactor

Figure IV.1 shows a schematic of the experimental apparatus, whereas a photo of the prototype is pictured in Figure IV.2. The prototype is mainly composed of five parts aligned along a same vertical axis:

i) the riser tube, internal diameter (ID) 10 mm, length 1490 mm;
ii) the annulus tube, ID 20.9 mm, length 1000 mm;
iii) the receiver, upper ID 102.3 mm, length 135 mm, lower internal cone angle 30°;
iv) the reservoir, ID 77.9 mm, length 225 mm;
v) the standpipe, ID 20.9, length 100 mm.

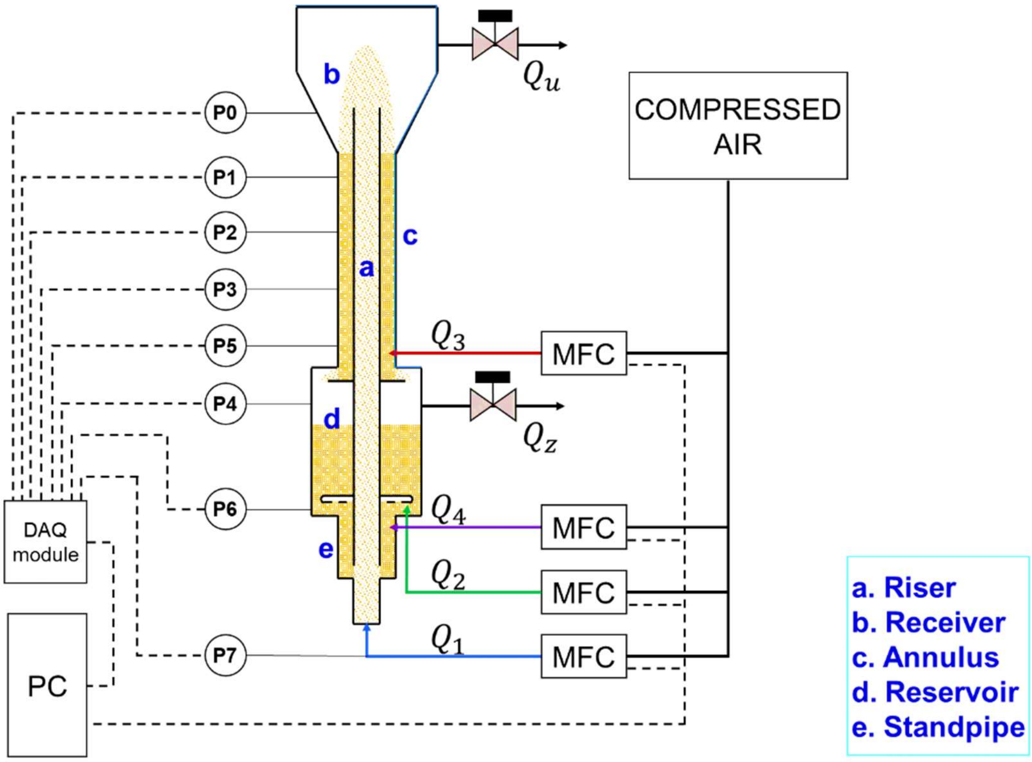

Figure IV.1 Experimental set-up for the hydrodynamic control.

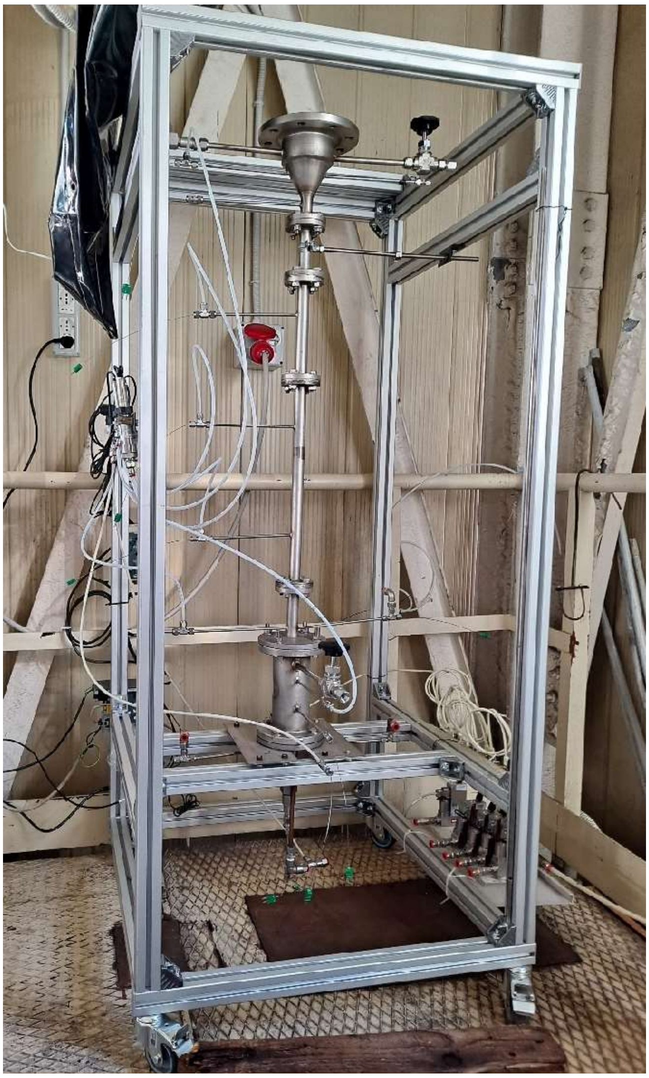

Figure IV.2 Photo of the DIFBAR prototype.

The reactor has been thermally insulated with multiple layers of rock wool blanket and ceramic fiber half-shells for high temperature experiments. All the parts are made of stainless steel (AISI 310 and AISI 316).

The annulus ends are welded directly at the conical bottom of the receiver and at the top flange of the reservoir. The annulus tube is interrupted by four flanged connections, so that three segments can be removed and replaced: a 225 mm segment can be removed to insert a second reservoir for the Dual Tank configuration or the receiver of the Shaded Reactor configuration; a 120 mm segment can be replaced with an identical piece made of Plexiglas, to observe the flow through the annulus in cold flow experiments.

The receiver is sealed at the top by a transparent quartz window (3 mm thick, transmittance of 90% in the 250–2500 μm wavelength range) to let in the solar radiation, concentrated at the top of the riser. A water-cooled flange is used to close the receiver, using a soft gasket.

The standpipe is welded at the bottom flange of the reservoir and connected to the riser by a reducer fitting. The riser protrudes inside the receiver for 35 mm. The solid returns to the riser through four symmetrical orifices (6 mm) at a height corresponding to the bottom of the standpipe.

The reactor is designed to operate with a bed inventory–of 1 - 1.2 kg of sand-like particles. A fluidizing gas stream (Q_1) is fed to the riser, through a nozzle (ID 4 mm). A secondary gas stream (Q_2) can be fed to the reservoir, through a single-ring sparger with seven holes (1 mm), made of a copper bent tube (ID 8 mm). Two additional gas streams can be fed to the lower segment of the annulus (Q_3) and to the standpipe (Q_4) right below the reservoir from two symmetrical tubes (ID 4 mm), to provide a gas-sealing for the reservoir and the receiver. The Q_3 stream also allows an independent control of the solid discharge from the annulus into the reservoir, thanks to a disk of 50 mm, fixed on the riser 4 mm below the annulus: when the Q_3 stream is off, the granular solid inside the annulus lays as a fixed bed, sustained by the disk; when the Q_3 stream exceeds a minimum flowrate, the particles are dragged by the gas and fall into the reservoir. This control device was inspired by the operation principle of an L-valve (Geldart and Jones, 1991; Yang and Knowlton, 1993).

IV.2.2. Measurement and control instrumentation

The gas streams are fed through mass flow controllers from Bronkhorst (El-Flow® Select series). Eight pressure transducers from Keller-Druck (full scale of 100, 200 and 500 mbar) and sixteen K-type thermocouples are installed at various heights through lateral ports. The bottom of the receiver is taken as reference for the vertical position coordinate. The pressure and temperature signals are acquired with modules from National Instruments (NI-9201, NI-9213, NI-cDAQ 9174) and monitored with a desktop PC. A LabView VI application is used to display and record the pressure and temperature measurements and to manage the set points of the mass flow controllers, to obtain desired velocities. A digital feedback control algorithm can be implemented through the VI to keep the bed level in the annulus at the maximum height, by automatic adjustments of the set point of Q_3. The bed level is calculated as the intercept of the pressure profile along the annulus. The control algorithm can be set to keep the bed level at any height but the maximum height allows to exploit the whole heat exchange area.

Two needle valves from DK-LOK (orifice 9.5 mm) on the outlet tubes (ID 10 mm) regulate the exit pressure drops. A piston check valve from VYC Industrial, with an opening pressure of 80 mbar, is installed on a lateral tube of the receiver, to protect the window from overpressures.

The solar simulator consists of a short-arc Xe lamp coupled with an elliptical reflector (Figure IV.3). The lamp input power can be tuned from 2 to 10 kW_{el}, with 1 kW_e increments. Two semi-cylindrical ceramic fiber heaters (Watlow) placed around the reservoir and connected in series is used to speed up the heating phase. The heaters power is controlled with a TRIAC (Sylvania), manually regulated by means of a potentiometer.

Figure IV.3 Photo of the 10 kW_{el} solar simulator.

IV.2.3. Materials

Quartz sand was used for hydrodynamic and heating experiments. Particle sizes are in the range 90-300 μm and the density is 2600 kg/m^3. Bulk density is about 1500 kg/m^3. The minimum fluidization velocity with air was assessed experimentally in a Plexiglas column (ID 40 mm) and resulted 1.8-1.9 cm/s (Figure IV.4). A batch of 93.1 g of magnesium carbonate ($MgCO_3$) with particle sizes in the range 300-400 μm, was added to the sand inventory for calcination experiments. Air supplied by an outdoor gas compressor was used for the operative gas streams. CO_2 from a technical cylinder (99.9% purity) was used for gas tracing experiments.

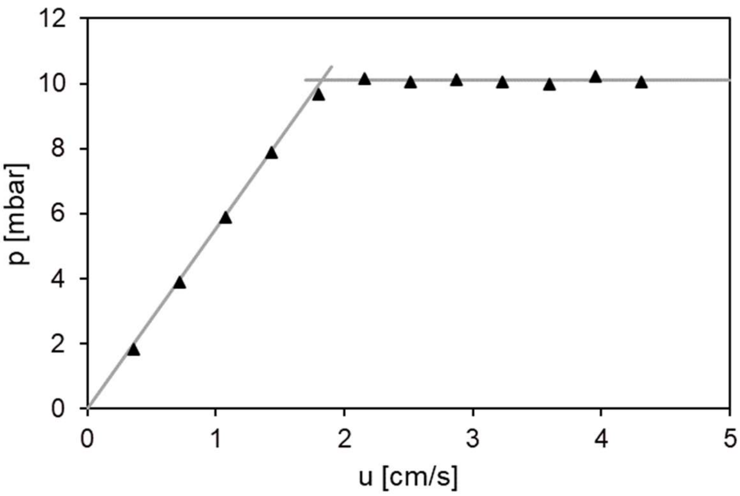

Figure IV.4 Fluidization curves of the sand batch employed for the hydrodynamic study.

IV.3. Hydrodynamic characterization

Cold flow experiments have proved the achievement of design goals, related to the control of solid circulation and gas by-passing.

IV.3.1. Solid circulation rate

The solid circulation rate was determined by two methods. In a first set of experiments, Q_3 was set off, so the annulus bed could not be discharged into the reservoir, and the bed level in the annulus increased. The mass flowrate of the solid flowing through the riser and settling in the annulus could then be calculated, by measuring with a stopwatch the time required to fill the Plexiglas segment between -165 and -75 mm (reference origin at receiver/annulus connection). The bed mass contained in the Plexiglas segment was independently measured by filling it with the bed material. At least five independent tests were run for each condition. By these experiments the solid circulation rate (W) was obtained for both the conditions of open receiver and receiver closed by the window.

A second set of experiments was performed under stable and steady circulation conditions, obtained when the solid mass flowrate in the riser is equal to that discharged from the annulus section. The first one is mainly regulated by the gas flowrate in the riser, Q_1, whereas the Q_3 gas flowrate controls the discharge flowrate of the moving bed in the annulus. A constant level of the bed in the annulus is reached at steady state conditions and, for the optimal autothermal operation, it should be kept at the maximum height. For any circulation condition, a small paper basket with a funnel shape was lowered at the bottom of the receiver to collect the particles flowing out of the riser for a pre-set time interval. Then, by weighing the sample, the mass flowrate could be calculated. At least five independent tests were run for each condition. For these measurements, the receiver had to be open. The results of the two methods match very well, so the first method was assumed to be reliable.

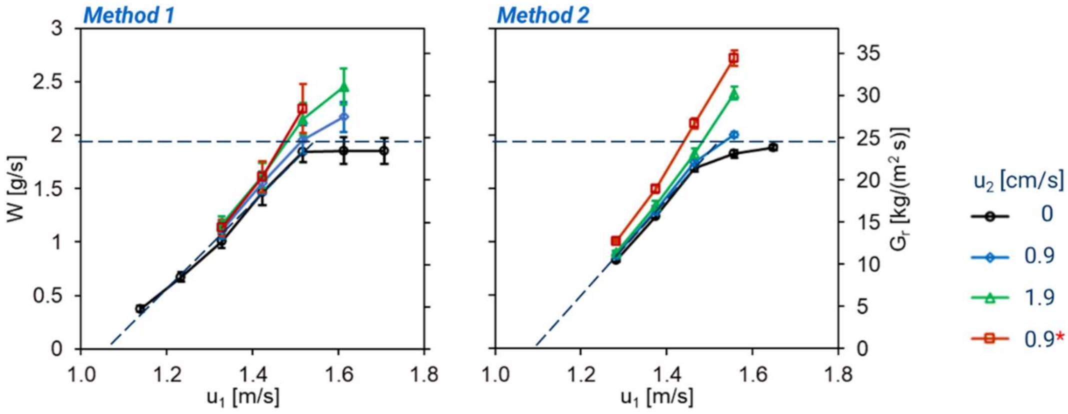

Figure IV.5 Solid circulation flowrate W as a function of the riser feed velocity (u_1) at various reservoir gas velocity (u_2) with the two methods: annulus level rise timing (left) and riser outlet sampling (right). The condition labelled with the asterisk (*) was obtained by partially closing the reservoir outlet valve.

Figure IV.5 reports the mass flowrate of the circulating bed (W), and the corresponding mass flux with respect to the riser section (G_r), as a function of the superficial velocity u_l of the gas fed to the riser. When u_l is increased, the solid circulation rate generally increases with a linear trend. A maximum value close to 2 g/s is asymptotically approached above 1.5 m/s, when the reservoir is not aerated. This limit disappears when the reservoir is aerated, and the pressure is increased either by increasing the flowrate or by increasing the outlet pressure drop of the reservoir. A minimum velocity (u_{min}) of about 1.1 m/s is needed in the riser to have the solid circulation. The height reached by the particles ejected inside the receiver increases with u_l, but the operative velocity range is limited to prevent the particles to impact the window. By increasing u_l, the transition from the slugging to the fast-fluidization regime is visually observed, as at low velocities the particles are ejected into the receiver with intermittent slugs, whereas at higher velocities a fountain-like jet becomes stable.

IV.3.2. Pressure loop

The pressure loop data were recorded during the gas tracing tests. The pressure transducers were carefully calibrated with an external pressure regulator before each test. The pressure at the bottom of the riser could not be measured and was estimated as follows: the pressure P7 was measured in absence of the bed material at different flowrates of Q_l, corresponding to the pressure drop across the feed nozzle. These measurements fitted well a linear correlation with the velocity head (Figure IV.6). The obtained values were subtracted to the corresponding measures during the circulation experiments.

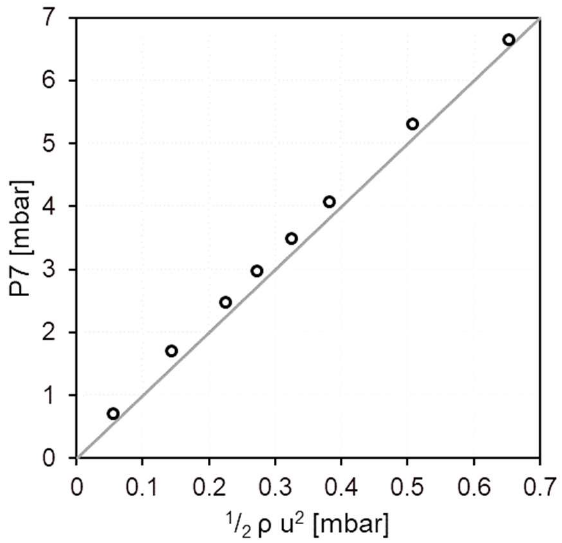

Figure IV.6 Pressure drops across the feed nozzle.

Figure IV.7 shows the different pressure profiles along the vertical axis of the DIFBAR obtained during the experiments for fixed values of u_2, while varying the riser velocity u_1 between 1.3 and 1.5 m/s. By increasing u_1, the bottom pressure of the riser P7 decreases, suggesting that the solid hold-up of the riser is reduced. Average void degrees are estimated in the range 0.95-0.98. Consequently, the pressure drop between the riser and the reservoir (Δp_c = P7 - P6) decreases. By increasing u_2, the bottom pressure of the reservoir P6 increases until fluidized bed conditions are established. Also in this case, Δp_c is reduced. The same reduction of Δp_c can be obtained by partially closing the outlet valve of the reservoir, thus increasing both P4 and P6, but in this way it is possible to keep the reservoir in non-fluidized conditions. P5 also increases because the pressure drop through the L-valve (Δp_L = P5 - P4) remains almost constant. Consequently, the pressure drop in the annulus (Δp_a = P5 - P0) increases.

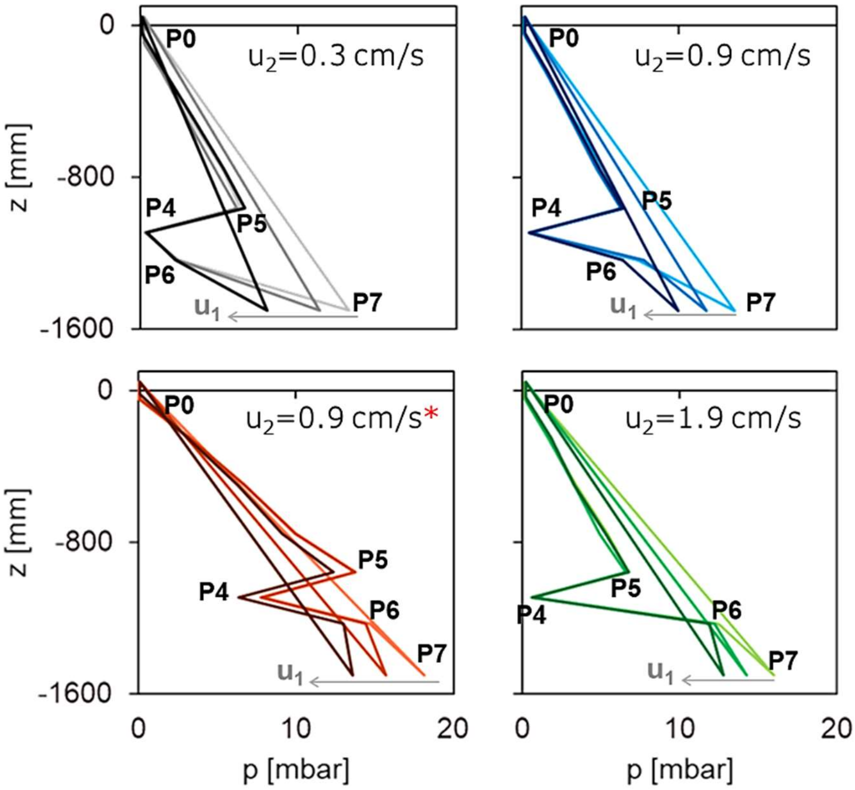

Figure IV.7 Pressure profiles along the vertical axis of the DIFBAR for fixed values of u_2 while varying u_1. The condition labelled with the asterisk (*) was obtained by partially closing the reservoir outlet valve.

IV.3.3. Gas by-passing

Gas streams can flow through the annulus (Q_a) and the lower standpipe connections (Q_c), as shown in Figure IV.8. These streams can either flow upward or downward. Depending on its direction the Q_a stream can cause a dilution or a loss of the gaseous products from the receiver. The Q_c stream, instead, can cause a dilution or a loss of the gaseous reactants fed to the riser. The two connections were carefully designed to minimize the two by-pass flows.

A series of experimental tests were carried out to understand the direction and intensity of these two streams. In these experiments CO_2 was used as a gas tracer, continuously mixed with one of the three inlet streams (Q_1, Q_2 and Q_3). Q_4 was always off in these experiments. An ABB AO2020 Uras 26 gas analyser (CO_2: 0-20%; CO_2: 0-2000 ppm) measured the concentrations of the tracer alternatively from the receiver and the reservoir outlets (y_u and y_z, respectively). A pump (KNF N814KTE) sucked a fixed gas flowrate (45 L/h) for the analyser from one of the two outlets through a tee connection.

Since Q_a and Q_c may have a different direction according to the operating conditions, they are referred to as quantities with a sign. As convention, they will be considered positive if directed upward (Figure IV.8b) and negative if directed downward. In this sense, an increase of these quantities must not be understood necessarily as an increase in absolute value.

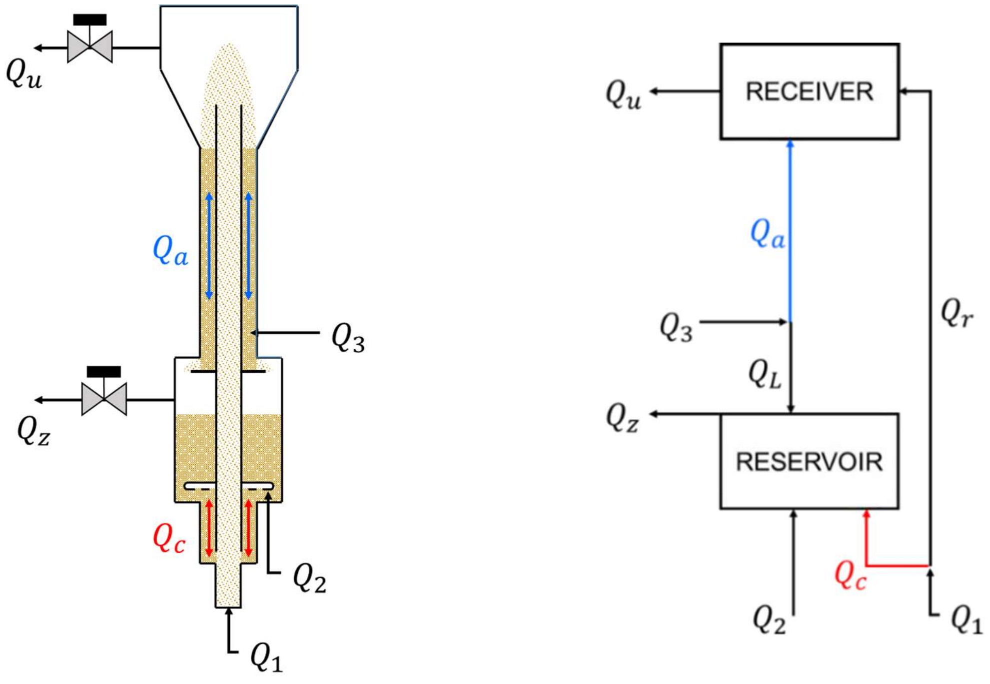

a

b

Figure IV.8 Gas by-passing streams depicted in the reactor sketch (left) and block diagram (right).

The effect of feed flowrates on the gas-bypassing streams Q_a and Q_c can be deduced by the pressure loop in terms of relative changes, by looking at Δp_a

and Δp_c. However, no indication about their sign and intensity can be directly obtained. The gas tracing experiments aimed at investigating such aspects.In a first set of experiments, the tracer was introduced in the Q_3 stream with a fixed flowrate of 10 NL/h (for an inlet concentration y_3 of about 50%) and the receiver outlet concentration y_u was measured. For each condition, except when the outlet valve is partially closed, the concentration was equal to that measured in air (y_{air} = 0.04 %), as shown in Figure IV.7-left, indicating that Q_a is always negative: it flows from the receiver downward along the annulus, dragged by the moving bed, and joins the Q_3 stream.

Then, the tracer was introduced in the Q_2 stream with a concentration of about 20%. Figure IV.9-right shows the y_u concentration for each condition. As it can be seen, in almost every case y_u is equal to y_{air}, indicating that Q_c is positive: it flows from the riser up to reservoir through the standpipe.

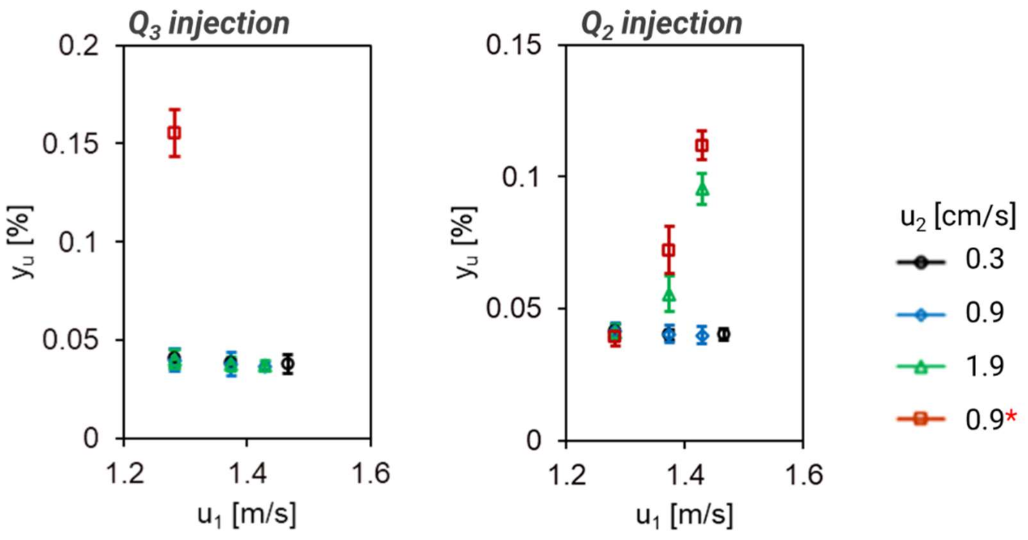

Figure IV.9 Receiver outlet concentration y_u for experiments with injection of the tracer in the Q_3 (left) and Q_2 (right) streams. The condition labelled with the asterisk (*) was obtained by partially closing the reservoir outlet valve.

Differently, when the reservoir is fluidized ($u_2 \geq 1.9$ cm/s) or the outlet valve is partially closed, the direction of Q_c is reversed by the increase of u_1, since the tracer reaches the receiver ($y_u > 0.04$ %). This is coherent with the results of the pressure loops, indicating the decrease of Q_c. This is also a very useful result, indicating the possibility of zeroing the Q_c by-passing stream by regulating the pressure of the reservoir.

At last, the tracer was introduced in the Q_1 stream and both outlet concentrations (y_u and y_z) were measured. From these measures, the outlet flowrates from the receiver (Q_u) and the reservoir (Q_z) can be calculated by solving the global balances:

$$\Sigma_{i=1:3} Q_i = Q_u + Q_z \tag{IV.1}$$

$$\Sigma_{i=1:3} Q_i y_i = Q_u y_u + Q_z y_z \tag{IV.2}$$

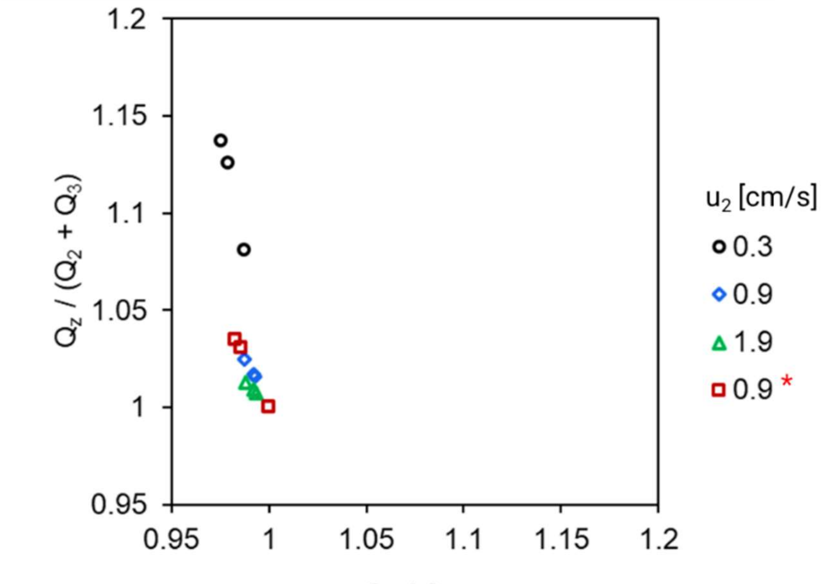

Figure IV.10 Normalized outlet flowrates as calculated from global balances. The condition labelled with the asterisk (*) was obtained by partially closing the reservoir outlet valve.

Ideally, if no by-passing occurred across the two standpipes, $Q_u = Q_1$ and $Q_z = Q_2 + Q_3$. The outlet flowrates are reported in Figure IV.10 in the form of dimensionless ratios, by dividing them with their ideal value. As it appears, the deviations from the ideal ratio of 1 are small, suggesting that the by-passing flowrates are small, though not proving it.

Unfortunately, gas tracing measurements do not provide further information to solve the internal mass balances. However, the by-passing flowrates Q_a and Q_c can be assessed by the following procedure. The relative gas-solid velocities are calculated from the pressure gradient along the two standpipes according to the law of Ergun, as applied to a moving bed (Yoon and Kunii, 1970):

$$\Delta p / L = 150 [(1-\varepsilon) / \varepsilon]^2 \mu u_i / d_p^2 + 1.75 [(1-\varepsilon) / \varepsilon] \rho u_i^2 / d_p \qquad \text{(IV.3)}$$

where ρ is the gas density, μ is the gas viscosity, d_p is the particle diameter, ε is the voidage and u_i is the interstitial relative gas-solid velocity. Then, the absolute superficial gas velocity u_g is obtained by the definition of the relative velocity:

$$u_i = u_g / \varepsilon – G_s / [\rho_s (1-\varepsilon)] \qquad \text{(IV.4)}$$

G_s is the solid mass flux and ρ_s is the particle density. Both u_g and G_s must be taken as quantities with a sign and the same convention is applied: upward flows are positive.

A value of 0.42 was adopted for ε, corresponding to the static voidage, determined from bulk density measurements. Figure 8 shows the results of the calculations in terms of gas by-passing flowrates Q_a and Q_c through the annulus (left) and the standpipe (right) as a function of the riser velocity, for fixed values of u_2.

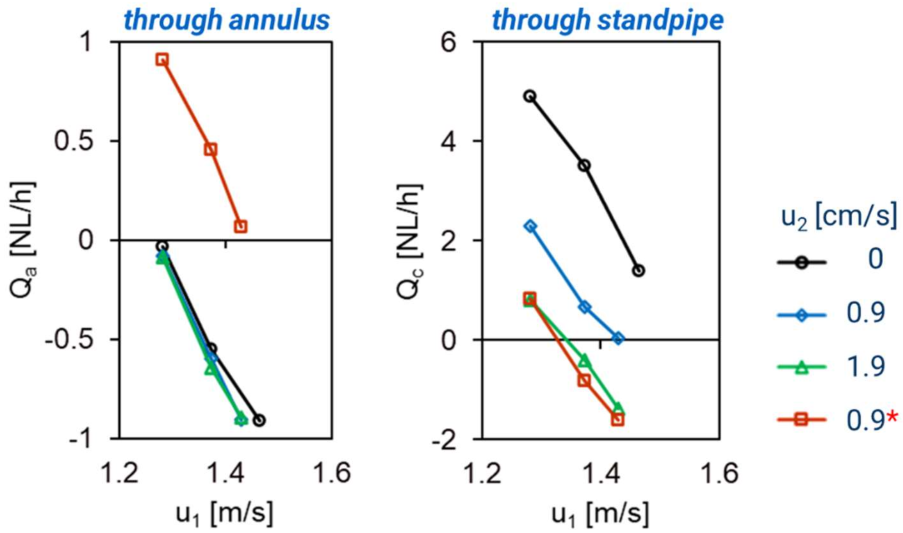

Figure IV.11 Calculated gas by-passing flowrates as a function of the riser velocity for fixed values of u_2: Q_a (left), Q_c (right). The condition labelled with the asterisk (*) was obtained by partially closing the reservoir outlet valve.

The pressure gradient through the annulus does not sensibly change with gas velocities u_1 and u_2 but is affected by the reservoir outlet pressure P4 (Figure IV.5). As a result, the trends of Q_a principally depend on the solid mass flux: as the circulation rate W increases, the by-passing rate Q_a is predicted to decrease (Figure IV.11-left). All calculated values agree with the evidence of a negative Q_a, except when the outlet valve is partially closed. The decreasing trends of Q_c (Figure IV.11-right), instead, are as expected from the pressure loops and the signs in agreement with the tracing experiments.

In conclusion, these results show that the prototype meets the expected operating conditions, necessary for high temperature and reactive experiments, and provide useful knowledge to understand the principles underlying the hydrodynamic control of the system and to improve its design.

IV.4. Thermal characterization

Heating experiments under inert conditions were performed to assess the performance of the heat exchanger. The first heating test was conducted without the assistance of the reservoir heaters, to observe the time evolution of the temperatures obtained by pure irradiation. Thermocouples were installed as in Figure IV.11.

The time evolution of reactor temperatures is shown in Figure IV.12. Temperature profiles have been smoothed with a three-minutes moving average. The thermocouples in the receiver evidence a very rapid heating (over 100 °C/min), but their measurement is probably affected by the absorption of the concentrated radiative flux. Initial heating rates become smaller, by moving down along the annulus. At the bottom of the heat exchanger, the temperature increase appears delayed by 15 min.

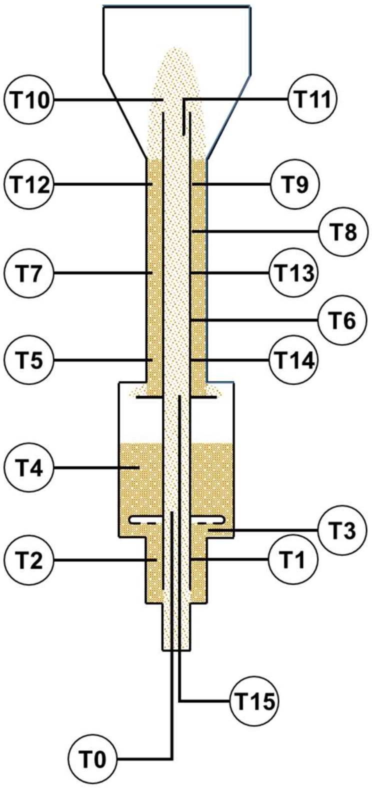

Figure IV.12 Thermocouples scheme.

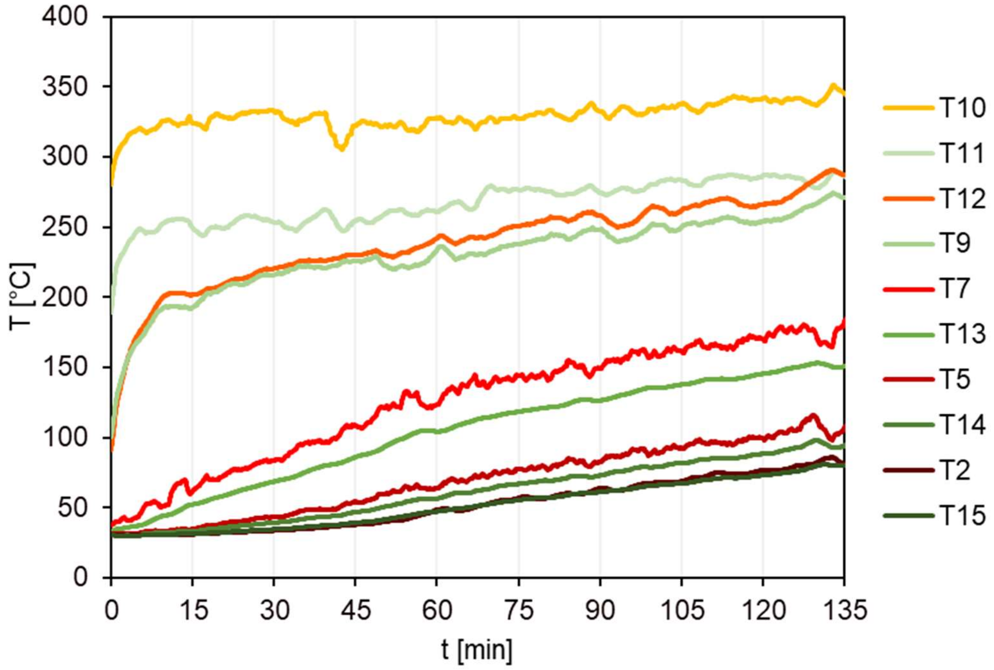

Figure IV.13 Temperature-time profiles.

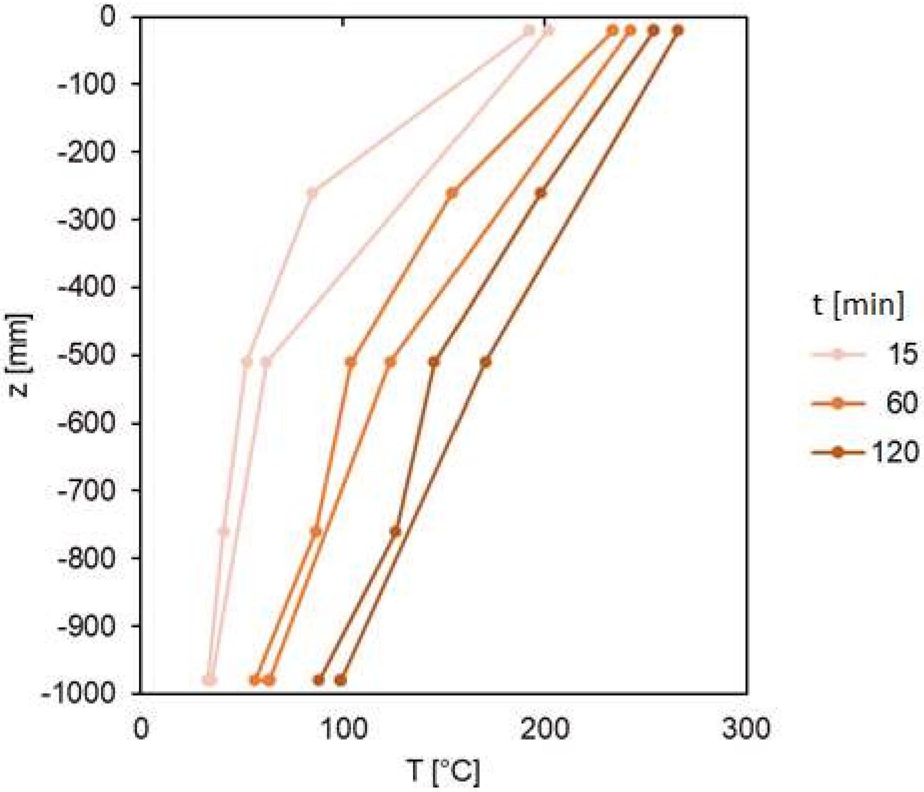

Figure IV.14 Evolution of the temperature profile along the heat exchanger.

Over time, heating rates increase at the bottom of the heat exchanger and decrease at the top. As consequence the shape of the temperature profile changes with time (Figure IV.13). It takes between 1-2 h to achieve a uniform heating rate along the heat exchanger. Correspondingly the temperature profile assumes the classical parallelogram shape.

When heating the reactor, the hydrodynamics slightly changes. The major effect is that the riser gas velocity increases along the axis-coordinate because of thermal expansion. As consequence, the riser exit velocity is higher than the inlet one. According to the ideal gas equation of state, the gas velocity is linear with the temperature and the ratio between the exit and inlet velocity is:

$$u_{rf} / u_{r0} = T_{rf} / T_{r0} \tag{IV.5}$$

The first visible consequence is the increase of the height of the particles jet inside the receiver for a fixed inlet velocity. Therefore, the operating velocity must be limited to prevent impacts with the window. On the other hand, the inlet velocity cannot be lower than the minimum circulation velocity (u_{min}). As a result, the operative range becomes narrower. When the bottom temperature (T_{r0}) is close to ambient temperature (about 300 K), an increase of 300 K along the heat exchanger determines an increase in the riser velocity by a factor $u_{rf} / u_{r0} = 2$. For this reason, it was preferable during the tests to work close to the minimum circulation velocity and with the minimum lamp power: in particular the inlet riser velocity was $u_{r0} = 1.2$ m/s and the lamp power was 2 kW_{el}. If higher velocities are needed, it is possible to increase the distance of the window from the riser, with an extension segment. However, with the increase of the bottom temperature (T_{r0}) the velocity ratio becomes smaller, widening the operative range. For the design value of T_{r0} (about 900 K), the velocity ratio would be $u_{rf} / u_{r0} = 1.33$. So, in the successive experiments, the reservoir heaters were used to boost the increase of T_{r0}, while increasing the lamp power. After a while the heaters were switched off to let the temperatures settle and assess the performance of the heat exchanger with pure irradiation.

By a global energy balance (Eq. (II.6a)), the net power (P_{net}) absorbed by the receiver should be 29 W. The mean temperature difference between the riser and the annulus is $\Delta T_f = 16.7$ K, corresponding to an enthalpy change for the solid passing through the receiver of $\Delta H_f = 16.5$ J/g. The temperature increase along the heat exchanger is $\Delta T_{ex} = 169$ K, corresponding to an enthalpy change for the solid of $\Delta H_{ex} = 157$ J/g. By these considerations a heat recovery factor (*R*) of 91% can be calculated as:

$$R = \Delta H_{ex} / (\Delta H_{ex} + \Delta H_R) \qquad \text{(IV.6)}$$

This means that 91% of the heat duty to heat the solid at the temperature of the receiver is recovered by the heat exchanger. The solid circulation rate (W) is necessary to calculate the power exchanged (P_{ex}) and then the heat transfer coefficient (U) as in Eqs. (II.4a) and (II.7). W was determined by cold flow data (Figure IV.3), by taking as reference the velocity at the riser mid-height ($u_l = 1.4$ m/s, $W = 1.2$ g/s). This choice is supported by the result of simulation with a transient model described in the Appendix. The heat transfer coefficient results to be $U = 374$ W/(m^2 K) in reasonable accord with the expectations (§II.2.4).

Figure IV.15 shows steady temperature profiles obtained for three different lamp powers. The same analysis is repeated, and the results are gathered in Table IV.1. By increasing the irradiation power, the slope of the temperature profiles increases, indicating an increasing efficiency of the heat exchanger and the heat transfer coefficient appears effectively to increase. The heat recovery factor *R* remains close to 90%. These results clearly confirm that autothermal operation of the reactor is feasible.

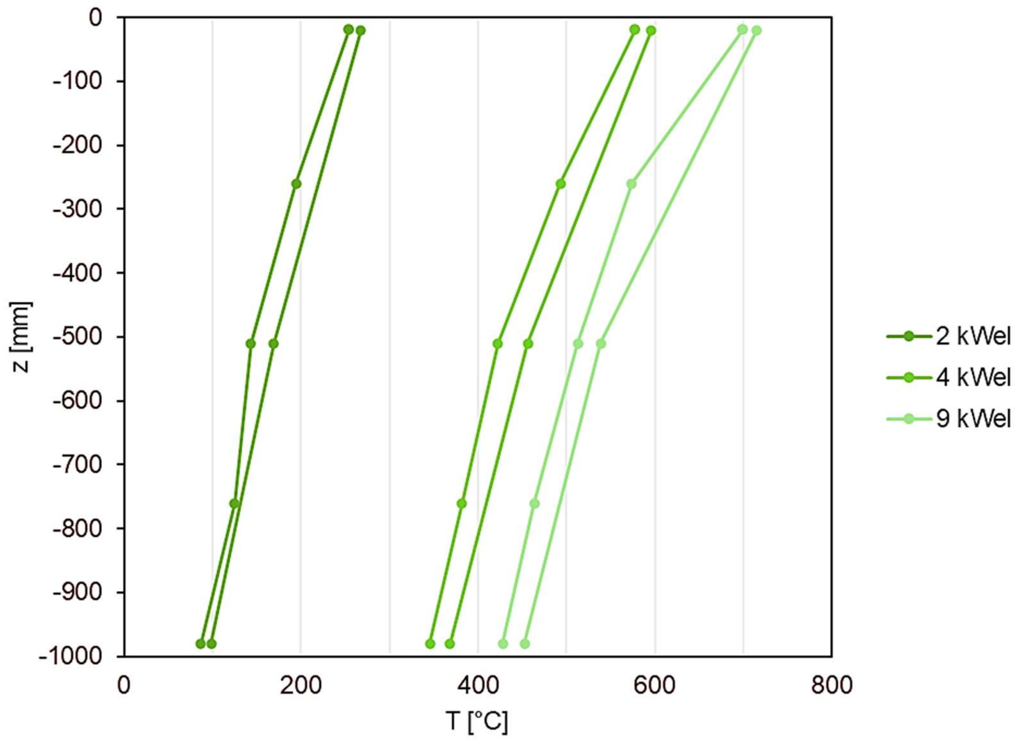

Figure IV.15 Temperature profiles along the heat exchanger for different lamp powers.

ΔT_{ex} [K]	ΔT_f [K]	***R*** -	P_{net} [W]	**U** [W/(m^2 K)]
169	17	91%	29	374
228	25	90%	53	397
263	22	92%	56	538

Table IV.1 Results of the thermal characterization for different lamp powers.

IV.5. Operation with reactive conditions

A first calcination experiment was conducted to test the operability of the DIFBAR prototype as a solar reactor. A batch of $MgCO_3$ particles was loaded in the reactor and mixed with the sand inventory for a mass fraction of 8.0%. The calcination rate is calculated from the CO_2 concentration in the receiver outlet gas (y_u):

$$\dot{n} = F_1\, y_u / (1 - y_u) \tag{IV.7}$$

To rate the performance of the reactor, some evaluations are introduced. The global conversion degree can be obtained by the integral:

$$X_g = \int \dot{n}\, M_{MgCO3}\, dt / (\, m\, \alpha_0\,) \tag{IV.8}$$

where M_{MgCO3} is the molar mass of $MgCO_3$, m is the total mass inventory and α_0 is the initial mass fraction of the solid reactant. As the receiver is operated as a continuous reactor, it also possible to assess its local conversion degree:

$$X_f = \dot{n}\, M_{MgCO3} / (\, W\, \alpha\,) \tag{IV.9}$$

The instantaneous mass fraction α of the solid reactant must be updated with time:

$$\alpha = \alpha_0\, (1 - X_g) \tag{IV.10}$$

At last, the heat recovery factor can be reformulated as:

$$R = W\, \Delta H_{ex} / (W\, \Delta H_{ex} + W\, \Delta H_f + \dot{n}\, \Delta H_{298}) \tag{IV.11}$$

where ΔH_{298} is the enthalpy change of the reaction: 118.2 kJ/mol.

Figure IV.16 shows the evolution of the CO_2 produced and of the global conversion degree (X_g). To obtain a significant calcination rate, it was necessary to increase the residence time of the particles inside the receiver. This was possible, by simply tuning the control algorithm for the level of the annulus bed (§IV.2.3), to fill the receiver up to a certain height. Taking the riser outlet as a reference height, a volume of about 50 cm^3 could be filled, corresponding to a residence time of the order of 1 min. Operating the reactor with this strategy, an average calcination rate of 5.7 mmol/min was obtained between 180 and 260 min, peaking at 30 mmol/min, corresponding to local conversion degrees (X_f) respectively of 12 and 69 %.

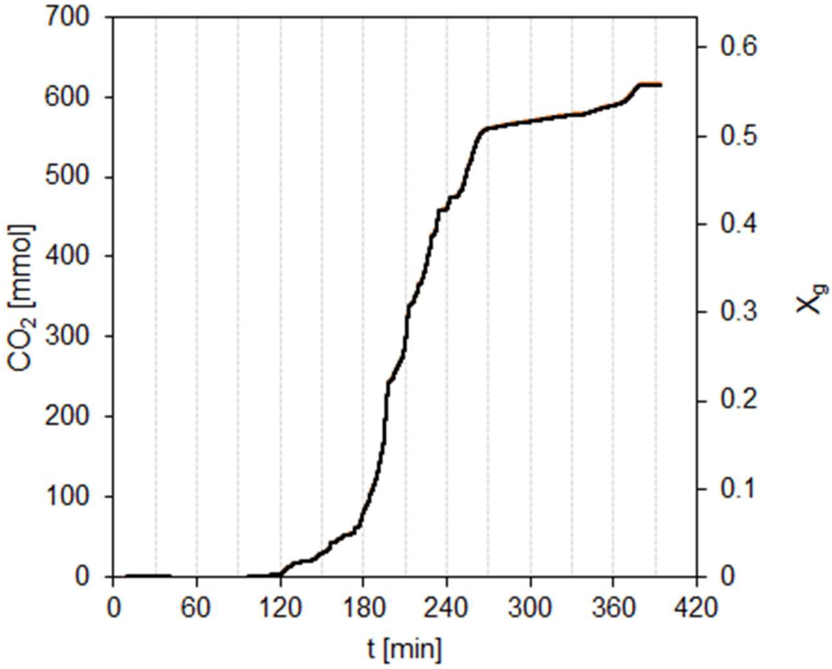

Figure IV.16 Cumulative CO_2 production and global conversion degree during the calcination test.

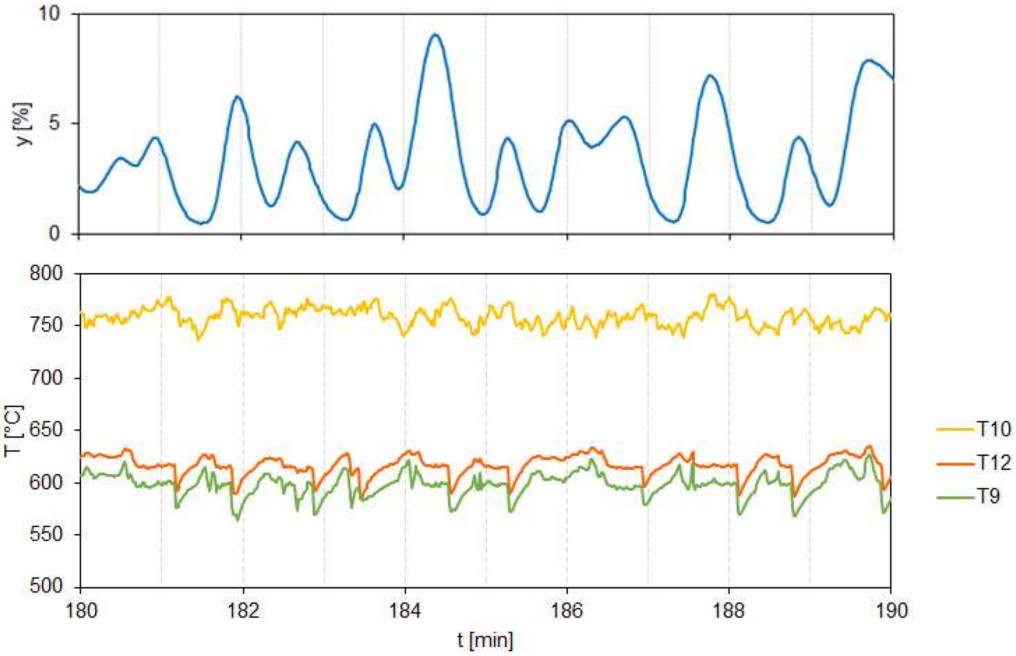

Figure IV.17 CO_2 and temperatures signals during stable operation.

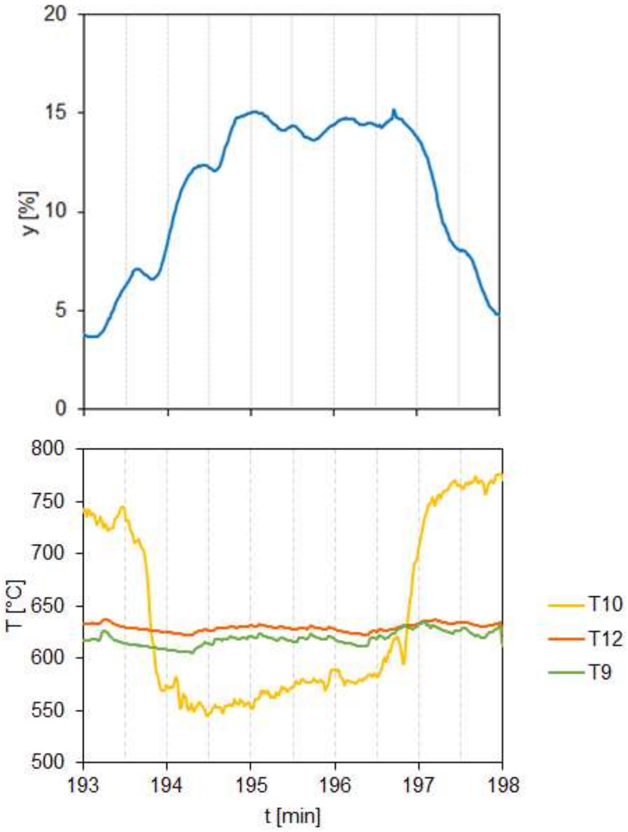

Figure IV.18 CO_2 and temperatures signals for a surge of the bed level.

The calcination rate strongly fluctuates due to oscillations of the bed level. Figure IV.17 shows the CO_2 and temperatures signals during a relatively stable period ($\dot{n}$ = 4.8 mmol/min, X_f = 7.4%). Between 193 and 197 min the bed level was raised over the riser outlet, as evidenced by the temperature drop of the T10 thermocouple, shown in Figure IV.18. Correspondingly, the calcination rate highly increased ($\dot{n}$ = 22 mmol/min, X_f = 37%).

At last Figure IV.19 shows the temperature profile averaged on the interval between 180 and 190 min. The heat recovery factor is calculated R = 89%, only slightly reduced by the reduction term. The temperatures are lower than those of experiments with inert sand, even if the power of the solar simulator is the same. The cause is probably the deposition of carbonate fines on the window, that reduced the transmittivity.

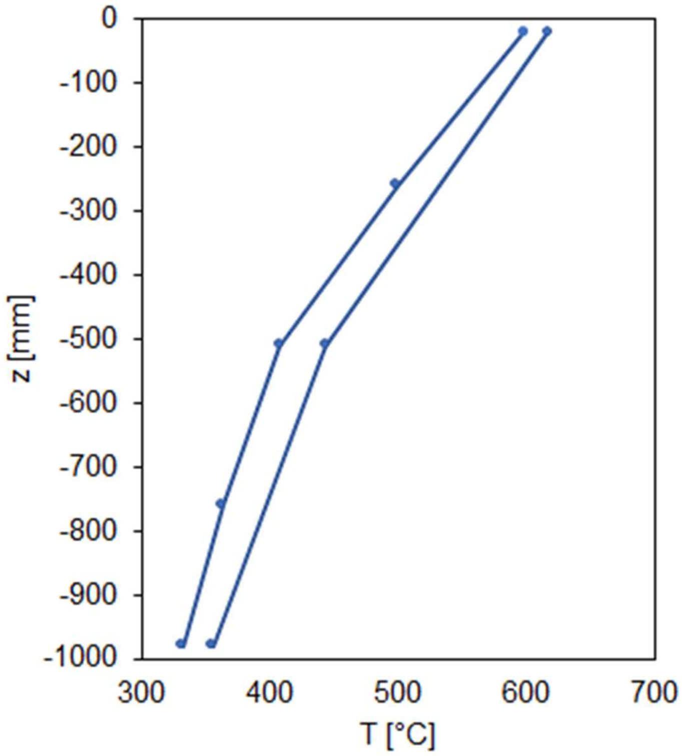

Figure IV.19 Temperature profile during stable operation.

CONCLUSIONS

The aim of this Ph.D. thesis is the full proof-of-concept of the Directly Irradiated Fluidized Bed Autothermal Reactor (DIFBAR). The three-years research project included modeling, design and experimental activities and culminated with the realization and full characterization of a new DIFBAR prototype. Secondary achievements are the development and validation of a compartmental model of the DIFBAR, as a practical design tool and the experimental study of a solar thermochemical process for the production of hydrogen in bench reactors, in view of an application with the new DIFBAR prototype.

In Chapter II the compartmental model, based on steady state thermal balances is presented. The application of the DIFBAR as a “thermochemical battery” has been explored, considering the Single Tank scheme and Calcium Looping as reference process. The solid circulation rate strongly influences the length of the heat exchanger that is necessary to keep the operational temperatures at the pre-set values. An optimal receiver temperature is found around 880–900°C, for which the length of the heat exchanger can be minimized, and charge efficiency maximized. The discharge reaction takes place in the reservoir. The discharge time and power can be varied with negligible influence on the efficiency and temperature and are adaptable to process needs. These results served as a basis to size the new prototype, in particular the heat exchanger was chosen to be 1 m long and to operate with a solid mass flowrate of about 1.4 g/s. The compartmental model has been extended to simulate transient operation and experimental data have been used for validation, as shown in the Appendix.

In Chapter III the results of the solar thermochemical process for the production of hydrogen are presented. A laboratory-produced perovskite with chemical formula $La_{0.6}Sr_{0.4}FeO_3$ has been tested for Chemical Looping Reforming of CH_4. Tests have first been carried out in a fixed bed reactor and a fluidized bed reactor and then in an experimental unit, reproducing the

DIFBAR receiver. Temperature-programmed experiments indicate that the reduction can be performed at temperatures above 800°C and the oxidation above 600°C. The perovskite can be reduced up to a non-stoichiometric value of $\delta = 1.5$, so 0.6 Nm^3 of syngas per kg of catalyst per cycle can be obtained from reactions (I.6)-(I.8). Except for a brief initial stage, the reduction yields synthesis gas with a selectivity around 90%. Decomposition of CH_4 can occur, catalyzed by the reduced oxide and can be limited by interrupting the reduction step. Carbon deposition does not deactivate the oxygen carrier, that is fully regenerated during the oxidation step, thanks to gasification reactions. No sign of a loss of reactivity was evidenced by determining the perovskite conversion degrees for several cycles at different temperatures. Fluidized bed tests showed higher conversion rates compared to fixed bed conditions and allowed a better control of CH_4 decomposition. The results encouraged to test the material with the DIFBAR receiver test unit. For this reason, a batch of perovskite was mixed with the reactor bed inventory, made of mullite. Unlike what expected, the reaction proceeded with a slower rate than in fluidized bed conditions. Further analysis is needed to understand the reason. An explanation might be sought in the physical-chemical interaction between the perovskite oxygen carrier and the mullite. The selection and preparation of bed materials is a fundamental aspect, that will be further examined in the future, in view of the implementation of this process with the new DIFBAR complete prototype .

The new DIFBAR prototype is presented in Chapter IV. The prototype has been assembled in the Single Tank scheme in this work, but thanks to a modular design it can be customized, by changing specific parts, to test different configurations and meet variable experimental needs. From a hydrodynamic point of view the prototype is a Circulating Fluidized Bed composed by a fluidized bed riser, a solid separator (the receiver), a standpipe (the annulus) and a reservoir. Cold flow experiments verified the efficacy of the adopted control systems and highlighted the effect of operative variables on the solid flowrates and gas by-passing flowrates. The solid circulation flowrate (W) is mainly regulated with the riser fluidization velocity (u_1) and can be set to the target value of 1.4 g/s, assumed for the operation of the heat exchanger. The reservoir can be operated as a moving or fluidized bed with a secondary gas feed (Q_2). When the reservoir is not aerated, the solid circulation flowrate W shows an upper limit of about 2 g/s. This limit disappears when the reservoir is aerated, and its bottom pressure is increased either by increasing the gas velocity or by increasing the outlet pressure drop. The discharge flowrate from the annulus is regulated with a non-mechanical valve, inspired to an L-valve, operated with an auxiliary gas stream (Q_3). Pressure measurements are used to monitor and control the annulus bed level, which is fundamental for the effective heat transfer to the riser. Calculations indicate that the gas by-passing flowrates through the two standpipes connections are very small (less than 2% of the riser feed). In addition, gas tracing tests have shown evidence that by-passing flows can be reversed and therefore reduced to zero by tuning the operating conditions. Then, the prototype was insulated and heated with an in-house built high-flux solar simulator for high temperature experiments. A characterization of the heat exchanger was conducted by operating the prototype with inert sand. The heat transfer coefficient ranges between 374 and 538 W/(m^2 K) and meets the design expectations. A heat recovery factor has been calculated of 90%, demonstrating clearly that autothermal operation of the reactor is feasible. The receiver temperature reached 700°C, well below the design target of 900°C, indicate an efficiency of absorption of the solar radiation lower than expected. However, temperatures were sufficiently high to perform calcination tests with $MgCO_3$. A batch of $MgCO_3$ particles, loaded in the reactor and mixed with the sand inventory for a mass fraction of 8.0%. To obtain a significant calcination rate, it was necessary to increase the residence time of the particles inside the receiver to about 1 min, by increasing the bed level up to a about the riser outlet. Operating the reactor with this strategy, an average calcination rate of 5.7 mmol/min was obtained, peaking at 30 mmol/min, corresponding to local conversion degrees (X_f) respectively of 12 and 69 %. Half conversion was reached in 2-3 h. These preliminary reaction tests provide a first demonstration of the working principle of the DIFBAR, and the results obtained lay the groundwork for future studies. The optimization of operating conditions is an activity that will immediately follow this thesis, with a particular focus on bed material properties. Additional efforts might also be needed to optimize the design of the receiver, to maximize radiative absorption and chemical conversion. Thanks to the modular design of the prototype, it will be possible to modify specific parts according to experimental purposes. It will also be possible to test the alternative plant schemes presented in Chapter I. The main long-term objective of this research is the application of the DIFBAR to more challenging solar processes, like the production of solar fuels and materials.

APPENDIX

The compartmental model presented in Chapter II, is here extended to simulate transient behavior. The only differences are that unsteady balance equations are written, and a 1-D model is used to describe the heat exchanger. The nomenclature is the same with the addition of few symbols.

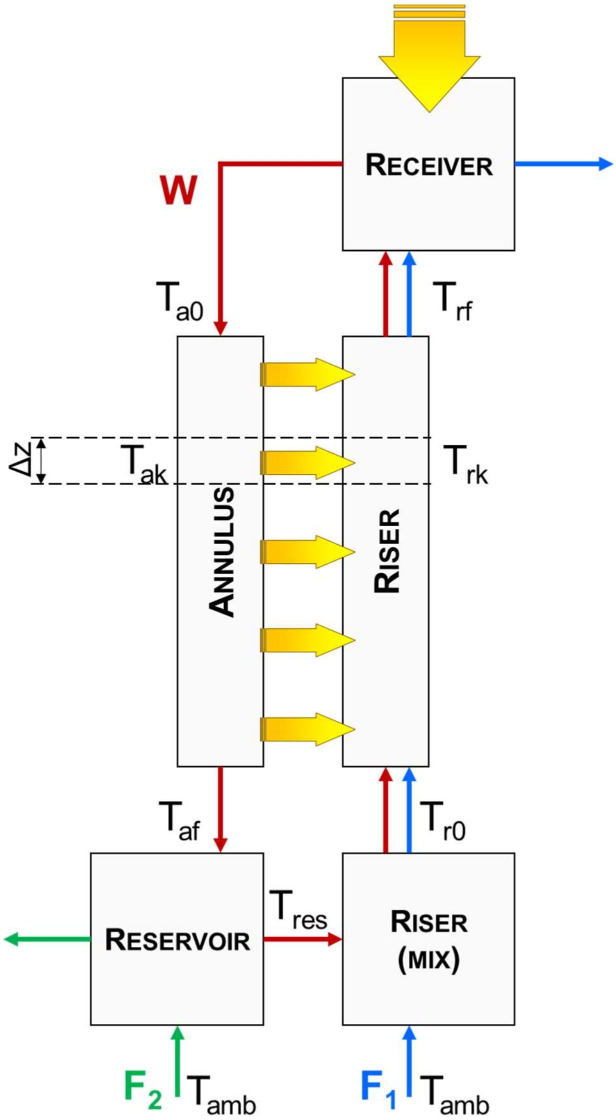

Figure A.1 Compartmental model of the DIFBAR with distributed parameters.

The energy balances for the annulus and the riser are written in local form, assuming a plug flow:

$$\rho_s (1-\varepsilon_a) S_a c_p \partial T_a / \partial t = W c_p \partial T_a / \partial z - U a (T_a - T_r) \quad (A.1)$$

$$\rho_s (1-\varepsilon_r) S_r c_p \partial T_r / \partial t = - W c_p \partial T_r / \partial z - F_1 c_{pg} \partial T_r / \partial z + U a (T_a - T_r) \quad (A.2)$$

where ρ_s is the solid density, ε_a and ε_r are the annulus and riser void degrees, S_a and S_r are the annulus and riser cross-sections, c_p and c_{pg} are the solid and gas specific heat capacities. The z-axis is upward oriented, and its origin is set at the bottom of the receiver.

The boundary conditions change dynamically and must be calculated by the energy balances on the other compartments:

$$m_f c_p dT_{a0} / dt = W (H_{rf} - H_{a0}) + P_{net} \quad (A.3)$$

$$m_{res} c_p dT_{res} / dt = W (H_{af} - H_{res}) + F_2 (h_{amb} - h_{res}) \quad (A.4)$$

$$m_{r,mix} c_p dT_{r0} / dt = W (H_{res} - H_{r0}) + F_1 (h_{amb} - h_{r0}) \quad (A.5)$$

where m_f, m_{res} and $m_{r,mix}$ are the solid mass in the receiver, the reservoir and the riser zone below the heat exchanger. Equations (A.3)-(A.5) are solved by setting:

$$T_a (0) = T_{a0} \quad (A.6)$$

$$T_r (-L) = T_{r0} \quad (A.7)$$

$$T_a (-L) = T_{af} \quad (A.8)$$

$$T_r (0) = T_{rf} \quad (A.9)$$

At the same time, (A.6) and (A.7) are the boundary conditions of Eqs. (A.1) and (A.2).

Equations (A.1)-(A.2) are discretized by dividing the heat exchanger in N-1 slices with thickness $\Delta z = L / (N - 1)$:

$$\Delta m_a c_p dT_{ak} / dt = W (H_{ak-1} - H_{ak}) - U a \Delta z (T_{ak} - T_{rk}) \qquad \text{(A.1-k)}$$

$$\Delta m_r c_p dT_{rk} / dt = W (H_{r+1} - H_{rk}) + F_1 (h_{r+1} - h_{rk}) + U a \Delta z (T_{ak} - T_{rk}) \qquad \text{(A.2-k)}$$

where:

$$\Delta m_a = \rho_s (1\text{-}\varepsilon_a) S_a \Delta z \qquad \text{(A.10)}$$

$$\Delta m_r = \rho_s (1\text{-}\varepsilon_r) S_r \Delta z \qquad \text{(A.11)}$$

Each of the N-1 equations (A.1-k)-(A.2-k) are solved numerically with an explicit first-order finite difference scheme. The time step is chosen by setting the Courant number:

$$Cou = W \Delta t / \Delta m_r \qquad \text{(A.12)}$$

This model has been applied to simulate the first heating test shown in Chapter IV.1. The parameters used in the simulation are the following.

The following assumptions were made:

$\varepsilon_r = 0.96$

$\varepsilon_a = \varepsilon_{res} = 0.43$

$m_f = 0.001$ kg

$m_{res} = \rho_s (1-\varepsilon_{res}) S_{res} L_{res}$

$m_{r,mix} = \rho_s (1-\varepsilon_r) S_r L_{r,mix}$

$L_{res} = 0.060$ m

$L_{r,mix} = 0.400$ m

Initial temperatures were set to $T_{amb} = 30°C$. The net power (P_{net}), the solid circulation rate (W) and the heat transfer coefficient (U) were assumed constant and set by the experimental data presented in Chapter IV. After a few attempts, the parameters of the numerical solver were set to be N = 101 and Cou = 0.5.

The time evolution of the temperatures obtained from the simulation is compared with the experiment in Figure A.2. Figure A.3 shows the comparison between the temperature profiles at 120 min.

The simulation fits well experimental data, considering that a fair number of assumptions are made and some of the internal variables are uncertain (like volumes and void degrees). A better agreement might be obtained by varying those variables and maybe applying a *machine learning* technique. On the other hand, to reduce the dependence on experimental data, a preferable approach would be the integration of *predictive models*. The prediction of the heat transfer coefficient, based on the properties of the annulus and riser beds, would be a considerable achievement. Furthermore, the riser equation (A.2) might eventually be improved, by considering more realistically a decaying void degree profile and an axial dispersion term. However, such developments are outside the scope of this Ph.D. thesis.

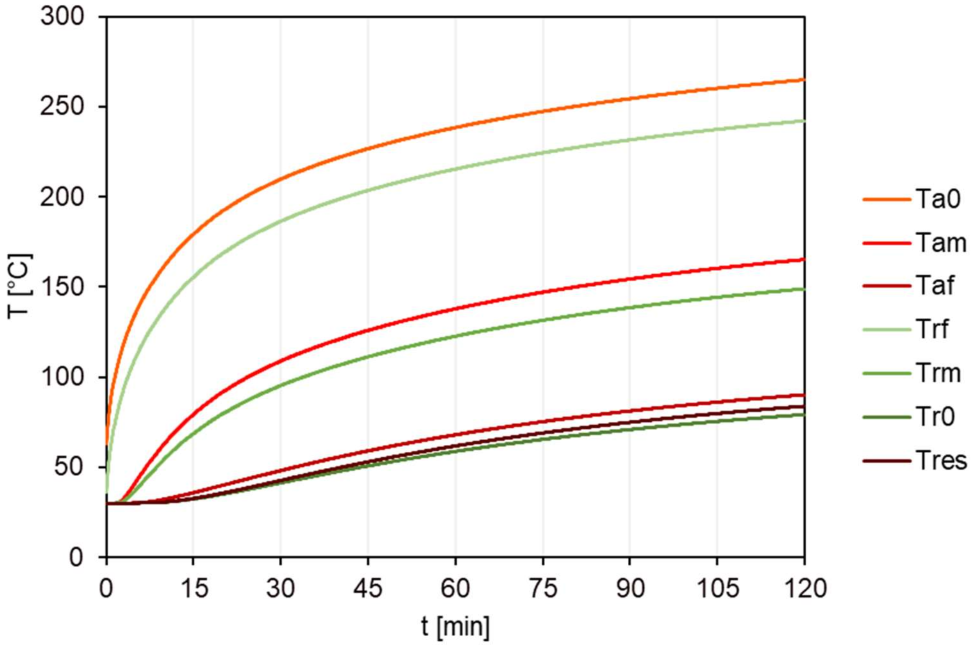

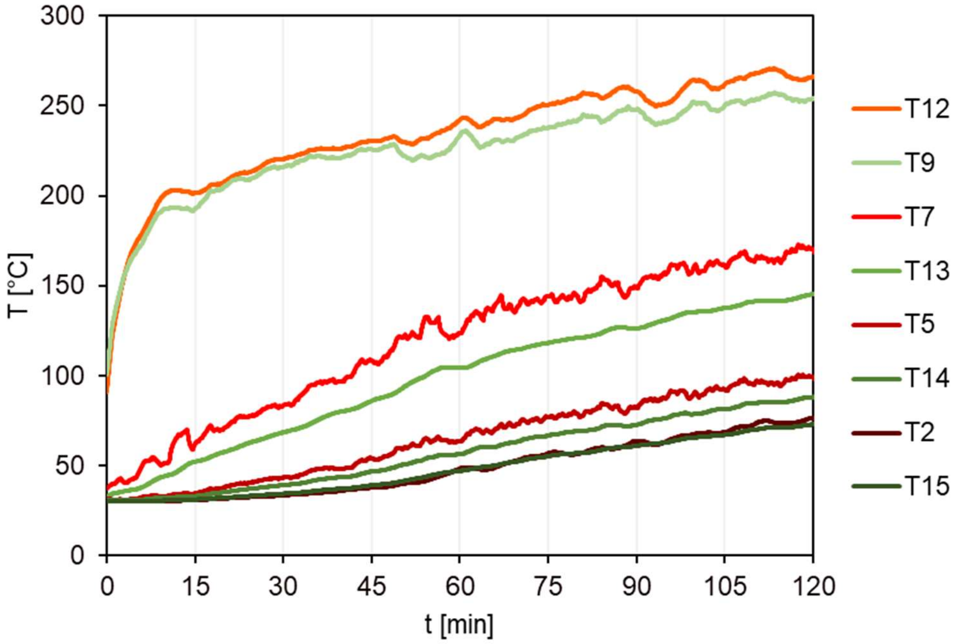

Figure A.2 Time evolution of the temperatures of the heat exchanger: simulation (up) vs. experimental data (down).

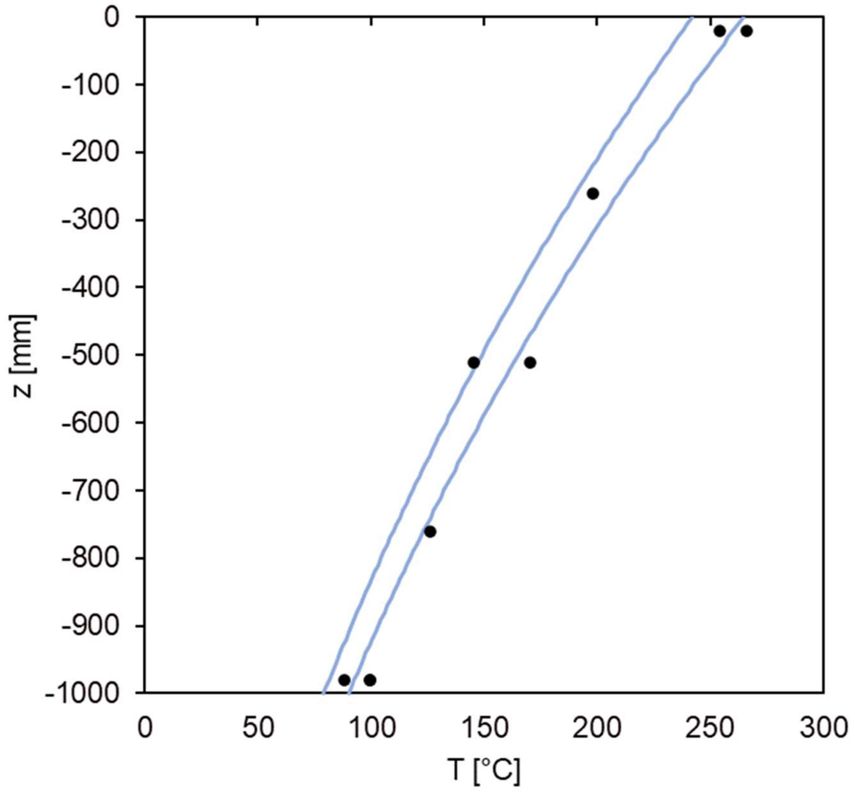

Figure A.3 Temperature profile along the heat exchanger: simulation (line) vs. experimental data (dots).

NOMENCLATURE

Symbols	Description	Units
A	Collecting area	[m^2]
a	Surface area per unit length of the heat exchanger	[m]
C	Concentration factor	
Cou	Courant number	
d_p	Particle diameter	[m]
E	Stored chemical energy	[kJ]
F	Gas molar flowrate	[mol/s]
G_r	Solid mass flux through the riser cross-section	[kg/(s m^2)]
H	Solid specific enthalpy	[J/kg]
h	Air molar enthalpy	[J/mol]
$\hat{h}$	CO_2 molar enthalpy	[J/mol]
I	Incident radiation	[W/m^2]
K	Coefficient in Eq. (8)	[kg/m^3]
L	Length	[m]
M	Molecular weight	[kg/mol]
m	Mass of the solid bed	[kg]
n	Converted moles	[mol]
$\dot{n}$	Product molar rate	[mol/s]
P	Power	[W]
p	Pressure	[bar]
Q	Gas volumetric flowrate	[m^3/s]
R	Ideal gas constant	[J/(mol K)]
R	Heat recovery factor	
S	Cross-section	[m^2]
T	Temperature	[°C]
T*	Temperature at which $\dot{n}_{eq} = \dot{n}_{st}$	[°C]
t	Time	[s]
U	Heat transfer coefficient	[W/(m^2 K)]
u	Gas velocity through the riser cross-section	[m/s]
W	Solid mass flowrate	[kg/s]

X	Conversion degree	
y	Volume fraction	
z	Axial coordinate	[m]
ΔH_{298}	Molar enthalpy change of the calcination reaction at 298 K	[J/mol]
ΔG°	Molar change of Gibbs energy of the calcination reaction	[J/mol]

Greek symbols		
α	Mass fraction of the reactant	
δ	Non-stoichiometric value	
ε	Void degree	
η	Efficiency	
ρ	Density	[kg/m^3]
σ_{SB}	Stefan-Boltzmann constant	[W·m^{-2}·K^{-4}]
τ	Recirculation time	[min]
τ_r	Time for complete conversion	[min]

Subscripts	**Description**
1	Primary, referred to the riser cross-section
2	Secondary, referred to reservoir cross-section
a0	Referred to the receiver or the annulus inlet
ad	Referred to adiabatic conditions
af	Referred to the annulus exit
amb	Referred to ambient conditions
eq	Referred to thermodynamic equilibrium
ex	Referred to the heat exchanger
f	Referred to the receiver
g	Global
in	Referred to the inlet
max	Maximum theoretical value
min	At minimum recirculation conditions
net	Net absorbed
out	Referred to the outlet
r0	Referred to the riser bottom
res	Referred to the reservoir

r,mix	Referred to the riser mixing region
rf	Referred to the riser exit
R	Referred to reservoir in the discharge operation
st	Referred to stoichiometric conditions

REFERENCES

Abanades, S., and André, L. (2018). Design and demonstration of a high temperature solar-heated rotary tube reactor for continuous particles calcination. *Appl. Energy* 212, 1310–1320. doi: 10.1016/j.apenergy.2018.01.019.

Ackermann, S., Takacs, M., Scheffe, J., and Steinfeld, A. (2017). Reticulated porous ceria undergoing thermochemical reduction with high-flux irradiation. *Int. J. Heat Mass Transf.* 107, 439–449. doi: 10.1016/j.ijheatmasstransfer.2016.11.032.

Agrafiotis, C., Roeb, M., and Sattler, C. (2015). A review on solar thermal syngas production via redox pair-based water/carbon dioxide splitting thermochemical cycles. *Renew. Sustain. Energy Rev.* 42, 254–285. doi: 10.1016/j.rser.2014.09.039.

Agrafiotis, C., Von Storch, H., Roeb, M., and Sattler, C. (2014). Solar thermal reforming of methane feedstocks for hydrogen and syngas production - A review. *Renew. Sustain. Energy Rev.* 29, 656–682. doi: 10.1016/j.rser.2013.08.050.

Al-Maaitah, A. (2022). Design & demonstration of a 10-meter metallic reflector-based Fresnel lens, with lower focal point fixed to the ground. *AIP Conf. Proc.* 2445, 1–7. doi: 10.1063/5.0085658.

Alonso, E., and Romero, M. (2015). Review of experimental investigation on directly irradiated particles solar reactors. *Renew. Sustain. Energy Rev.* 41, 53–67. doi: 10.1016/j.rser.2014.08.027.

Alxneit, I. (2008). Assessing the feasibility of separating a stoichiometric mixture of zinc vapor and oxygen by a fast quench - Model calculations. *Sol. Energy* 82, 959–964. doi: 10.1016/j.solener.2008.05.009.

André, L., and Abanades, S. (2017). Evaluation and performances comparison of calcium, strontium and barium carbonates during calcination/carbonation reactions for solar thermochemical energy storage. *J. Energy Storage* 13, 193–205. doi: 10.1016/j.est.2017.07.014.

André, L., Abanades, S., and Flamant, G. (2016). Screening of thermochemical systems based on solid-gas reversible reactions for high temperature solar thermal energy storage. *Renew. Sustain. Energy Rev.* 64, 703–715. doi: 10.1016/j.rser.2016.06.043.

Bellouard, Q., Abanades, S., and Rodat, S. (2017). Biomass Gasification in an Innovative Spouted-Bed Solar Reactor: Experimental Proof of Concept and Parametric Study. *Energy and Fuels* 31, 10933–10945. doi: 10.1021/acs.energyfuels.7b01839.

Block, T., and Schmücker, M. (2016). Metal oxides for thermochemical energy storage: A comparison of several metal oxide systems. *Sol. Energy* 126, 195–207. doi: 10.1016/j.solener.2015.12.032.

Bulfin, B., Miranda, M., and Steinfeld, A. (2021). Performance Indicators for Benchmarking Solar Thermochemical Fuel Processes and Reactors. *Front. Energy Res.* 9, 1–12. doi: 10.3389/fenrg.2021.677980.

Carrillo, A. J., González-Aguilar, J., Romero, M., and Coronado, J. M. (2019). Solar Energy on Demand: A Review on High Temperature Thermochemical Heat Storage Systems and Materials. *Chem. Rev.* 119, 4777–4816. doi: 10.1021/acs.chemrev.8b00315.

Chinnici, A., Arjomandi, M., Tian, Z. F., Lu, Z., and Nathan, G. J. (2015). A Novel Solar Expanding-Vortex Particle Reactor: Influence of Vortex Structure on Particle Residence Times and Trajectories. *Sol. Energy* 122, 58–75. doi: 10.1016/j.solener.2015.08.017.

Cho, H. S., Gokon, N., Kodama, T., Kang, Y. H., and Lee, H. J. (2015). Improved operation of solar reactor for two-step water-splitting H2 production by ceria-coated ceramic foam device. *Int. J. Hydrogen Energy* 40, 114–124. doi: 10.1016/j.ijhydene.2014.10.084.

Chuayboon, S., Abanades, S., and Rodat, S. (2019). Insights into the influence of biomass feedstock type, particle size and feeding rate on thermochemical performances of a continuous solar gasification reactor. *Renew. Energy* 130, 360–370. doi: 10.1016/j.renene.2018.06.065.

Criado, Y. A., Alonso, M., and Abanades, J. C. (2014). Kinetics of the CaO/Ca(OH)2 hydration/dehydration reaction for thermochemical energy storage applications. *Ind. Eng. Chem. Res.* 53, 12594–12601. doi: 10.1021/ie404246p.

Davis, D., Troiano, M., Chinnici, A., Saw, W. L., Lau, T., Solimene, R., et al. (2020). Particle residence time distributions in a vortex-based solar particle receiver-reactor: An experimental, numerical and theoretical study. *Chem. Eng. Sci.* 214, 115421. doi: https://doi.org/10.1016/j.ces.2019.115421.

Di Lauro, F., Tregambi, C., Montagnaro, F., Salatino, P., Chirone, R., and Solimene, R. (2021). Improving the performance of calcium looping for solar thermochemical energy storage and CO2 capture. *Fuel* 298, 120791. doi: 10.1016/j.fuel.2021.120791.

Donat, F., Xu, Y., and Müller, C. R. (2020). Combined Partial Oxidation of Methane to Synthesis Gas and Production of Hydrogen or Carbon Monoxide in a Fluidized Bed using Lattice Oxygen. *Energy Technol.* 8, 1–10. doi: 10.1002/ente.201900655.

Edwards, S. E. B., and Materić, V. (2012). Calcium looping in solar power generation plants. *Sol. Energy* 86, 2494–2503. doi: 10.1016/j.solener.2012.05.019.

Ehrensberger, K., Frei, A., Kuhn, P., Oswald, H. R., and Hug, P. (1995). Comparative experimental investigations of the water-splitting reaction with iron oxide Fe1-yO and iron manganese oxides (Fe1-xMnx)1-yO. *Solid State Ionics* 78, 151–160. doi: 10.1016/0167-2738(95)00019-3.

Ermanoski, I., Siegel, N. P., and Stechel, E. B. (2013). A New Reactor Concept for Efficient Solar-Thermochemical Fuel Production. *J. Sol. Energy Eng.* 135, 1–10. doi: 10.1115/1.4023356.

Esence, T., Benoit, H., Poncin, D., Tessonneaud, M., and Flamant, G. (2020a). A shallow cross-flow fluidized-bed solar reactor for continuous calcination processes. *Sol. Energy* 196, 389–398. doi: 10.1016/j.solener.2019.12.029.

Esence, T., Guillot, E., Tessonneaud, M., Saraiva, A., Le Gal, A., Elidrissi, M., et al. (2020b). Characterization of a pilot fluidized bed reactor for solar calcination processes. *AIP Conf. Proc.* 2303. doi: 10.1063/5.0028763.

Evdou, A., Zaspalis, V., and Nalbandian, L. (2008). La(1-x)SrxMnO3-δ perovskites as redox materials for the production of high purity hydrogen. *Int. J. Hydrogen Energy* 33, 5554–5562. doi: 10.1016/j.ijhydene.2008.06.036.

Evdou, A., Zaspalis, V., and Nalbandian, L. (2010). La1-xSrxFeO3-δ perovskites as redox materials for application in a membrane reactor for simultaneous production of pure hydrogen and synthesis gas. *Fuel* 89, 1265–1273. doi: 10.1016/j.fuel.2009.09.028.

Falter, C. P., and Pitz-paal, R. (2018). Modeling counter-flow particle heat exchangers for two-step solar thermochemical syngas production. *Appl. Therm. Eng.* 132, 613–623. doi: 10.1016/j.applthermaleng.2017.12.087.

Fernández, A. G., Gomez-Vidal, J., Oró, E., Kruizenga, A., Solé, A., and Cabeza, L. F. (2019). Mainstreaming commercial CSP systems: A technology review. *Renew. Energy* 140, 152–176. doi: 10.1016/j.renene.2019.03.049.

Flamant, G. (1982). Theoretical and experimental study of radiant heat transfer in a solar fluidized-bed receiver. *AIChE J.* 28, 529–535.

Flamant, G., Hernandez, D., Bonet, C., and Traverse, J.-P. (1980). Experimental aspects of the thermochemical conversion of solar energy; Decarbonation of CaCO3. *Sol. Energy* 24, 385–395. doi: https://doi.org/10.1016/0038-092X(80)90301-1.

Fletcher, E. A., and Moen, R. L. (1977). Hydrogen and oxygen from water. *Science (80-.).* 197, 1050–1056. doi: 10.1126/science.197.4308.1050.

Geldart, D., and Jones, P. (1991). The behaviour of L-valves with granular powders. *Powder Technol.* 67, 163–174.

Gokon, N., Izawa, T., Abe, T., and Kodama, T. (2014). Steam gasification of coal cokes in an internally circulating fluidized bed of thermal storage material for solar thermochemical processes. *Int. J. Hydrogen Energy* 39, 11082–11093. doi: 10.1016/j.ijhydene.2014.05.124.

Gokon, N., Izawa, T., and Kodama, T. (2015). Steam gasification of coal cokes by internally circulating fluidized-bed reactor by concentrated Xe-light radiation for solar syngas production. *Energy* 79, 264–272. doi: 10.1016/j.energy.2014.11.012.

Gokon, N., Kumaki, S., Miyaguchi, Y., Bellan, S., Kodama, T., and Cho, H. (2019). Development of a 5kWth internally circulating fluidized bed reactor containing quartz sand for continuously-fed coal-coke gasification and a beam-down solar concentrating system. *Energy* 166, 1–16. doi: 10.1016/j.energy.2018.10.036.

Gokon, N., Mataga, T., Kondo, N., and Kodama, T. (2011). Thermochemical two-step water splitting by internally circulating fluidized bed of NiFe2O4 particles : Successive reaction of thermal-reduction and water-decomposition steps. *Int. J. Hydrogen Energy* 36, 4757–4767. doi: 10.1016/j.ijhydene.2011.01.076.

Gokon, N., Ono, R., Hatamachi, T., Liuyun, L., and Kim, H. (2012). CO 2 gasification of coal cokes using internally circulating fluidized bed reactor by concentrated Xe-light irradiation for solar gasification. *Int. J. Hydrogen Energy* 37, 12128–12137. doi: 10.1016/j.ijhydene.2012.05.133.

Gokon, N., Takahashi, S., Yamamoto, H., and Kodama, T. (2008). Thermochemical two-step water-splitting reactor with internally circulating fluidized bed for thermal reduction of ferrite particles. *Int. J. Hydrogen Energy* 33, 2189–2199. doi: 10.1016/j.ijhydene.2008.02.044.

Gokon, N., Takahashi, S., Yamamoto, H., and Kodama, T. (2009). New solar water-splitting reactor with ferrite particles in an internally circulating fluidized bed. *J. Sol. Energy Eng. Trans. ASME* 131, 0110071–0110079. doi: 10.1115/1.3027511.

Gokon, N., Yamamoto, H., Kondo, N., and Kodama, T. (2010). Internally circulating fluidized bed reactor using m-ZrO2 supported NiFe2O4 particles for thermochemical two-step water splitting. *J. Sol. Energy Eng. Trans. ASME* 132, 0211021–02110210. doi: 10.1115/1.4001154.

Haueter, P., Moeller, S., Palumbo, R., and Steinfeld, A. (1999). The production of zinc by thermal dissociation of zinc oxide - Solar chemical reactor design. *Sol. Energy* 67, 161–167. doi: 10.1016/s0038-092x(00)00037-2.

He, F., and Li, F. (2014). Hydrogen production from methane and solar energy - Process evaluations and comparison studies. *Int. J. Hydrogen Energy* 39, 18092–18102. doi: 10.1016/j.ijhydene.2014.05.089.

Hirsch, D., Epstein, M., and Steinfeld, A. (2001). The solar thermal decarbonization of natural gas. *Int. J. Hydrogen Energy* 26, 1023–1033. doi: 10.1016/S0360-3199(01)00040-4.

Hirsch, D., and Steinfeld, A. (2004). Solar hydrogen production by thermal decomposition of natural gas using a vortex-flow reactor. *Int. J. Hydrogen Energy* 29, 47–55. doi: 10.1016/S0360-3199(03)00048-X.

Ho, C. K. (2016). A review of high-temperature particle receivers for concentrating solar power. *Appl. Therm. Eng.* 109, 958–969. doi: 10.1016/j.applthermaleng.2016.04.103.

Ho, C. K., Christian, J., Yellowhair, J., Jeter, S., Golob, M., Nguyen, C., et al. (2017). Highlights of the high-temperature falling particle receiver project: 2012 - 2016. *AIP Conf. Proc.* 1850, 2012–2016. doi: 10.1063/1.4984370.

Hoskins, A. L., Millican, S. L., Czernik, C. E., Alshankiti, I., Netter, J. C., Wendelin, T. J., et al. (2019). Continuous on-sun solar thermochemical hydrogen production via an isothermal redox cycle. *Appl. Energy* 249, 368–376. doi: 10.1016/j.apenergy.2019.04.169.

Kaiser, S., Lo, G., Bosch, K., and Hofbauer, H. (2003). Hydrodynamics of a dual fluidized bed gasifer. Part II: simulation of solid circulation rate, pressure loop and stability. *Chem. Eng. Sci.* 58, 4215–4223. doi: 10.1016/S0009-2509(03)00233-1.

Kodama, T., Cho, H. S., Inoue, K., Saito, T., Watanabe, S., Gokon, N., et al. (2019). Particles fluidized bed receiver/reactor with a beam-down solar concentrating optics: First performance test on two-step water splitting with ceria using a Miyazaki solar concentrating system. *AIP Conf. Proc.* 2126. doi: 10.1063/1.5117691.

Koepf, E., Villasmil, W., and Meier, A. (2016). Pilot-scale solar reactor operation and characterization for fuel production via the Zn/ZnO thermochemical cycle. *Appl. Energy* 165, 1004–1023. doi: 10.1016/j.apenergy.2015.12.106.

Kong, W., Wang, B., Baeyens, J., Li, S., Ke, H., Tan, T., et al. (2018). Solids mixing in a shallow cross-flow bubbling fluidized bed. *Chem. Eng. Sci.* 187, 213–222. doi: 10.1016/j.ces.2018.04.073.

Krenzke, P. T., Fosheim, J. R., and Davidson, J. H. (2017). Solar fuels via chemical-looping reforming. *Sol. Energy* 156, 48–72. doi:

10.1016/j.solener.2017.05.095.

Liu, M., Steven Tay, N. H., Bell, S., Belusko, M., Jacob, R., Will, G., et al. (2016). Review on concentrating solar power plants and new developments in high temperature thermal energy storage technologies. *Renew. Sustain. Energy Rev.* 53, 1411–1432. doi: 10.1016/j.rser.2015.09.026.

Luciani, G., Landi, G., Aronne, A., and Di Benedetto, A. (2018). Partial substitution of B cation in La0.6Sr0.4MnO3 perovskites: A promising strategy to improve the redox properties useful for solar thermochemical water and carbon dioxide splitting. *Sol. Energy* 171, 1–7. doi: 10.1016/j.solener.2018.06.058.

Luciani, G., Landi, G., Imparato, C., Vitiello, G., Deorsola, F. A., Di Benedetto, A., et al. (2019). Improvement of splitting performance of Ce0.75Zr0.25O2 material: Tuning bulk and surface properties by hydrothermal synthesis. *Int. J. Hydrogen Energy* 44, 17565–17577. doi: 10.1016/j.ijhydene.2019.05.021.

Martin, J., and Vitko, J. J. (1982). ASCUAS: a solar central receiver utilizing a solid thermal carrier. Available at: https://doi.org/10.2172/5663779.

Miller, D. C., Pfutzner, C. J., and Jackson, G. S. (2018). Heat transfer in counterflow fluidized bed of oxide particles for thermal energy storage. *Int. J. Heat Mass Transf.* 126, 730–745. doi: 10.1016/j.ijheatmasstransfer.2018.05.165.

Moumin, G., Tescari, S., Sundarraj, P., de Oliveira, L., Roeb, M., and Sattler, C. (2019). Solar treatment of cohesive particles in a directly irradiated rotary kiln. *Sol. Energy* 182, 480–490. doi: 10.1016/j.solener.2019.01.093.

Muhich, C. L., Ehrhart, B. D., Witte, V. A., Miller, S. L., Coker, E. N., Musgrave, C. B., et al. (2015). Predicting the solar thermochemical water splitting ability and reaction mechanism of metal oxides: A case study of the hercynite family of water splitting cycles. *Energy Environ. Sci.* 8, 3687–3699. doi: 10.1039/c5ee01979f.

Nakamura, T. (1977). Hydrdogen production from water utilizing solar heat at high temperatures. *Sol. Energy* 19, 467–475. doi: https://doi.org/10.1016/0038-092X(77)90102-5.

next - CSP Available at: http://next-csp.eu/.

Nie, F., Bai, F., Wang, Z., Li, X., and Yang, R. (2022). Solid particle solar receivers in the next-generation concentrated solar power plant. *EcoMat*, 1–27. doi: 10.1002/eom2.12207.

Nikulshina, V., Halmann, M., and Steinfeld, A. (2009). Coproduction of syngas and lime by combined CaCO3-calcination and CH4-reforming using a particle-flow reactor driven by concentrated solar radiation. *Energy and Fuels* 23, 6207–6212. doi: 10.1021/ef9007246.

Nzihou, A., Flamant, G., and Stanmore, B. (2012). Synthetic fuels from biomass using concentrated solar energy - A review. *Energy* 42, 121–131. doi: 10.1016/j.energy.2012.03.077.

Osinga, T., Frommherz, U., Steinfeld, A., and Wieckert, C. (2004). Experimental investigation of the solar carbothermic reduction of ZnO using a two-cavity solar reactor. *J. Sol. Energy Eng. Trans. ASME* 126, 633–637. doi: 10.1115/1.1639001.

Padula, S., Tregambi, C., Solimene, R., Chirone, R., Troiano, M., and Salatino, P. (2021). A novel fluidized bed “ thermochemical battery ” for energy storage in concentrated solar thermal technologies. *Energy Convers. Manag.* 236.

Panlener, R. J., Garnier, J. E., and Blumenthal, R. N. (1976). A thermodynamic study of nonstoichiometric cerium dioxide. *J. Phys. Chem. Solids* 37, 368–378. doi: 10.1016/0022-3697(76)90017-2.

Pardo, P., Anxionnax-Minvielle, Z., Rougé, S., Cognet, P., and Cabassud, M. (2014). Ca(OH)2 / CaO reversible reaction in a fluidized bed reactor for thermochemical heat storage. *Sol. Energy* 107, 605–616. doi: 10.1016/j.solener.2014.06.010.

Perry, R. H. (2008). *Perry's Chemical Engineer's Handbook*. 8th Editio. , ed. D. W. Green McGraw Hill Education.

Piatkowski, N., Wieckert, C., and Steinfeld, A. (2009). Experimental investigation of a packed-bed solar reactor for the steam-gasification of carbonaceous feedstocks. *Fuel Process. Technol.* 90, 360–366. doi: 10.1016/j.fuproc.2008.10.007.

Pitz-Paal, R. (2020). "Concentrating solar power," in *Future Energy: Improved, Sustainable and Clean Options for Our Planet* (Elsevier Ltd), 413–430. doi: 10.1016/B978-0-08-102886-5.00019-0.

Puig-Arnavat, M., Tora, E. A., Bruno, J. C., and Coronas, A. (2013). State of the art on reactor designs for solar gasification of carbonaceous feedstock. *Sol. Energy* 97, 67–84. doi: 10.1016/j.solener.2013.08.001.

Roeb, M., Neises, M., Monnerie, N., Call, F., Simon, H., Sattler, C., et al. (2012). Materials-Related Aspects of Thermochemical Water and Carbon Dioxide Splitting: A Review. *Materials (Basel).* 5, 2015–2054. doi: 10.3390/ma5112015.

Salatino, P., Ammendola, P., Bareschino, P., Chirone, R., and Solimene, R. (2016). Improving the thermal performance of fluidized beds for concentrated solar power and thermal energy storage. *Powder Technol.* 290, 97–101. doi: 10.1016/j.powtec.2015.07.036.

Schäppi, R., Rutz, D., Dähler, F., Muroyama, A., Haueter, P., Lilliestam, J., et al. (2022). Drop-in fuels from sunlight and air. *Nature* 601, 63–68. doi: 10.1038/s41586-021-04174-y.

Schaube, F., Koch, L., Wörner, A., and Müller-Steinhagen, H. (2012). A thermodynamic and kinetic study of the de- and rehydration of Ca(OH) 2 at high H 2O partial pressures for thermo-chemical heat storage. *Thermochim. Acta* 538, 9–20. doi: 10.1016/j.tca.2012.03.003.

Scheffe, J. R., and Steinfeld, A. (2012). Thermodynamic analysis of cerium-based oxides for solar thermochemical fuel production. *Energy and Fuels* 26, 1928–1936. doi: 10.1021/ef201875v.

Scheffe, J. R., and Steinfeld, A. (2014). Oxygen exchange materials for solar thermochemical splitting of H2O and CO2: A review. *Mater. Today* 17, 341–348. doi: 10.1016/j.mattod.2014.04.025.

Scheffe, J. R., Weibel, D., and Steinfeld, A. (2013). Lanthanum-strontium-manganese perovskites as redox materials for solar thermochemical splitting of H2O and CO2. *Energy and Fuels* 27, 4250–4257. doi: 10.1021/ef301923h.

Schunk, L. O., Haeberling, P., Wept, S., Wuillemin, D., Meier, A., and Steinfeld, A. (2008). A receiver-reactor for the solar thermal dissociation of zinc oxide. *J. Sol. Energy Eng. Trans. ASME* 130, 0210091–0210096. doi: 10.1115/1.2840576.

Shackelford, J. F., and Alexander, W. (2006). *CRC Handbook of Chemistry and Physics*. 86th Editi. , ed. D. R. Lide CRC Press Available at: https://doi.org/10.1021/ja059868l.

Solimene, R., Chirone, R., Chirone, R., and Salatino, P. (2017). Dynamic modeling of a solar receiver/thermal energy storage system based on a compartmented dense gas fluidized bed. *AIP Conf. Proc.* 1850. doi: 10.1063/1.4984447.

Steinfeld, A. (2002). Solar hydrogen production via a two-step water-splitting thermochemical cycle based on Zn/ZnO redox reactions. *Int. J. Hydrogen Energy* 27, 611–619. doi: 10.1016/S0360-3199(01)00177-X.

Steinfeld, A., Brack, M., Meier, A., Weidenkaff, A., and Wuillemin, D.

(1998). A solar chemical reactor for co-production of zinc and synthesis gas. *Energy* 23, 803–814. doi: 10.1016/S0360-5442(98)00026-7.

STEM®-CST Concentrated Solar Thermal Available at: https://www.magaldigreenenergy.com/en/stem.

Suárez-almeida, M., Gómez-barea, A., Pfeifer, C., and Leckner, B. (2021). Fluid dynamic analysis of dual fluidized bed gasifier for solar applications Citation for the original published paper (version of record): *Powder Technol.* 390, 482–495. doi: 10.1016/j.powtec.2021.05.032.

Synhelion (2022). Available at: https://synhelion.com/.

Tamaura, Y., Kojima, N., Hasegawa, N., Inoue, M., Uehara, R., Gokon, N., et al. (2001). Stoichiometric studies of H2 generation reaction for H2O/Zn/Fe3O4 system. *Int. J. Hydrogen Energy* 26, 917–922. doi: 10.1016/S0360-3199(01)00039-8.

Tan, T., and Chen, Y. (2010). Review of study on solid particle solar receivers. *Renew. Sustain. Energy Rev.* 14, 265–276. doi: 10.1016/j.rser.2009.05.012.

Tescari, S., Moumin, G., Bulfin, B., De Oliveira, L., Schaefer, S., Overbeck, N., et al. (2018). Experimental and numerical analysis of a solar rotary kiln for continuous treatment of particle material. *AIP Conf. Proc.* 2033, 1–8. doi: 10.1063/1.5067148.

Tescari, S., Neumann, N. C., Sundarraj, P., Moumin, G., Rincon Duarte, J. P., Linder, M., et al. (2022). Storing solar energy in continuously moving redox particles – Experimental analysis of charging and discharging reactors. *Appl. Energy* 308, 118271. doi: 10.1016/j.apenergy.2021.118271.

Tescari, S., Singh, A., Agrafiotis, C., de Oliveira, L., Breuer, S., Schlögl-Knothe, B., et al. (2017). Experimental evaluation of a pilot-scale thermochemical storage system for a concentrated solar power plant.

Appl. Energy 189, 66–75. doi: 10.1016/j.apenergy.2016.12.032.

Tescari, S., Sundarraj, P., Moumin, G., Duarte, J. P. R., Agrafiotis, C., de Oliveira, L., et al. (2020). Solar rotary kiln for continuous treatment of particle material: Chemical experiments from micro to milli meter particle size. *AIP Conf. Proc.* 2303. doi: 10.1063/5.0029271.

Tregambi, C., Bevilacqua, C., Troiano, M., Solimene, R., and Salatino, P. (2020a). A novel autothermal fluidized bed reactor for concentrated solar thermal applications. *Chem. Eng. J.* 398, 125702. doi: 10.1016/j.cej.2020.125702.

Tregambi, C., Chirone, R., Montagnaro, F., Salatino, P., and Solimene, R. (2016). Heat transfer in directly irradiated fluidized beds. *Sol. Energy* 129, 85–100. doi: 10.1016/j.solener.2016.01.057.

Tregambi, C., Di Lauro, F., Montagnaro, F., Salatino, P., and Solimene, R. (2019). 110th anniversary: Calcium looping coupled with concentrated solar power for carbon capture and thermochemical energy storage. *Ind. Eng. Chem. Res.* 58, 21262–21272. doi: 10.1021/acs.iecr.9b03083.

Tregambi, C., Padula, S., Galbusieri, M., Coppola, G., Montagnaro, F., Salatino, P., et al. (2020b). Directly irradiated fluidized bed reactor for thermochemical energy storage and solar fuels production. *Powder Technol.* 366, 460–469. doi: 10.1016/j.powtec.2020.02.045.

Tregambi, C., Troiano, M., Montagnaro, F., Solimene, R., and Salatino, P. (2021). Fluidized Beds for Concentrated Solar Thermal Technologies—A Review. *Front. Energy Res.* 9, 1–26. doi: 10.3389/fenrg.2021.618421.

Troiano, M., Ianzito, V., Solimene, R., Ganda, E. T., and Salatino, P. (2022). Fluidized Bed Pyrolysis of Biomass: A Model-Based Assessment of the Relevance of Heterogeneous Secondary Reactions and Char Loading. *Energy and Fuels* 36, 9660–9671. doi: 10.1021/acs.energyfuels.2c01483.

Tzouganatos, N., Wieckert, C., and Steinfeld, A. (2016). A Packed-Bed Solar

Reactor for the Carbothermal Zinc Production – Dynamic Modelling and Experimental Validation. *AIChE J.* 62, 4586–4594. doi: 10.1002/aic.

Wieckert, C., Frommherz, U., Kräupl, S., Guillot, E., Olalde, G., Epstein, M., et al. (2007). A 300 kW Solar chemical pilot plant for the carbothermic production of zinc. *J. Sol. Energy Eng. Trans. ASME* 129, 190–196. doi: 10.1115/1.2711471.

Wong, B., Schaube, F., Wörner, A., and Tamme, R. (2011). Thermochemical Heat Storage for Concentrated Solar Power, Thermochemical System Reactor Design for Thermal Energy Storage.

Yadav, D., and Banerjee, R. (2016). A review of solar thermochemical processes. *Renew. Sustain. Energy Rev.* 54, 497–532. doi: 10.1016/j.rser.2015.10.026.

Yang, W.-C., and Knowlton, T. M. (1993). L-valve equations. *Powder Technol.* 77, 49–54.

Yoon, S. M., and Kunii, D. (1970). Gas Flow and Pressure Drop through Moving Beds. 9, 559–565.

Z'Graggen, A., Haueter, P., Trommer, D., Romero, M., de Jesus, J. C., and Steinfeld, A. (2006). Hydrogen production by steam-gasification of petroleum coke using concentrated solar power-II Reactor design, testing, and modeling. *Int. J. Hydrogen Energy* 31, 797–811. doi: 10.1016/j.ijhydene.2005.06.011.

Z'Graggen, A., and Steinfeld, A. (2008). Hydrogen production by steam-gasification of carbonaceous materials using concentrated solar energy - V. Reactor modeling, optimization, and scale-up. *Int. J. Hydrogen Energy* 33, 5484–5492. doi: 10.1016/j.ijhydene.2008.07.047.

Zhang, H., Benoit, H., Perez-Lopèz, I., Flamant, G., Tan, T., and Baeyens, J. (2017). High-efficiency solar power towers using particle suspensions as heat carrier in the receiver and in the thermal energy storage. *Renew.*

Energy 111, 438–446. doi: 10.1016/j.renene.2017.03.101.

Zhang, H., Xiao, R., Pan, Q., Song, Q., and Huang, H. (2009). Hydrodynamics of a Novel Biomass Autothermal Fast Pyrolysis Reactor: Flow Pattern and Pressure Drop. *Chem. Eng. Technol.*, 27–37. doi: 10.1002/ceat.200800541.

Zsembinszki, G., Sole, A., Barreneche, C., Prieto, C., Fernández, A. I., and Cabeza, L. F. (2018). Review of reactors with potential use in thermochemical energy storage in concentrated solar power plants. *Energies* 11. doi: 10.3390/en11092358.